



Ue Fiscardi

Registration number,
"Petru Poni" Institute
of Macromolecular Chemistry

SCIENTIFIC STAGE REPORT
PN-III-P4-ID-PCCF-2016-0050 Project. Contract no. 4/2018.
-- 2019 Stage --

Mimicking Living Matter Mechanisms by Five-dimensional Chemistry Approaches

*Mimarea mecanismelor viului prin abordări ale chimiei supramoleculare,
în cinci dimensiuni*

Acronym: 5D-nanoP

Coordinating Institute,
"Petru Poni" Institute of Macromolecular Chemistry
Legal representative,
Dr. Anton Airinei, physicist

Project Director,
Professor Aatto Laaksonen, PhD.

This document is the property of the organizations involved in the project, and may not be reproduced, distributed, or used by, and/or to third parties, without the prior consent of the authors.

Contents

	Page
I. Generic approaches within the 2019 stage of the project	1
II. The research results of 2019 stage	3
A.1. - Selection of a biomolecular candidate and preliminary studies of a typical nanoentity of biologic origin, as a prototype of functional nanoplatforms	3
A.2. - Design, synthesis, and characterization of some molecular constructs able to act as supramolecular active components of nanoplatforms	7
A.3. - Producing and preliminary testing of extracellular matrix / tumors surrogates dedicated to the ex vivo evaluation of supramolecular nanoplatforms	17
A.4. - Development of micro-particulate systems applicable as mezo-porous substrata for the delivery and for the amount control of low molecular (bio)active compounds	29
A.5. - Evaluation of the functionality of the extracellular matrix / tumors surrogates in <i>ex vivo</i> systems of cells culturing	45
A.6. - <i>In silico</i> approaches on delivering systems adapted for macro- and supra-molecular constructs	59
References	70
III. Quantifiable results of the project, obtained during the 2019 stage	80
IV. Topics and prognoses for Stage 2020	84

I. Generic approaches within the 2019 stage of the project

The 2019 stage of **5D-nanoP** project is devoted to the obtaining and characterization of: (i) the main and / or typical molecular constituents of the nanoplatforms to be further developed, and (ii) some structured macromolecular substrata able to mimic the environments in which the developed nanoplatforms are designed to act and work. According the general implementation plan of the project, the main goals of the current stage consist in:

- the selection and preliminary study of a biomacromolecular prototype of a functional nanoplatform intended to be mimicked by means of supramolecular chemistry approaches into the frame of 5D-nanoP project; an enzyme was chosen in this respect, in order to capture the real complexity of the capabilities (like the specificity of action and of substrates) of highly versatile and performant biological entities;
- the elaboration of the generic protocols for the synthesis and characterization of some particular (macro)molecular components which will be further used to develop mimetic supramolecular assemblies;
- the design, producing and preliminary testing of a macromolecular scaffold, together with the overall framework of its functional characterization as a biocompatible substrata able to incorporate, to vehiculate and to assist the functional supramolecular aggregates.

The details of the implementation work of Stage 2019 are summarized in the Synopsis 1 (inserted on next page).

Synopsis 1. Implementation plan and results of 5D-nanoP – Stage 2019.

Year	Stage	Main objective of Stage 2019	Particular / adapted activities and sub-activities carried out	Stage results and deliverables
2019	The single one	Obtaining and physical - chemical characterization of the constituents of nanoplatfoms and of the substrata for their <i>ex vivo</i> testing	A.1. Selection of a biomolecular candidate and preliminary studies of a typical nanoentity of biologic origin, as a prototype of functional nanoplatfoms.	<ol style="list-style-type: none"> 1. Research report (Stage 2019). 2. Particular protocols for synthesis and testing. 3. Particular protocols for <i>in silico</i> studies. 4. 17 published scientific papers. 5. Two submitted and accepted scientific papers. 6. 14 participations to conferences and symposia, with communications and poster works. <p>Note: (2) and (3) of above are included in the published papers.</p>
			A.2. Design, synthesis, and characterization of some molecular constructs able to act as supramolecular active components of nanoplatfoms.	
			A.3. Producing and preliminary testing of extracellular matrix / tumors surrogates dedicated to the <i>ex vivo</i> evaluation of supramolecular nanoplatfoms.	
			A.4. Development of micro-particulate systems applicable as mezo-porous substrata for the delivery and for the amount control of low molecular (bio)active compounds.	
			A.5. Evaluation of the functionality of the extracellular matrix / tumors surrogates in <i>ex vivo</i> systems of cells culturing.	
			A.6. <i>In silico</i> approaches on delivering systems adapted for macro- and supra-molecular constructs.	

II. The research results of 2019 stage

A.1. Selection of a biomolecular candidate and preliminary studies of a typical nanoentity of biologic origin, as a prototype of functional nanoplatforms

In order to understand the particular functionality of a natural nanoentity, prior to mimic its behavior as a supramolecular nanoplatform, we choose to investigate the activity of a family of peculiar enzymes, widely spread in all the biological kingdoms and cells (starting from bacteria, to mammalian), the carbonic anhydrases. We consider them as acting as typical nanoplatforms in their relation with their low molecular activators and inhibitors, together with which they generate dynamic supramolecular assemblies.

The *carbonic anhydrases* (or *carbonate dehydratases*) (CA) form a family of enzymes that catalyze the interconversion between carbon dioxide and water and the dissociated ions of carbonic acid (i.e. bicarbonate and protons): $\text{CO}_2 + \text{H}_2\text{O} \rightleftharpoons \text{HCO}_3^- + \text{H}^+$ [1]. The active site of CA contains a Zn^{2+} ion, making them to be classified as metalloenzymes, maintaining acid-base balance and helps transport carbon dioxide [2]. Carbonic anhydrase helps regulate pH and fluid balance. Depending on its location, the role of the enzyme changes slightly. For example, carbonic anhydrase produces acid in the stomach lining. In the kidney, the control of bicarbonate ions influences the water content of the cell. The control of bicarbonate ions also influences the water content in the eyes, and if the enzyme does not work properly, a buildup of fluid can lead to glaucoma [3].

At least seven distinct CA genetic families are known to date (α -, β -, γ -, ξ -, η -, θ -CA) and their diffusion and physiological roles have been investigated in details mainly in vertebrates, including humans, who possess only α -CAs, but with quite a large number of isoforms [4-8]. The studies on CA are carried out in 2 directions: finding some CA inhibitors (CAIs) or finding CA activators (CAAs), depending on the disease to be managed. Recently, it has been demonstrated that CAAs may have pharmacological applications for enhancing cognition, in the management of CA deficiencies, for therapy memory and for obtaining artificial tissues as well as for investigating the effects of endogenous amino acids and amines on CA activity [9-11], while CAIs are belonging to many diverse chemotypes, possessing a wealth of inhibition mechanisms, are clinically used for the management of a variety of disorders, including edema, epilepsy, glaucoma, obesity, hypoxic tumors, neuropathic pain and arthritis [12-14].

I. – Low molecular weight compounds acting as CA activators (CAAs) [15]

The activation studies of the β -class CA enzymes from the pathogenic bacteria *Brucella suis* and *Francisella tularensis* may bring some insights in the difficult processes related with the invasion and pathogenic effects of intracellular bacteria when attacking their hosts. The pathogenic bacteria *Brucella suis* and *Francisella tularensis* provoke serious diseases both in human and livestock and are difficult to treat by antibiotics, and have the potential to induce widespread infections. The genome of *Brucella suis* encodes two β -CAs (BsuCA1 and BsuCA 2) whereas in the genome of *Francisella tularensis* encodes only one β -CA class enzyme (FtuCA). Our studies were done by using 24 amino acid and amine derivative (Figure 1). It should be noted that many of the investigated amino acid and amines are present in rather high concentrations in many tissues in vertebrates, and their role in the pathogenicity of the two bacteria is poorly understood. In this context, our studies showed: BsuCA 1 was sensitive to activation with amino acids and amines, which showed activation constants in the range of 0.70 – 43.1 μM . The most effective BsuCA 1 activators were L-adrenaline and D-Tyr (K_{AS} of 0.70-0.95 μM). L-His, L-/D-Phe, L-/D-DOPA, L-Trp, L-Tyr, 4-amino-L-Phe, dopamine, 2-pyridyl-methylamine, D-Glu and L-Gln showed activation constants in the range of 0.70 – 3.21 μM . FtuCA was not sensitive to activation with many of the investigated compounds ($K_A > 100 \mu\text{M}$), and only L-Glu had a $K_A < 10 \mu\text{M}$. Most of the investigated active compounds showed a weak

activating effect against FtuC_A, with K_{AS} ranging between 30.5 – 78.3 μM, such a L-/D-His, L-/D-Phe, L-/D-Trp, 2-pyridyl-methylamine.

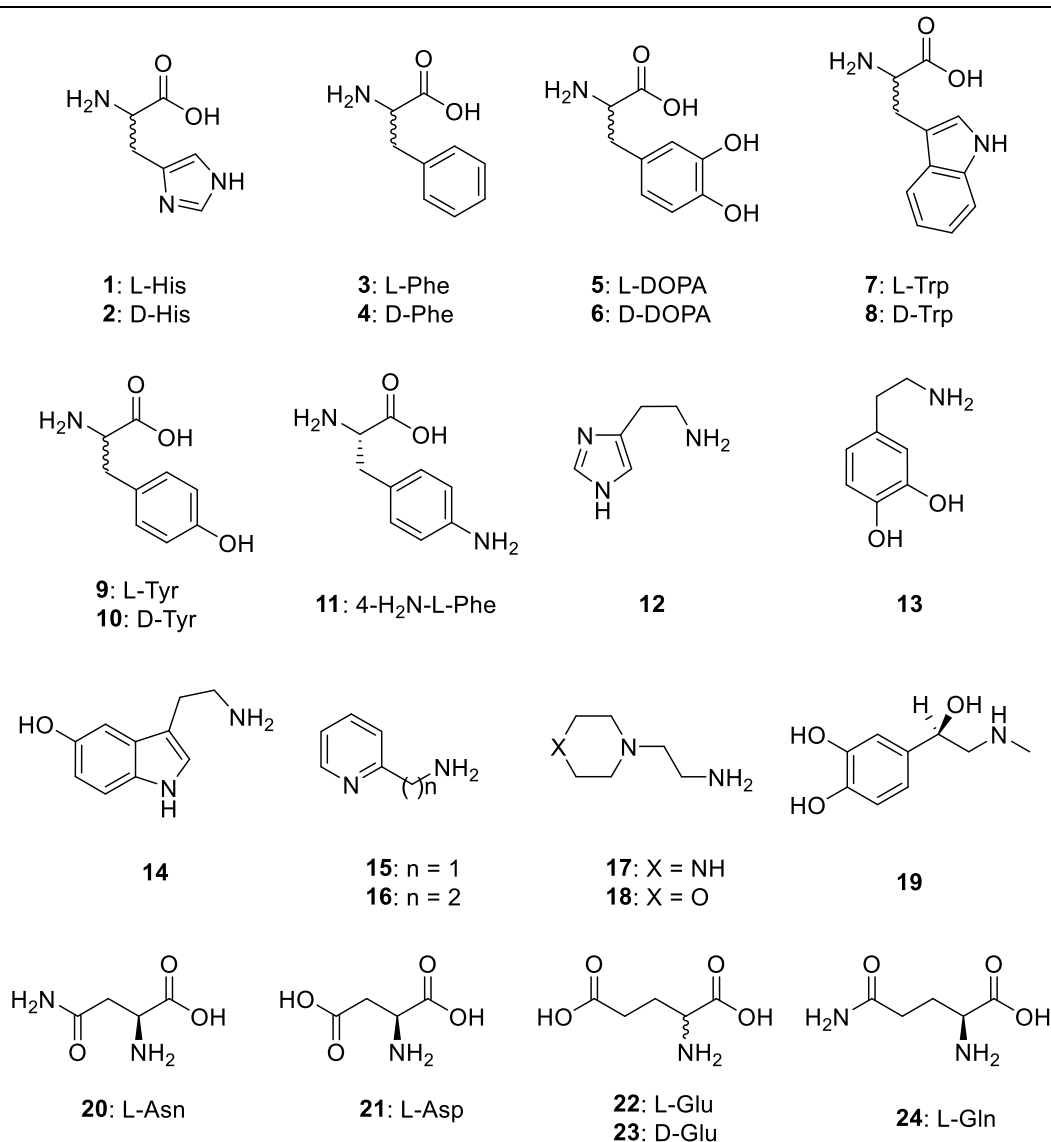


Figure 1. Amino acids and amines used as potential activators of β -class CA enzymes.

II. – Low molecular weight compounds acting as CA inhibitors (CAIs)

CAIs are not yet seriously considered as potential anti-infectives up until now, mainly due to the fact that no relevant drug discovery program has been yet started, although these compounds may show indeed a great promise for fighting drug resistant microbes, such as bacteria, fungi and protozoa [16-18].

A. Selenazoles incorporating benzenesulfonamide moieties as bacterial α -, β - and γ -class CA inhibitors [19]

In the last decade, a large number of studies were dedicated to discovering effective *in vitro* CA inhibitors (CAIs) of CAs enzymes encoded by the *Helicobacter pylori* (a Gram-negative bacterium colonizing the human stomach), *Vibrio cholera* (a Gram-negative bacterium provoking cholera), *Brucella suis* (non-motile Gram-negative coccobacillus), and the *Burkholderia pseudomallei* (a Gram-negative bacterium) pathogens and their possibility to translate the results *in vivo* and clinical applications [20-23].

It has been demonstrated that the genome of the pathogen *Helicobacter pylori* (a Gram-negative bacterium colonizing the human stomach) encodes two CAs (α and β) enzymes and are

essential for the acid acclimatization of the *Helicobacter pylori* pathogen within the human stomach and thus, for the bacterial survival in the host [24-26]. *Vibrio cholerae* (a Gram-negative bacterium provoking cholera) uses its CAs (α , β and γ) for producing sodium bicarbonate, which induces cholera toxin expression, and for colonizing the host [27, 28], while *Burkholderia pseudomallei* (encoding BpsCA β and BpsCA γ enzymes) infects humans, animals and plants and causes the disease melioidosis [29].

In this context, our main interest was to investigate structure-activity relationship related to the inhibition of different CAs classes from different pathogenic bacteria: *Helicobacter pylori* (hpCA α), *Vibrio cholerae* (VchCA α , VchCA β and VchCA γ), and *Burkholderia pseudomallei* (BpsCA β and BpsCA γ), relevant pathogens in many diseases for which drug resistant strains were evidenced, using a series of benzenesulfonamides incorporating selenazoles with diverse substitution patterns (Figure 2).

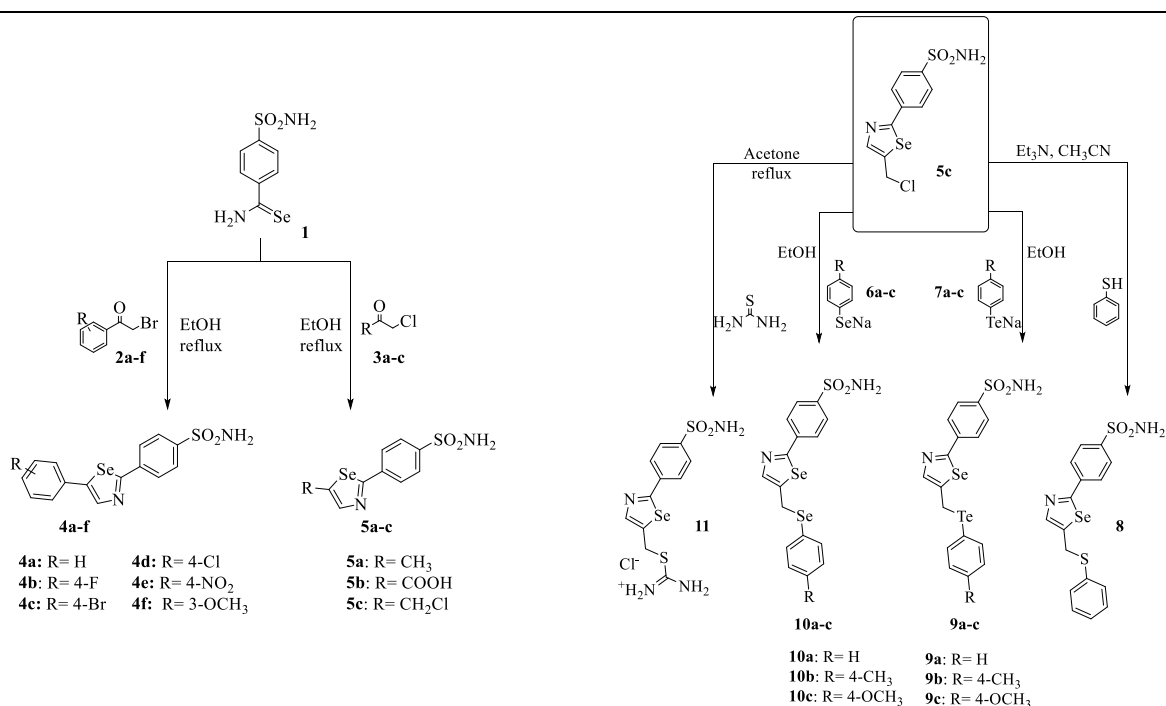


Figure 2. Unsubstituted and substituted selenazoles used as inhibitors in the studies on the structure-activity relationship related to the inhibition of different CAs classes from different pathogenic bacteria.

All the investigated sulfonamides were effective inhibitors, with potencies in the low micromolar or submicromolar range, making this class of CAs inhibitors attractive as lead compounds for designing antibacterials with a novel mechanism of action, which could counteract the extensive antibiotic resistance problem encountered with most clinically used such drugs.

B. Famotidine as bacterial α -, β - and γ -class CAs inhibitor [30]

Famotidine (Figure 3) is a generic medication that decreases stomach acid production [31]. It is used to treat peptic ulcer disease, gastroesophageal reflux disease, and Zollinger-Ellison syndrome.

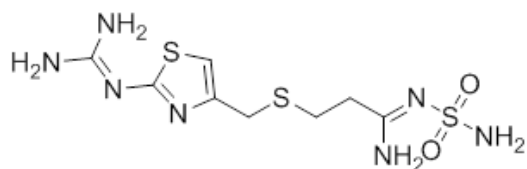


Figure 3. The chemical structure of famotidine.

We investigated the inhibitory effects of famotidine against all classes of CAs from the pathogenic bacteria *Vibrio cholerae*, *Burkholderia pseudomallei*, *Mycobacterium tuberculosis* (Rv3273 β -CA), as well as the CAs from the non-pathogenic bacteria/cyanobacteria *Sulfurihydrogenibium yellowstonensis*, *S. azorense*, *Pseudoalteromonas haloplanktis*, *Colwellia psychrerythraea*, *Nostoc commune*. The δ - and ζ -CAs from the diatom *Thalassiosira weissflogii*, the fungal enzymes from *Cryptococcus neoformans*, *Candida glabrata* and *Malassezia globosa*, as well as the protozoan enzymes from *Trypanosoma cruzi* and *Plasmodium falciparum*, were also investigated. *Anopheles gambiae* β -CA was also investigated. All these enzymes were effectively inhibited by famotidine, with affinities between the low nanomolar to the micromolar range. For some pathogenic enzymes such as those from *V. cholerae*, *C. albicans*, *P. falciparum* as well as the mosquitoes involved in malaria transmission (*A. gambiae*), the drug showed efficacy in the range of $13.6 \div 397$ nM, making it a possible lead or a possible agent for more detailed, in vivo investigations. The best inhibition was observed against *C. glabrata* fungus (β -CA and TweCA ζ , with K_{iS} ranging between 13.6 and 22.1 nM).

C. Synthesis of a series of phenothiazine based compounds with proper design for carbonic anhydrase inhibition

At the end of the 2019 stage of the project we started to investigate the synthesis, characterization and the inhibitory activity of a new class of phenothiazine derivatives (Figure 4). Work on these compounds is in progress.

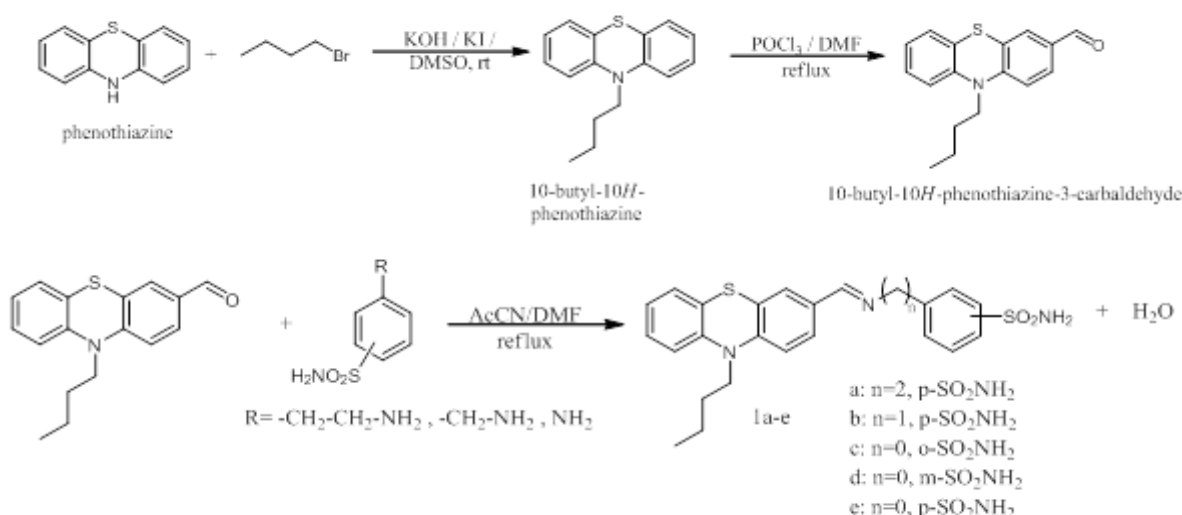


Figure 4. The synthesis pathway of the phenothiazine derivatives applicable as CAs inhibitors.

D. Unimers acting as CAs inhibitors

Our goal was to develop a strategy to functionalize squalene (Sq) with sulphonamide groups, to obtain a library of compounds being able to self-aggregate into reversible micelles (Figure 5), and acting as CAs inhibitors. A few authors have investigated the exchange dynamics between polymer aggregates and unimers by mixing two populations of micelles, labeled, and unlabeled.

Functionalization of Sq-COOH was designed as a two step synthesis: (i) activation of carboxylic function, and (ii) amide formation in presence of base, in DMF. Three derivatives were obtained (CL-SQ-02, CL-SQ-06 and CL-SQ-16), while aromatic amine was not sufficiently reactive to form the amide. The obtained compounds were preliminary tested on carbon anhydrase isoforms I, II, IX and XII using an SX.18MV-R Applied Photophysics (Oxford, UK) stopped-flow instrument, to assay the catalytic/inhibition of CAII. As reference, acetazolamide

(AAZ) was used. From the series of compounds, CL-SQ-06 showed a selective inhibition on hCAII, with a K_I (nM)* value of 5.0, which is significantly lower than for control AAZ.

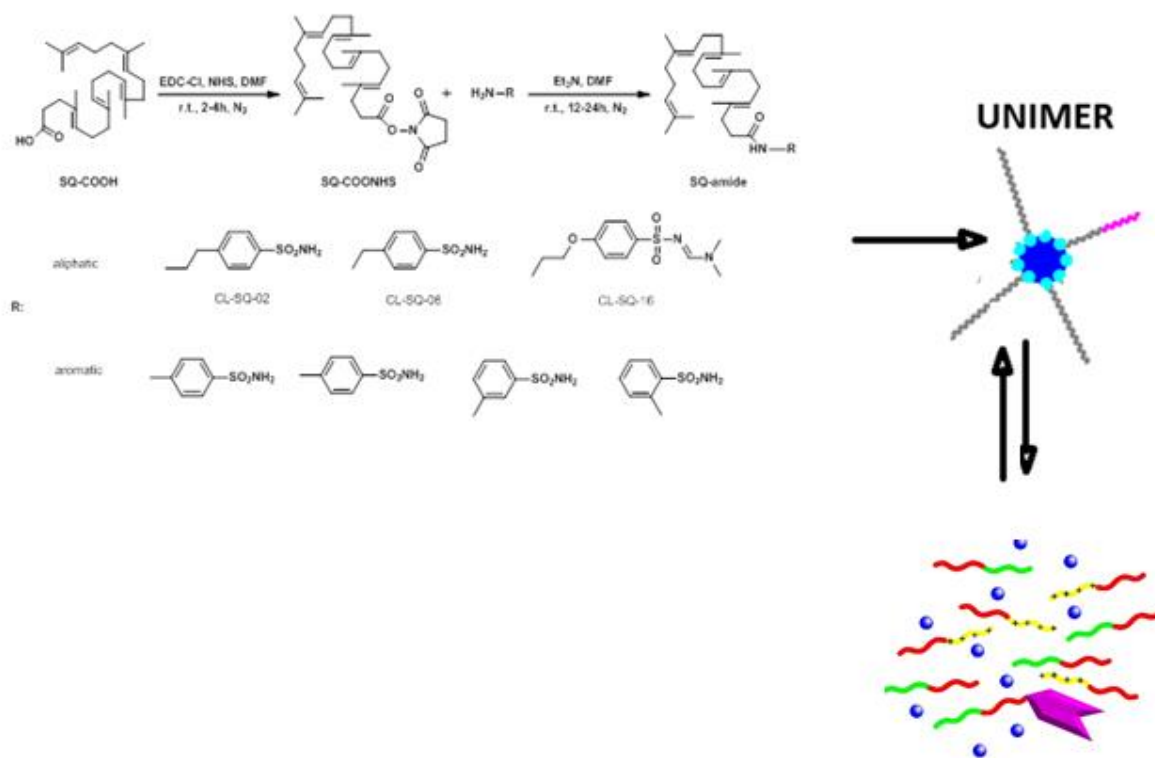


Figure 5. The synthesis pathway of the squalene-sulphonamide unimer.

A.2. Design, synthesis, and characterization of some molecular constructs able to act as supramolecular active components of nanoplatforms

Stage 2019 of the **5D-nanoP** project aimed to develop adapted protocols to obtain and to characterize (macro)molecular constructs which could become parts of delivering systems of nanoplatform types. In this respect, two distinctive (macro) molecular systems were considered, one of unimeric type, with aggregation ability and able to act as an antibacterial / antimycotic, and the second of macromolecular platform type, able to sustain further development of a functional nanoplatform.

I. – Silicone-bridged bis-triazoles as effective, selective metal ligands and biologically active agents in lipophilic environment

Pairs of different substituted 3-mercapto-1,2,4-triazole units were coupled, through thioether bridges, to organic-inorganic substrates consisting in short hydrophobic silicone segment (Figure 6). A library of six compounds are isolated as crystalline solids and structurally characterized by X-ray single crystal diffraction, elemental, spectral and thermal analysis (Figure 7). The flexibility of the silicone spacer makes the small molecular compounds exhibit glass transition in the negative domain. The metal binding capacity is evaluated by quantum mechanics calculations, the results being in line with experimental data obtained by UV-vis spectroscopy titration. The results indicate that the prepared compounds can act as ligands for metal ions with high selectivity for Cu^{2+} , an element of interest in biological processes, forming 1: 1 stable mononuclear complexes with an association constant up to $8.87 \times 10^3 \text{ M}^{-1}$. The presence of the highly hydrophobic silicone spacer makes the behavior of bis-triazoles obtained

more sensitive to the nature of the environment. The preliminary bioassay indicates lipophilic medium more suitable for biocide action of silicone-bridged bis-triazoles, which in some cases far exceeds that of reference. The mechanism of enzyme inhibition is demonstrated by molecular docking, and the results indicate that, in all docked complexes, the ligands are directly coordinated to the heme ferric iron.

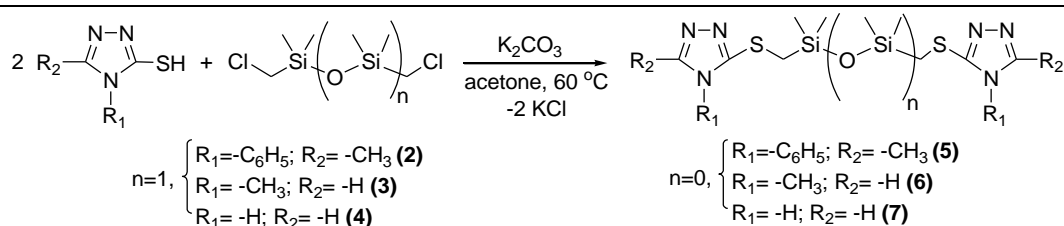


Figure 6. The reactions leading to bis-triazoles [32].

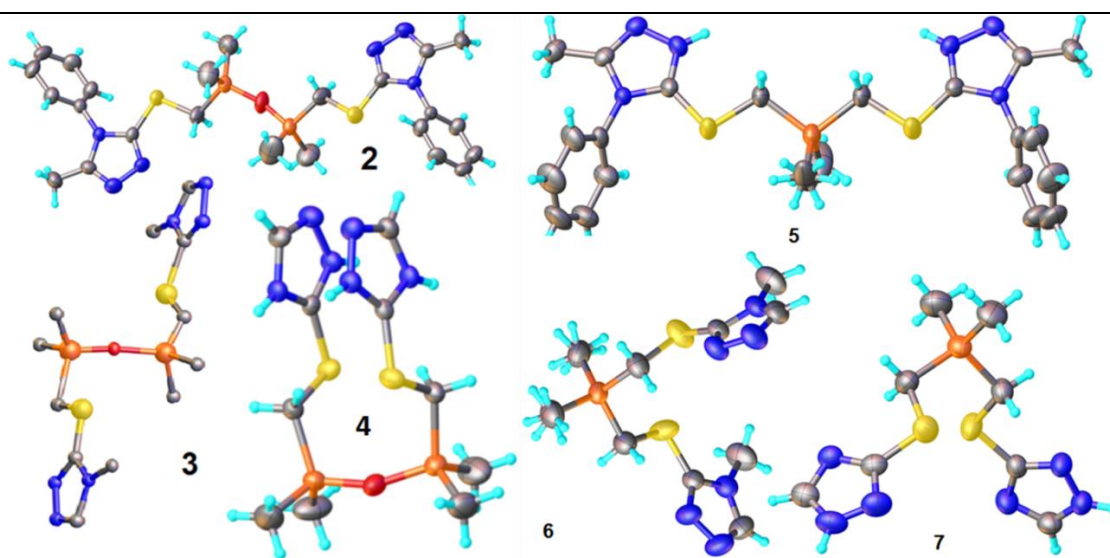


Figure 7. The conformation of the synthesized bis-triazoles [32].

Assessment of antimicrobial activity

Taking into account that triazole derivatives are often used in anti-infectious therapies, with triazole-based fluconazole being the first-choice antifungal agent, the newly synthesized here bis-triazole compounds have been evaluated as antibacterials and antifungals using *in vitro* testing against pure cultures of five fungi species (*Aspergillus niger*, *Penicillium frequentans*, *Penicillium fumigatus*, *Alternaria alternate*, *Fusarium*) and against selected Gram-negative (*Pseudomonas aeruginosa*) and Gram-positive (*Bacillus polymyxa*) bacteria. The results in Figure 8 indicate the antimicrobial activity of these compounds becomes more potent with the increasing concentration of the sample, and is definitely dependent on the nature of the solvent in which the tested compound is dissolved. Thus, the biocide activity in chloroform is better than the results obtained for the same compound in methanol. The best biological activity in the series of tested compounds has been recorded for compound 7 at a concentration of 1.5 wt% in chloroform.

Molecular docking

Molecular docking calculations were run to predict the inhibitory efficiency of our compounds and to identify the atomic scale interactions responsible for binding. Sterol 14 α -demethylase, a cytochrome P450 enzyme (CYP51A1) from *Aspergillus fumigatus*, a therapeutic target for many azoles was selected as a possible biologic effector, which could be inhibited by

the compounds presented in this study. The results of theoretical computations based on molecular docking are reflected in Figure 9.

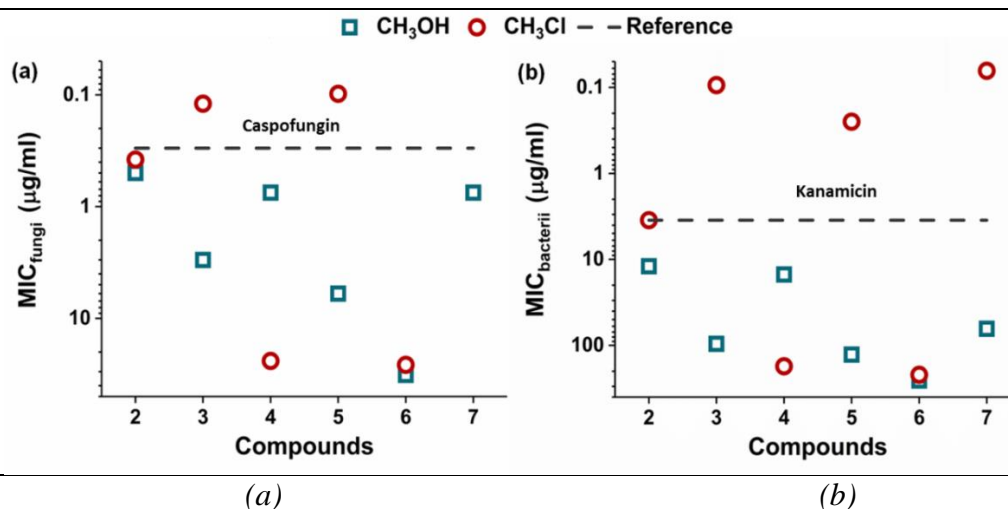


Figure 8. Comparative representation of antifungal (a) and antibacterial (b) activities (reported as minimum inhibitory concentration values, MIC) of bis-triazoles compounds 2 to 7, dosed as 1.5 % w/w solutions in methanol (M) and chloroform (C) [32].

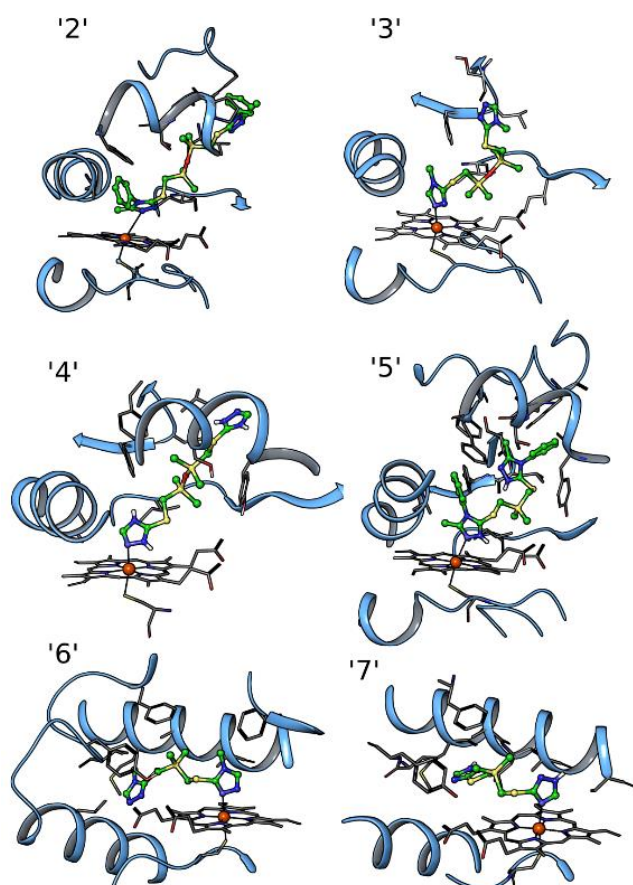


Figure 9. Molecular representation of the best binding modes for the six studied compounds as resulted from the docking calculations (ball and stick models).

Secondary structure elements lining the 14 α -Demethylase (CYP51) active sites are represented as ribbons. The heme group and residues important for binding are depicted as sticks. Iron was represented as an orange sphere.

In silico results show both hydrophobic and hydrophilic interactions between ligands and receptor, as well as π - π stacking interactions in the stabilization of docking complexes, but the hydrophobic interactions are predominant. Interestingly, all docked complexes show the triazole-based ligands directly coordinating the heme ferric iron (residue 601A) with nitrogen atom,

where Fe atom plays the role as acceptor of electrons and nitrogen as a donor of electrons. The calculated binding affinities, expressed as K_d constants, are presented in Table 1 and these are in the same range as experimentally measured K_d s for medical azoles [33].

Table 1. Calculated dissociation constants (K_d) for the complexes of the six triazoles-based ligands with the active site of *14 α -Demethylase (CYP51) enzyme.*

Compound	K_d (μ M)
2	4.58×10^{-4}
3	0.428
4	2.52
5	5.14×10^{-3}
6	2.98
7	10.35

Pairs of identical triazole cycles are coupled through thioalkylation reaction to a relatively long and flexible siloxane or silane spacer resulting in a library of compounds of organic-inorganic and hydrophobic-hydrophilic nature having behaviors accordingly, i.e. low glass transition or self-assembling ability sensitive to the polarity of the environment. The compounds show high biological activity proven both experimentally and through theoretical calculations.

II. – Design, synthesis, characterization and application of heterografted, amphiphilic "Hairy-Rod"-like polythiophene as electroactive surfaces in biomedical field

Premises for the topic's approach

- Imparting electroactivity to polymer biomaterials and integration of biomaterials to soft electronics, are two current hot topics which converge toward conjugated polymers (CPs), whose introduction into biomaterials field tailor them into smarter and more advanced ones [34-36].
- Nanostructuring by self-assembly, involving amphiphilic species, has increasingly emerged as an elegant "bottom-up" approach for the design and fabrication of reproducible nanoscale structures, both in solution and the solid state [37], and was shown as a useful, low cost and large scale technique to bring novel capabilities for both synthetic polymers biomaterials [38] and for CPs [39].
- Amphiphilic graft CPs are versatile and interesting construction of **rod-coil** type, with capability for various biomedical applications (bioimaging, drug delivery, imaging-guided therapy, tissue engineering or biosensors) [40] but, despite their technological relevance and fundamental interest, the SA of **rod-coil graft** CPs [41] remains much less explored and understood in many respects, (morphological control, hierarchical self-assembly, etc), by comparing with that of **rod-coil block** CPs.
- Being of great importance to develop easy-to-handle approaches to construct novel topological macromolecules, amphiphilicity can be also introduced into **graft rod-coil** CPs by attaching both hydrophilic and hydrophobic grafts along the conjugated backbones, in a statistical manner, obtaining a heterografted structure. It is important to notice that SA of amphiphilic graft copolymers, having two statistically distributed types of immiscible grafts is very complex and largely dependent on their hydrophilic-lipophilic balance (HLB) [42] and on the structural parameters (including graft length, graft ratio, backbone length [43] as well as on the monomer sequence and chain flexibility [44]. This allow for a multitude of possibilities to manipulate the copolymer's properties by these parameters variation in a controlled manner.

- An amphiphilic, statistical, heterografted conjugated copolymer of $(A-g-B)_m-ran-(A-g-C)_n$ type, due to its complex topology and composition, is endowed with multifunctionality, in order to function as an efficient and biocompatible electronic interface.

Design and synthesis of heterografted, amphiphilic copolymer PTh-g-(PEG-r-PCL)

In our design strategy we started from the point that biodegradable and biocompatible block copolymers based on polycaprolactone (PCL) and polyethyleneglycol (PEG) units (Figure 10) form a commercially available, important class of amphiphilic macromolecules useful for drug delivery, bioimaging or tissue engineering applications.

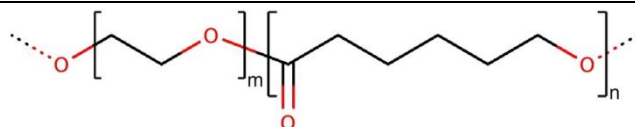


Figure 10. The chemical structure of poly(ethylene glycol)-*b*- Poly(ϵ - caprolactone) (PEG-*b*-PCL).

Moreover, the building blocks, PEG and PCL, are FDA approved polymers and, in aqueous media, linear block PCL-*b*-PEG copolymers form self-assembled nanostructures with PCL as the hydrophobic core and PEG as the hydrophilic corona-like structure. PCL is biodegradable and PEG is removed from the body by bioelimination (Gou, M.L. et al, 2009; Li, Z. et al, 2014)[45].

For **rod-coil** PTh-*g*-(PEG-*r*-PCL) (the molecular structure of which is shown in Figure 11 (iii)), the material's design criteria took in account the final copolymer architecture, nature (amphiphilic), type and properties of each structural motifs, encoding in its molecular peculiarities, based on a biomimetic approach [46], three types of intra- and/or intermolecular directional and non-directional interactions in solution, in melt and in bulk (like π - π intermolecular, hydrophilic / hydrophobic and hydrogen-bonding interactions). All of these endowed the copolymer with multifunctionalities and versatility for various types of bioapplications. Thus:

- Branched architecture was chosen because the obtained self-assembled nanostructures can show a higher drug loading capacity and storage stability [47] besides a longer *in vivo* retention times [48].
- The copolymer amphiphilicity allow for control and manipulation of film surface morphology and hydrophilicity as very influential parameters affecting cell adhesion, spreading and growth in tissue engineering [49], while amphiphilic copolymer coatings phase-separated on the length scale of biomacromolecules have significant potential to prevent bacterial infections on implanted medical devices(due to compositional heterogeneities which disrupt their adhesion mechanisms) [50].
- Fluorescent nanoparticles, dispersible in aqueous solutions, could be obtained by nanoprecipitation or by dialysis of PTh-*g*-(PEG-*r*-PCL), due to its amphiphilic character and due to the presence of the photoluminescent PTh main chain, meanwhile the oligo- ϵ -caprolactone and PTh hydrophobic moieties providing an appropriate compartment for hydrophobic bioactive principle loading.
- The electro-, photo- and electrochemically active PTh main chain can enable to the new copolymer a lot of bioapplications, specifically related to these properties. For example PTh-*g*-(PEG-*r*-PCL), containing both PEG and oligo- ϵ -caprolactone (an hydroxyl-ended oligoester) as side chains, could be an efficient aqueous electrolytes-compatible, redox-active material due to its mixed electron/ion conducting capability.

The new amphiphilic heterografted copolymer was synthesized in hierarchical fashion, by combining the so-called "macromonomer" or "grafting through" technique, with oxidative

polycondensation reaction of an equimolar mixture of two thiophene-ended macromonomers (see Figure 11), a method common for CPs chemical synthesis.

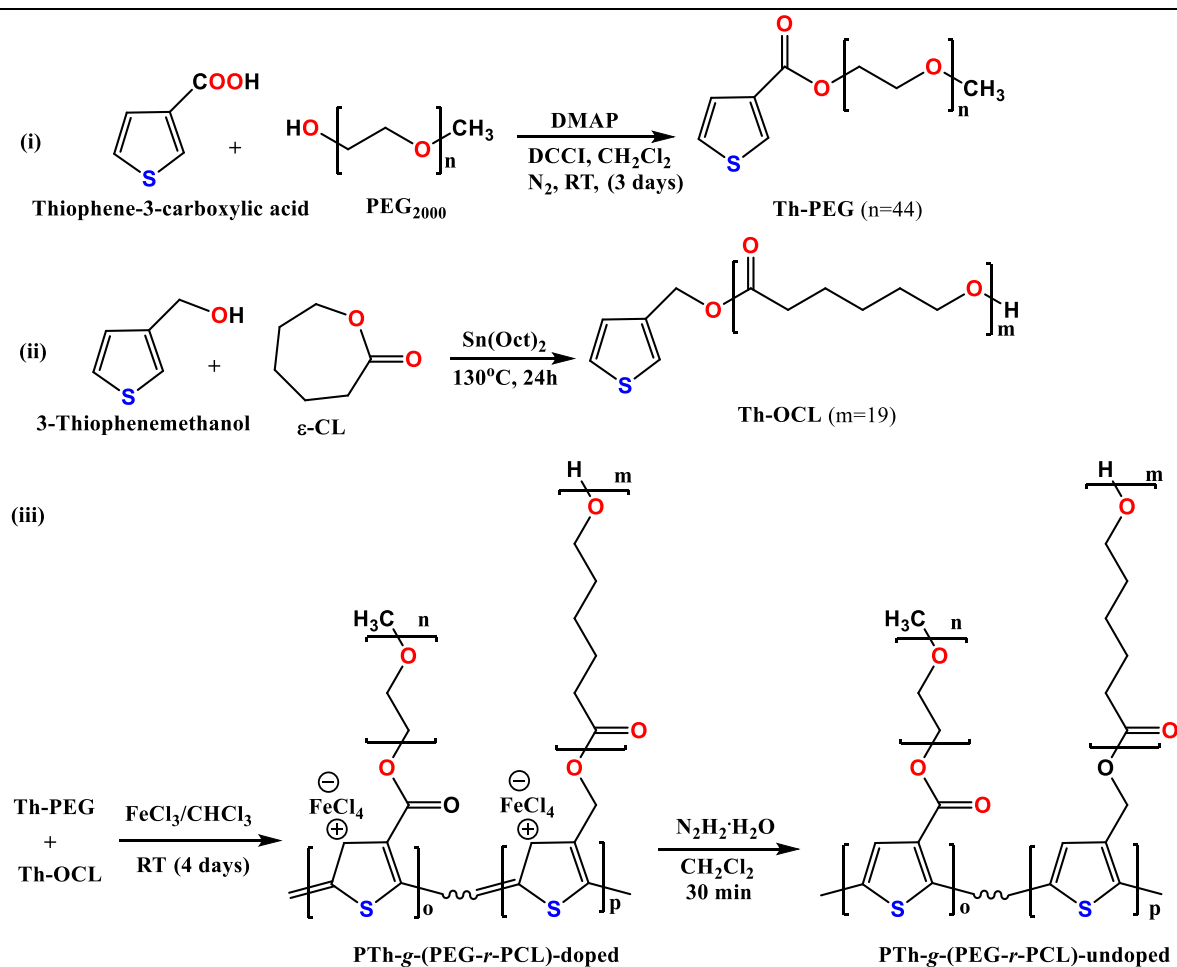


Figure 11. Synthesis of PTh-g-(PEG-r-PCL) copolymer.

(i) Esterification reaction of thiophene derivative and PEG2000.

(ii) Ring-opening polymerization of ϵ -caprolactone initiated by thiophene methanol.

(iii) oxidative polymerization of macromonomers from (i) and (ii) and dedoping reaction with hydrazine.

Physical-chemical characterization of the synthesized compounds

A. Structural characterization

The structural characterization of the macromonomers (Th-PEG and Th-OCL; (i) and (ii) in Figure 11) as well as of the statistical amphiphilic copolymer PTh-g-(PEG-r-PCL) was performed by complementary using FTIR and NMR spectroscopy techniques. The results of these investigations not only allow for demonstration of the accurate obtainment of the mentioned compounds but also enabled the assessing of the copolymer's composition (as 60% PCL side chains and 40% PEG side chains) as well as the calculation of its hydrophilic-lipophilic balance (HLB); the value of 0.36 characterizes an amphiphilic, non-water-self dispersible material. Interesting information was obtained by analyzing ^{13}C -NMR spectrum of the copolymer (Figure 12a) and, for a more accurate assignment of the signals, a DEPT 135 ^{13}C -NMR registration (Figure 12b) was performed, this technique actually being more sensitive than normal acquisitions.

An intriguing phenomenon took place during the ^{13}C -NMR registration of copolymer spectrum in acetone-d₆, which was reflected on the spectrum shape. More precisely, only the signals attributable to the C atoms of thiophene rings directly connected with an H atom in the copolymer structure (Figure 11 (iii)) were discernible in the spectrum.

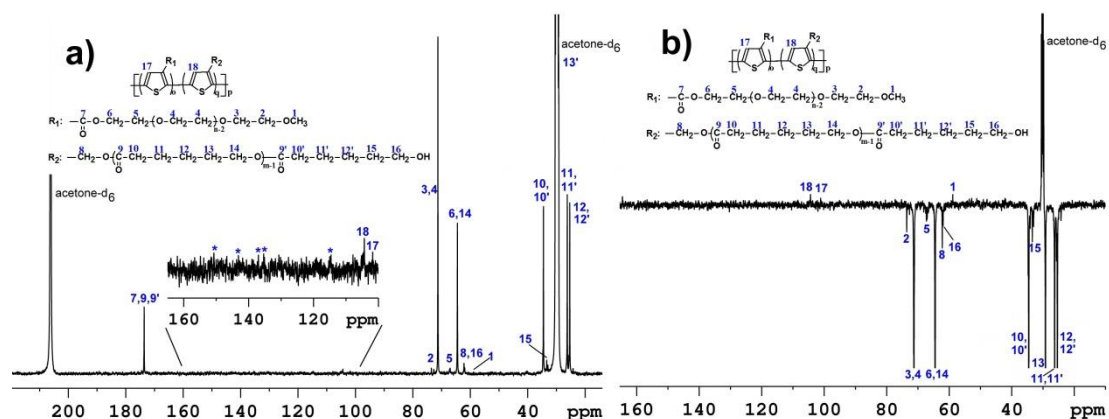


Figure 12. (a) ^{13}C -NMR and (b) DEPT $135\ ^{13}\text{C}$ -NMR spectra of the PTh-g-(PEG-r-PCL) copolymer, in acetone- d_6 . R_1 and R_2 represent the PEG and PCL side groups.

The noticed phenomenon in ^{13}C -NMR registration of PTh-g-(PEG-r-PCL), can be explained based on combination of two factors: (i)-the grafted side chains, both of them in extended configuration in a good solvent acetone, restrict the mobility of the rigid, hydrophobic polythiophene main chain for which acetone is a bad solvent, leading to small peaks broadening making them hardly to discern; (ii)- the side chains at high grafting density can shield the polythiophene main chain carbon atoms resonance. These experimental data suggested that in acetone the polythiophene main chain form a central solid-like hydrophobic core, while the side chains can function as a sheath and that the thiophene rings in the main chain are oriented such that to expose their β -position toward the side chains, while the more hydrophobic methoxy group of PEG side chains is oriented toward more hydrophobic inside of the structure. Given the side chains different nature and their inherited incompatibility, from the obtained results also it can get the conclusion that in acetone the copolymer chains segregated lengthwise by intramolecular self-assembling.

B. Optical and electrochemical properties of copolymer

An anomalous phenomenon was also noticed referring to photophysical properties of the random, heterografted copolymer. Thus, sharp absorption band which is usually found in polythiophenes around 400 nm, attributable to conjugated main chain, was missing from the UV-vis spectrum of PTh-g-(PEG-r-PCL) (Figure 13).

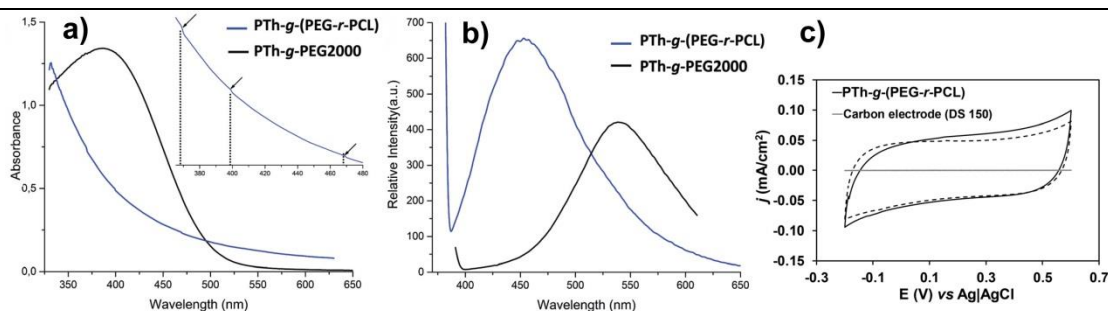


Figure 13. UV-vis (a), fluorescence (b) spectra of the random copolymer compared to previously reported PTh-g-PEG2000, in acetone at a concentration of $1\ \text{mg}\ \text{ml}^{-1}$; $\lambda_{ex} = 400\ \text{nm}$, and (c) the cyclic voltammograms of PTh-g-(PEG-r-PCL) in PBS solution.

This copolymer's behaviour was attributed to the introduction of PCL side chains besides the PEG ones, based on the UV-vis results obtained in similar conditions for a polythiophene having only PEG side chains.

By means of cyclic voltammetry (Figure 13c) were evaluated the electroactivity and electrostability of the copolymer in the film form deposited onto a carbon electrode. Experiments were conducted in PBS solution, which mimicked a physiological electrolytic medium and their results emphasized a material with a significant charge storing capacity as well as a high stability to redox processes.

Study of the self-assembly and of the morphology in thin films

In order to understand copolymer-solvent interaction and whether its chains are intermolecularly associated or not due to non-covalent supramolecular interactions, a dynamic light scattering (DLS) determination in acetone was performed. DLS measurements, which are much more sensitive to the bigger objects than to the smaller ones, showed the presence of three types of supramolecular aggregates, with size varying from 976 nm to 31 microns and to 146 microns.

Based on the properties of the acetone and on its selectivity toward particular components of the copolymer, as well as based on the architectural peculiarities of the copolymer it was concluded that multichains aggregation can be favored and enhanced by a synergistic combination of π - π stacking and intermolecular oligo- ϵ -caprolactone hydrogen bonding. As resulted from NMR measurements the copolymer chains exist as core-lengthwise-segregated sheath structures that can form intermolecular π - π stacks because PEG side chains in the hydrophilic half-sheath may be too short and/or too loosely grafted to prevent the main chains interaction. All of these can explain the obtained results by DLS.

Thin films morphology was investigated by SEM and TEM microscopy techniques (Figure 14) by a detailed study. The obtained results revealed the high dependency of the formed supramolecular structures on the solvent quality in relation with each component of the copolymer, on the solutions concentration and on the supports nature used for film deposition.

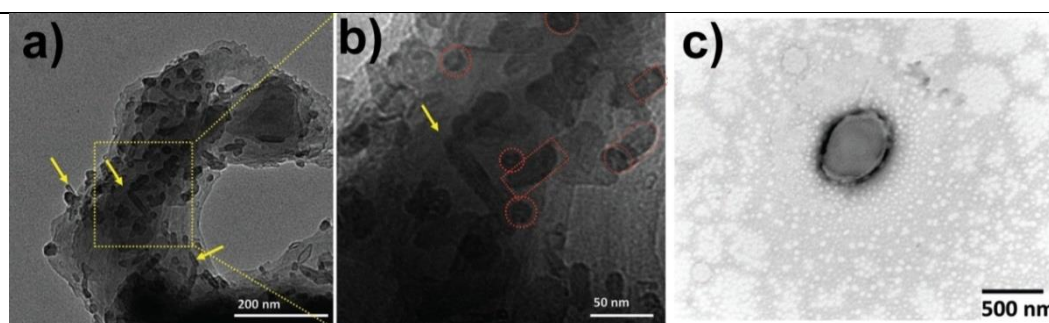


Figure 14. TEM micrograph of PTh-g-(PEG-r-PCL) obtained: (a) and (b) from a solution of 0.004 mg mL^{-1} in acetone, in unstained form, and (c) with uranyl acetate staining. Rod like structures are highlighted with yellow arrows in (a) low magnification and (b) high magnifications images with straight rods, horseshoe- and pseudospherical-like structures highlighted with spherical and rectangular forms in red, in figure (b).

This study also confirms the important role of PTh main chain in copolymer's constitution played by its length, rigid shape and π -conjugated character which decisively influence the shape and size of the formed supramolecular structures by SA (Figure 15). In addition, TEM experiment of copolymer's film staining with an aqueous solution of uranyl acetate (Figure 14c) allowed to demonstrate that PTh-g-(PEG-r-PCL) can form a compartmentalized structure as demonstrated previously for linear ter- and multi blocks copolymers and, moreover, that it can function as an adaptive surface in aqueous environments.

Ex-vivo biocompatibility evaluation

The biocompatibility of PTh-g-(PEG-r-PCL) copolymer was evaluated by cell adhesion (after one day) and proliferation (after 7 days) assays (Figure 16a). Due to their fast growth,

fibroblast (Cos-1) and epithelial (Vero) cell lines were selected, while steel was used as control substrate. Quantification of cell adhesion onto copolymer film reveals higher viabilities than those of the steel control substrates, for both types of cell lines (~ 160% Cos-1 and ~ 120% Vero cells). Thus, for short period of time (24 h) PTh-g-(PEG-*r*-PCL) copolymer do not show any cytotoxic effects acting as excellent supportive matrices, especially for the Cos-1. After seven days of culture, a slight reduction of the relative cell viability (12% for Cos-1 and 30% for Vero cells) on PTh-g-(PEG-*r*-PCL) in comparison to steel was recorded.

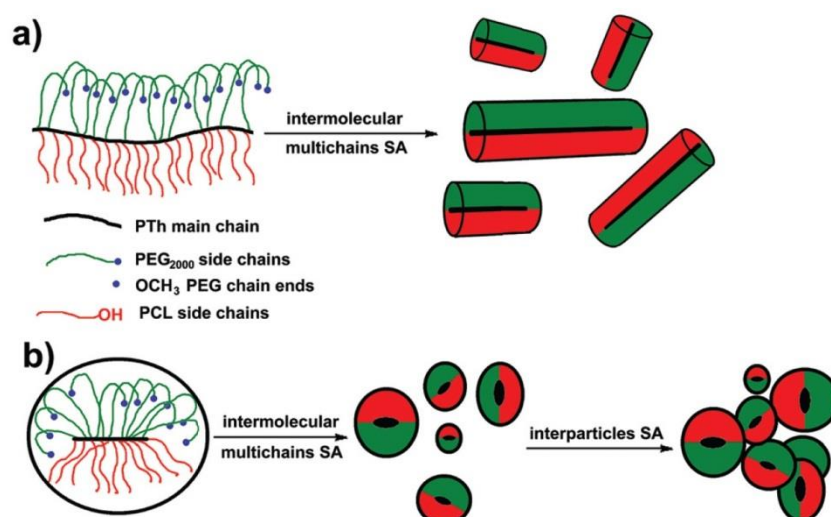


Figure 15. Schematic representation of the scenario for PTh-g-(PEG-*r*-PCL) copolymer self-assembling in both acetone solution and in thin film: (a) for longer PTh main chains, and (b) for short PTh main chains.

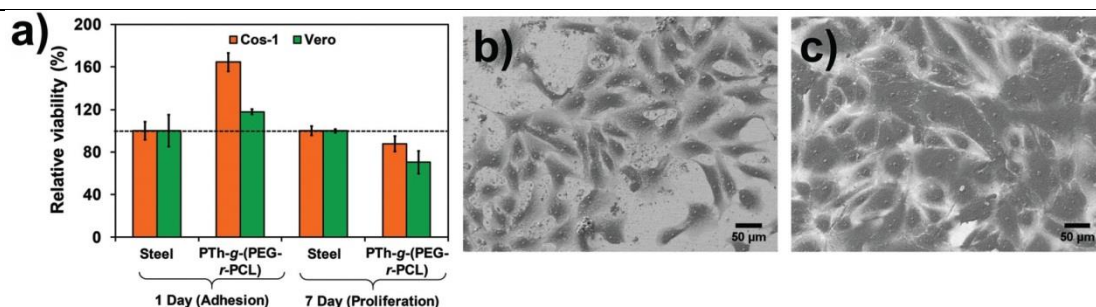


Figure 16. (a) Cellular adhesion and proliferation for the PTh-g-(PEG-*r*-PCL) amphiphilic copolymer using Cos-1 and Vero cells; (b) Cos-1 cells, and (c) Vero cells observed by SEM technique, after an incubation of 7 days.

It is well-recognized the poor adhesion of cells to the typically hydrophobic, neutrally charged, and low-surface energy semiconducting thin films [51] and PTh-g-(PEG-*r*-PCL) copolymer, with a composition of 40 % Th-PEG/ 60% Th-OCL, resulted as a high hydrophobic material, with a highly decreased HLB of only 0.36. If it is to also consider the recent report about the fact that pure PCL significantly decreased the viability of Vero cells [52], both these associated features could explain the reduction of cells proliferation on PTh-g-(PEG-*r*-PCL) film surface.

On the other hand, it is known that normal fibroblasts or epithelial cells, excepting adhesion, necessitate also an efficient spreading on the substrate for growth *in vitro* [53]. The obtained results induced the conclusion that PTh-g-(PEG-*r*-PCL) film surface properties highly stimulate adhesion of cells but subsequently the cells are most probably inhibited from spreading, resulting in a lower proliferation. However, as the cell morphology is a useful

indicator of a material biocompatibility [54] and as the SEM micrographs (Figures 16b, 16c) show an unaltered normal growth and characteristic morphology of both types of cells onto PTh-g-(PEG-r-PCL) films, allow to consider that, most probable, the reduction of cellular proliferation is a consequence of heterogeneous microscale surface topography combined with a certain surface chemistry of PTh-g-(PEG-r-PCL) copolymer.

Application of randomly heterografted copolymer in biosensing

Nowadays, the development of biosensing devices for the detection of β nicotinamide adenine dinucleotide (NADH) has gained interest because of its participation as enzymatic cofactor in more than 300 dehydrogenases and as electron carrier in cell processes associated to energy production. NADH is a vital coenzyme for metabolic redox reactions. NADH losses two electrons and delivers a hydrogen ion, as it becomes oxidized to NAD^+ . As the main role of NADH and NAD^+ in the metabolism is the transfer of electrons from one molecule to another, the balance between such oxidized and reduced species is called the NAD^+/NADH ratio. This ratio is an important parameter to certify the correct metabolic activity and the health status of the cells, among other functions.

By using cyclic voltammetry (Figure 17b) it was proven that PTh-g-(PEG-r-PCL) copolymer is able to catalyse the oxidation of of NADH molecules in PBS (pH=7.4) at 10 mM concentration and at a potential of 50 mV/s. Moreover, the results of differential pulse voltammetry (DPV) (Figure 17c) evidence that the copolymer catalyses the oxidation of NADH with good current density response in a low potential range. Even when the anodic peak current decreases with the concentration of NADH, the peak potential remains almost constant between 0.62-0.65 V, for all concentrations.

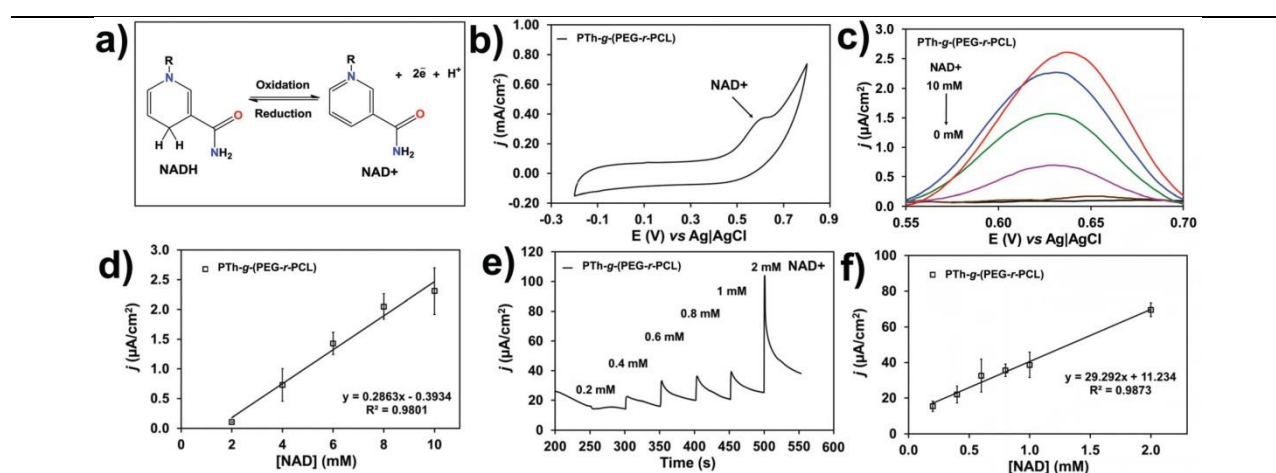


Figure 17. (a) Redox NADH/ NAD^+ reaction. (b) Cyclic voltammogram of PTh-g-(PEG-r-PCL) in a PBS solution containing 10 mM M NADH (scan rate = 50 mV s⁻¹). (c) DPV obtained for PBS solutions (pH = 7.4) containing a NADH concentration comprised between 2 mM and 10 mM. (d) Calibration curve for the NADH detection in a concentration range from 2 to 10 mM using the PTh-g-(PEG-r-PCL) copolymer. (e) Current density-time responses of PTh-g-(PEG-r-PCL) upon successive injection of a given concentration of NADH into the PBS solution (pH = 7.4). (f) Calibration curve for the NADH detection in a concentration range from 0.2 to 2 mM using PTh-g-(PEG-r-PCL).

The performance of copolymer as amperometric sensor for the detection of very low NADH concentrations has been also evaluated. The amperometric current density-time ($j-t$) response against the addition of NADH and the corresponding calibration plot were recorded (Figures 17e, 17f). A linear relationship with a regression coefficient of 0.9873 was obtained for NADH concentration interval between 0.2 to 2 mM (Figure 17f). This sensing capacity is simply achieved by depositing the copolymer microparticles onto a carbon electrode via drop-casting.

We attributed such sensor ability to the unusual topology of the copolymer, that is independent from the heterogeneous microparticle size, but with a positive influence of the presence of porous structure, that could allow the permeation of NADH molecules toward the thiophene inner units.

Having in mind the good sensitivity for low NADH concentrations, the sensibility of PTh-*g*-(PEG-*r*-PCL) particles to detect NADH oxidation was evaluated in the presence of ascorbic acid (AA) as interfering species. Accordingly, the selective determination of NADH in a mixture with AA was conducted using both CV and DPV (Figure 18). The voltammetric curve recorded for PTh-*g*-(PEG-*r*-PCL) in a 0.1 M of PBS solution with of 5 mM of AA and 5 mM of NADH showed two distinctive oxidation peaks, which have been attributed to the oxidation of AA (lower potential) and NAD⁺ process. The differential pulse voltammogram presents two well defined oxidation peaks at 300 and 580 mV that correspond to AA and NADH, respectively. The peak separation of 280 mV indicates that the amphiphilic PTh grafted copolymer can be successfully used for selective detection of NADH in the presence of AA [55].

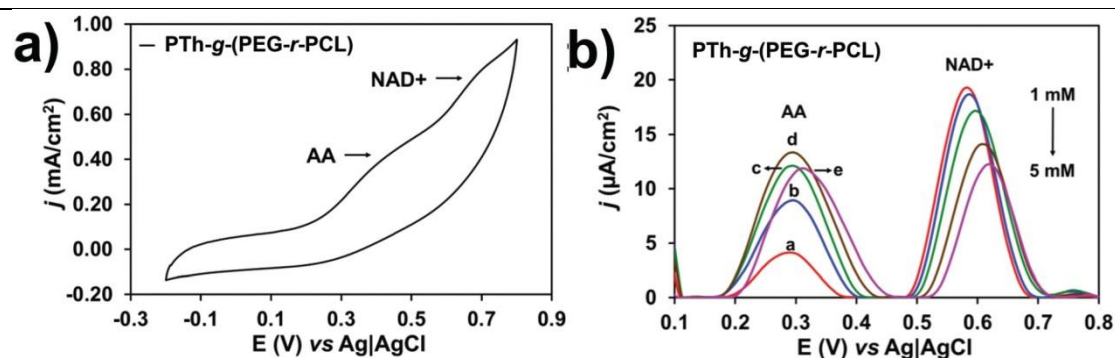


Figure 18. (a) Cyclic voltammogram obtained for PTh-*g*-(PEG-*r*-PCL) in a PBS solution with 5 mM NADH and 5 mM AA. Scan rate: 50 mV s⁻¹. (b) Differential pulse voltammogram obtained for PTh-*g*-(PEG-*r*-PCL) in a PBS solution with 5 mM NADH and a variable concentration of AA (from the lowest, a = 1 mM; to the highest concentration, e = 5 mM).

As a conclusion, in this stage of the project, by intelligently combining the components of a well-known polymeric biomaterial (PCL-*b*-PEG) with a multi-sensitive conjugated polymer (PTh), working on the composition, on the structural details and on the architecture, we produced a biomimetic, multifunctional and versatile polymeric material. Its biomimicry is reflected in its elementary constitutes kinship with biomolecules, in its amphiphilicity similitude and in its self-assembling ability and not in the last in its compartmentalization ability in a similar manner with the key feature of biological cells.

A.3. Producing and preliminary testing of extracellular matrix / tumors surrogates dedicated to the *ex vivo* evaluation of supramolecular nanoplateforms

Regardless the application, *ex vivo* experiments should be performed in quasi-real conditions from the point of view of (macro)molecular and morphological environment, which must mimic (as close as possible) the tissue that will host the bio-medical effectors. In this respect, during 2019 stage, we developed and tested five types of (connective tissue) surrogates.

I. – Design and development of sponge-type hydrogels composed of hyaluronic acid and poly(methylvinylether-*alt*-maleic acid) as surrogates for bio-medical testing

Sponge-type hydrogel (SpGH) based on hyaluronic acid (HA) and poly(methylvinylether-*alt*-maleic acid) (P(MVEaltMA)) cross-linked by solvent free thermal method was synthesized

and characterized. First, aqueous solutions containing different weight ratios of HA and P(MVEaltMA) were mixed. Solutions were quickly frozen in liquid nitrogen and then freeze-dried for 48 h, until all the water was eliminated. The resulting sponge-type samples were obtained in cylinder-like pieces. These samples were not cross-linked and therefore they were soluble in water. In order to obtain cross-linked hydrogels, the samples were subsequently placed in the oven for 12h at 80 °C. The resulted cross-linked SpgH were kept for 2-4 days in a large amount of water, frequently refreshed to remove the soluble fraction of polymer residues. Finally, the SpgH was recovered by frozen in liquid nitrogen and then freeze-dried for 48 h. The schematic representation of the synthesis steps of the SpgH is given in Figure 19.

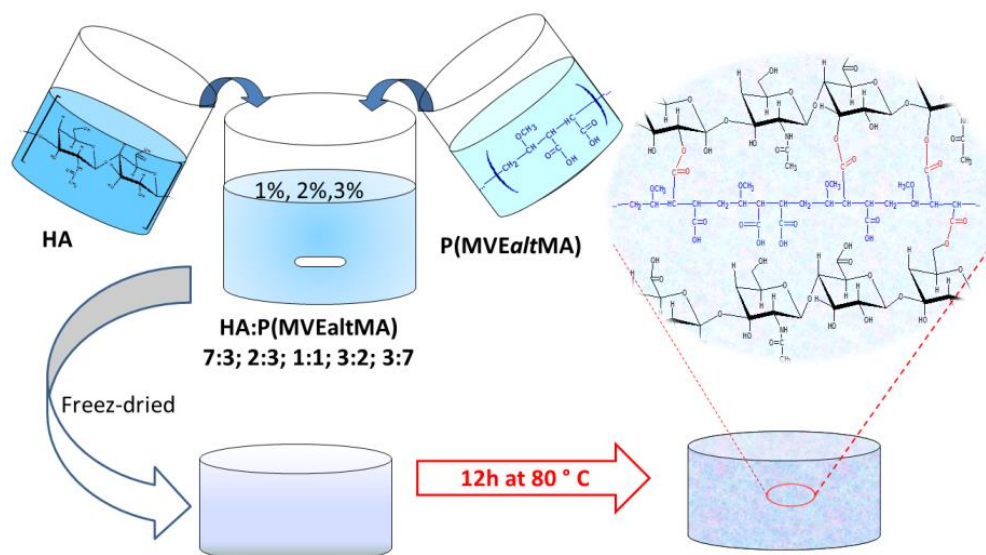


Figure 19. Schematic representation of the steps of preparation process sponge-type hydrogels.

For preparing sample of hydrogel, the polymer concentration was varied from 1 to 3 % w/v, and the content of each polymer from 30 to 70 % (w/w). The samples were coded as HA^xPMAY, where “x” is the polymers concentration used in synthesis feed, and “y” the content (% , w) of P(MVEaltMA). The composition of the reaction mixture for each sample is given in Table 2.

Table 2. Feed compositions used in synthesis of sponge-type hydrogels.

Samples code	Feed composition			Yield (%)
	HA (g)	P(MVEaltMA) (g)	Water (mL)	
HA ¹ P30	0.7	0.3	99	-
HA ¹ P40	0.6	0.4	99	55.3
HA ¹ P50	0.5	0.5	99	96.5
HA ¹ P60	0.4	0.6	99	54.8
HA ¹ P70	0.3	0.7	99	-
HA ² P40	1.2	0.8	98	72.6
HA ² P50	1.0	1.0	98	96.0
HA ² P60	0.8	1.2	98	77.6
HA ³ P30	2.1	0.9	97	92.5
HA ³ P50	1.5	1.5	97	89.2
HA ³ P70	0.9	2.1	97	78.0

The main evidence of the cross-links formation is the swelling in water of SpgH network while the non-cross-linked SpgH dissolves quickly after immersing in water. As the hydrogels are designed to be used for biomedical applications, the swelling studies were carried out in simulated physiological conditions at different values of pH (7.4; 5.5; 1.2).

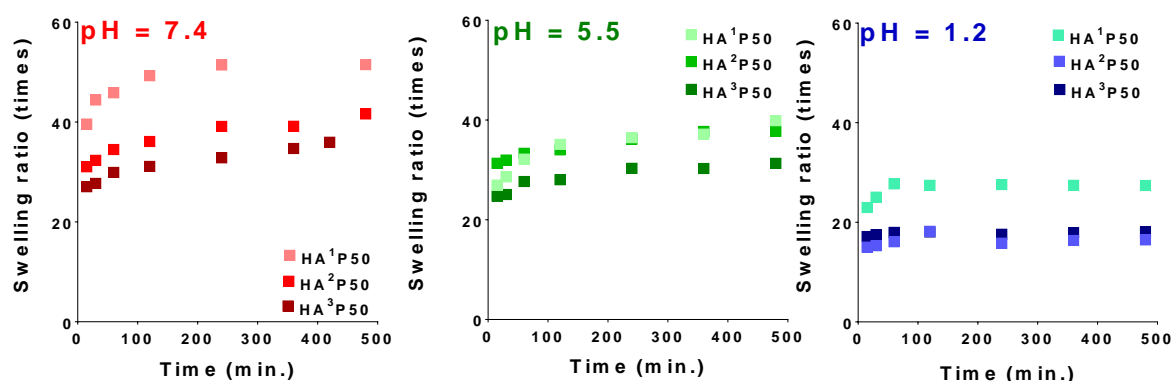


Figure 20. SpgH swelling kinetics at 25 °C, in standard solution at pH 7.4, 5.5, and pH 1.2.

The obtained swelling profiles showing a maximum swelling in less 2 hours for all pH values are presented in Figure 20. At alkali pH values swelling was higher as compared with the water absorption at acidic pH. The higher swelling at pH 7.4 is explained by the dissociation of COOH groups, preventing intermolecular hydrogen bonds and consequently yielding higher swellings. Moreover, the presence of extra negative charges in the structure will lead to an extra expansion of the network, due to the repulsion of the negatively charged chains.

SpgH characterization by SEM, ¹³C CP/MAS NMR, FTIR, and BET

From SEM images (Figure 21) it can be observed that the hydrogels have a more ordered and compact structure, and even larger pores with the increases of the concentration of polymers in the feed solution. Moreover, in longitudinal section of hydrogels, the SEM micrograph indicated that the hydrogels present lamellar structures arrangement, containing abundant pores between each layer, observable in cross-section.

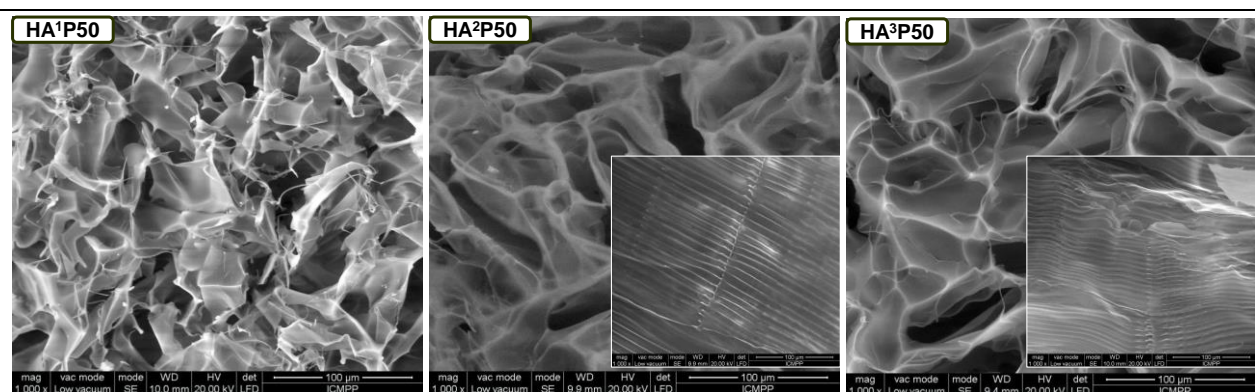


Figure 21. Scanning electron micrographs of three samples of SpgH.

The comparison of the ¹³C CP/MAS-NMR spectra of the original HA and P(MVEaltMA) with SpgH spectra confirms the formation of the ester bound by appearance of 2 new resonance signals at around 70 and 171 ppm (Figure 22). The FTIR spectra (Figure 23) also confirmed the ester bound formation as well as the anhydride bound formation for the un-washed hydrogels.

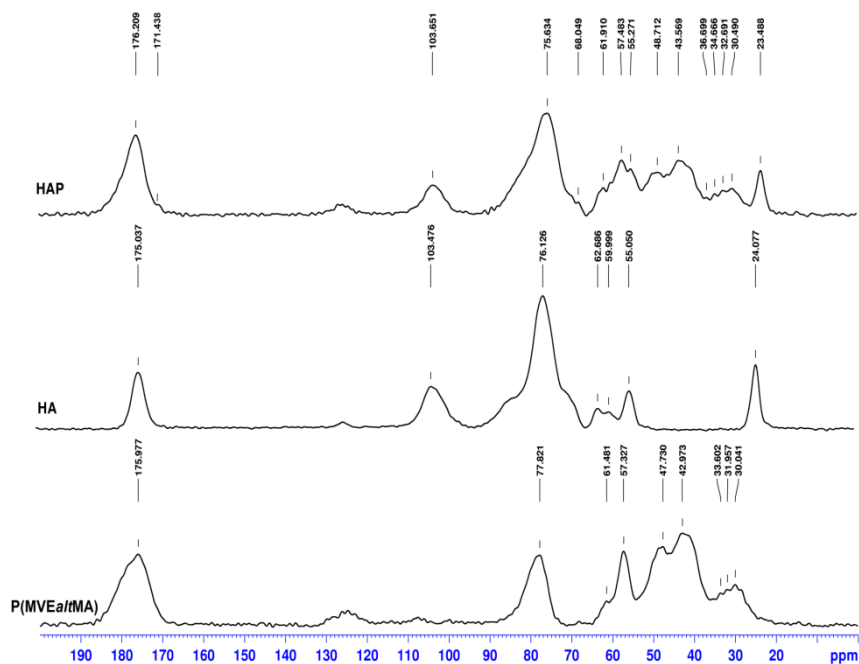


Figure 22. ^{13}C CP-MAS NMR spectra of P(MVEaltMA), HA and HAP.

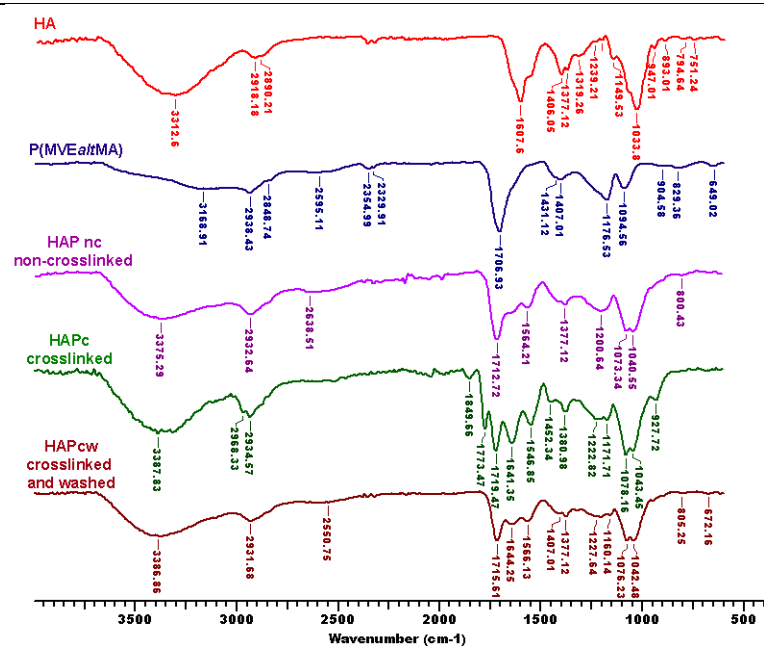


Figure 23. FTIR spectra of HA, P(MVEaltMA), HAPc (non-cross-linked), HAPc (cross-linked), HAPcw (cross-linked and washed).

The textural properties of the synthesized sponge type-hydrogels were studied by means of the nitrogen adsorption-desorption isotherms. The obtained isotherms (Figure 24) for SpgH (sample HA²P50), can be categorized as type IV, based on the IUPAC classification scheme. This type of isotherm in the presence of a hysteresis loop are characteristic for mesoporous structures with cylindrical pores. The BET surface area was found to be 8.033 m²/g with pore diameter of 16 nm.

Loading / release experiments

Diphenhydramine (DPH) was selected as a model molecule to evaluate the drug loading and release capacity of the SpgH. Since it is a cationic molecule it is expected to have high

loading capacity in hydrogels that are heavily negatively charged. Therefore, as it can be seen in Figure 25, the loading capacity increases with increasing of P(MVEaltMA) content in hydrogel, due to the electrostatic interactions. The release profiles of DPH from SpgH at different values of pH show that the release amount at pH 5.5 is lower than at pH 7.4 and 1.2, that suggests a strong binding of the drug to the negatively charged hydrogel network at this pH.

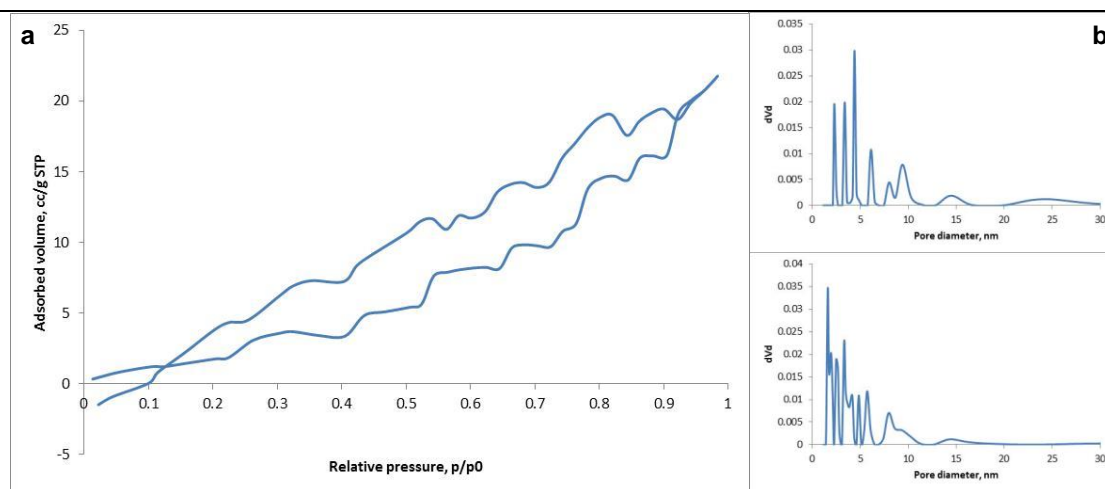


Figure 24. Nitrogen adsorption-desorption isotherms (a), and pore size distributions (b) in the case of HA²P50 sample.

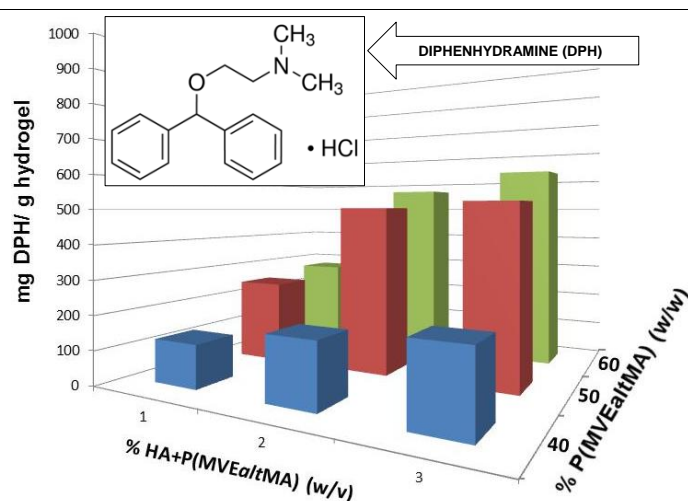


Figure 25. DPH loading capacity of SpgH samples.

II. – Alginate-poloxamer hydrogels produced by photo-initiated thiol-ene reaction

In situ forming hydrogels were obtained using thiol-ene reaction, a selective and fast reaction that can be performed under physiological conditions. Macromers (alginate and Poloxamer derivatives) were used instead of monomers in order to be non-toxic for the cells. UV irradiation at long wavelength was used for photo-initiation, procedure that will allow cell incorporation into the hydrogels.

Thiolated alginate (Alg-SH) (Figure 26a) was obtained by covalent attachment of cysteamine. The thiol group content was determined by iodometric titration and by ¹H NMR. The substitution degree was determined to be 20%. Diacrylated Poloxamer (PLDA) (Figure 26b) was prepared by reaction of hydroxyl end groups from Poloxamer 407 with acryloyl chloride. The conversion, determined by ¹H NMR was 98%.

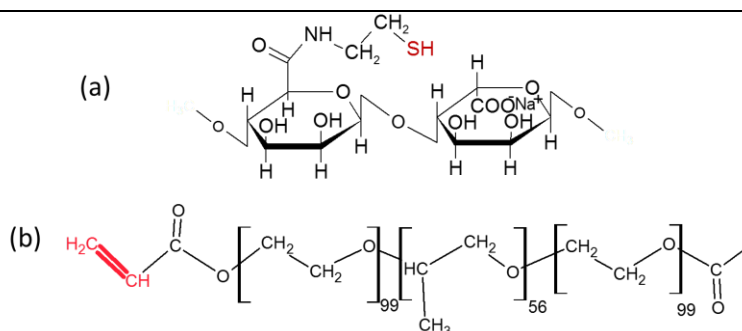


Figure 26. Thiolated alginate (Alg-SH) (a) and diacrylated poloxamer (PLDA) (b).

The hydrogels were prepared using the Alg-SH and PLDA (in different ratios) in phosphate buffer pH 7.4 and Irgacure 2959 as photo-initiator. The influence of the irradiation time, photo-initiator concentration, macromers concentration and ratio between the thiol and acrylate groups on the gel fraction were studied (Figure 27).

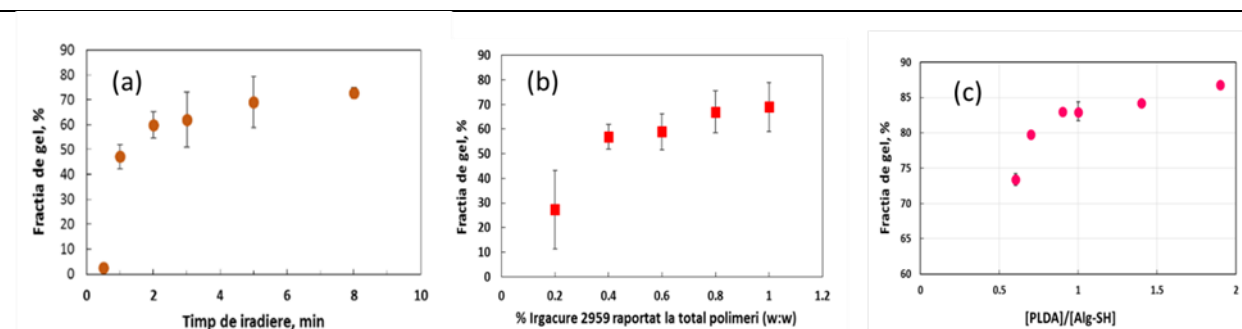


Figure 27. Gel fraction of the hydrogels obtained by photo-initiated thiol-ene reaction as a function of: irradiation time (a), photo-initiator amount (b), and ratio between acrylate groups and thiol groups (c).

An initiation of 5 minutes, 0.8 - 1% Irgacure 2959 to the total monomer amount and a 15% concentration of macromers are enough for relatively complete cross-linking. The gel fraction increases with the [PLDA]/[Alg-SH] weight ratio, showing that PLDA acts as a bi-functional cross-linker. At 1:1 [PLDA]:[Alg-SH], the gel fraction was around 83% but increase slowly with further addition of cross-linker. The morphology of the hydrogels obtained with different [PLDA]:[Alg-SH] ratio was studied by SEM (Figure 28) and it can be observed that the increase of PLDA amount leads to a decreased porosity.

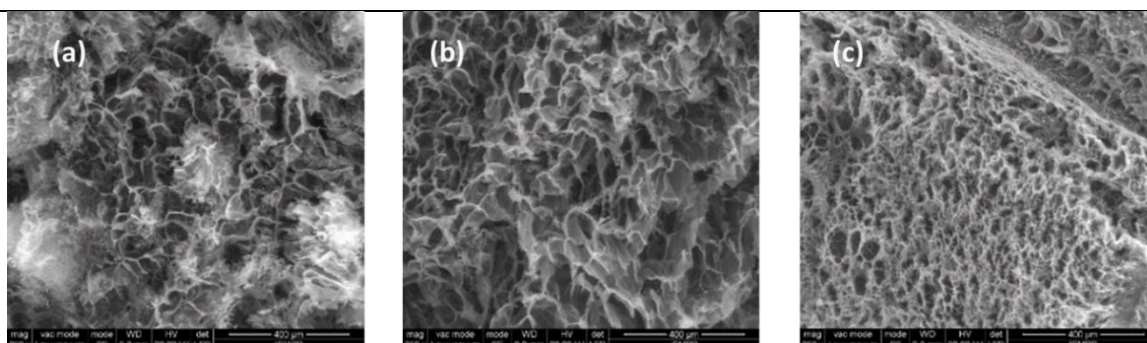


Figure 28. SEM images of free-dried hydrogels obtained with different [PLDA]: [Alg-SH] weight ratios: 0.7 : 1 (a), 1 : 1 (b), 2 : 1 (c).

The swelling degree of the hydrogels decreases with the increase of the [PLDA]: [Alg-SH] weight ratio. The mechanical properties of the hydrogels are also influenced by the hydrogel composition (Figure 29). With the increase of PLDA, that plays the role of the cross-linker, the compressive modulus and the stress at break increase.

It is known that Poloxamer is a thermosensitive copolymer. The swelling degree of our hydrogels is also influenced by the temperature, as shown in Figure 30. The hydrophobic interactions of PPO blocks become stronger with the temperature increase, so the micellar structures of Poloxamer entrapped in the hydrogels become more collapsed and water is expelled from the hydrogels.

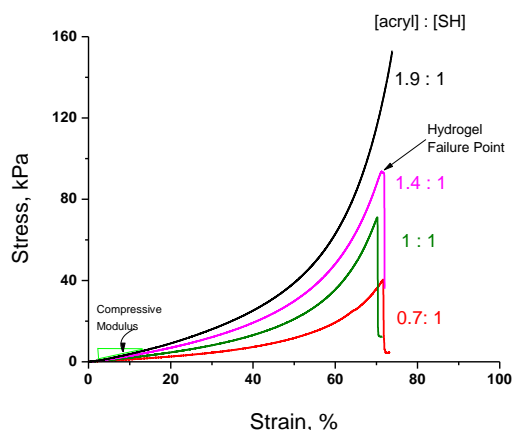


Figure 29. Uniaxial compression of cylindrical hydrogel samples with different macromer ratios.

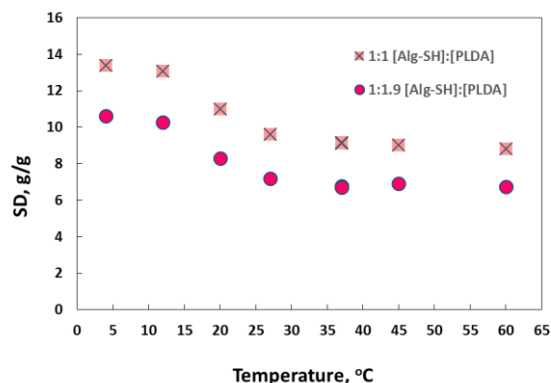


Figure 30. Influence of the temperature on the swelling degree of hydrogels in phosphate buffer (pH 7.4).

In order to obtain information about the permeability of the hydrogels, the release of FITC-dextran with different molar mass from the hydrogels was investigated (Figure 31). A amount of 70-80 % of the FITC-dextran with low molar mass (10 kDa) was released in several hours, but the FITC-dextran with high molar mass (150 kDa) was released more slowly. In this case the release rate is also influenced by the porosity of the hydrogels: with the decrease of the pores, meaning with increase of [PLDA]/[Alg-SH] ratio, the release of the marked macromolecules was retarded.

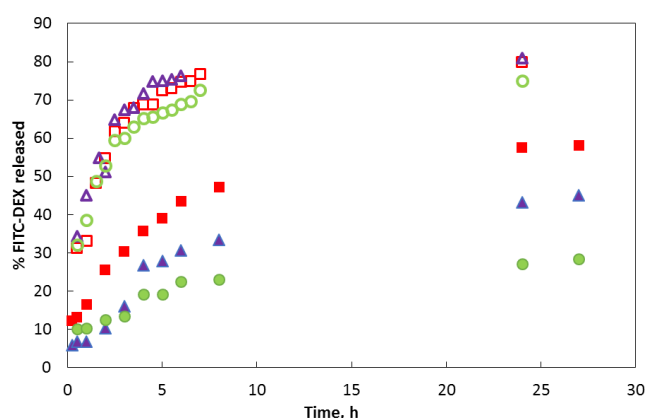


Figure 31. Release profiles of FITC-Dex $M_w=10$ kDa (empty symbols), and FITC-Dex $M_w=150$ kDa (filled symbols) from the hydrogels with different [PLDA]: [Alg-SH] ratios: 0.6 : 1 (squares), 1 : 1 (triangles), and 2 : 1 (circles).

III. – Polysaccharide / poly(vinyl alcohol) hydrogels as tissue surrogates

The oxidation of polysaccharides represents one of the most suitable approach to introduce new functionalities, i.e. aldehyde, ketone or carboxylic, able to serve for further derivatisation or as anchoring sites of different molecules, broadening the applications area of these products.

New types of hydrogels were prepared, made by using various amounts of carboxyl pullulan or water soluble tricarboxy cellulose, (ranging from 0.1% to 25% (wt.) acting as a

multifunctional key component: due to its particular structure, bearing three $-\text{COOH}$ groups per anhydroglucose unit, fulfills the role of a cross-linker agent), and poly (vinyl alcohol) (PVA).

The first step involves the polysaccharide's oxidation in the presence of TEMPO, NaClO, NaBr, which affords selectively carboxyl pullulan (OxP) and 6-carboxy cellulose (OxC), with different carboxyl content depending on the reaction time, amount of the NaClO, pH, temperature, etc. When the amount of the introduced carboxyl groups is low (generally as low as 0.59 mmol g^{-1}) the product keeps its insolubility in water, while the oxidized samples having more than 0.60 mmol g^{-1} carboxyl groups are becoming water soluble (see Figure 32). The water soluble 6-carboxy cellulose and carboxyl pullulan obtained after dialysis and freeze-drying were further utilised for the hydrogels preparation.

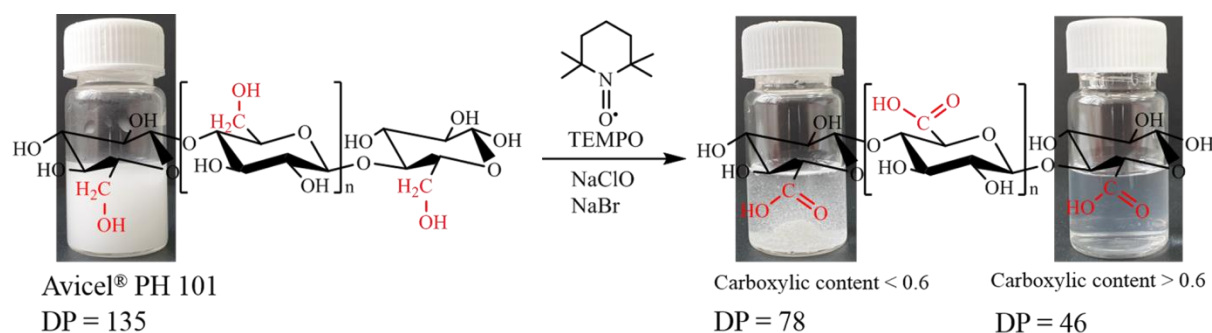


Figure 32. Schematic illustration of cellulose oxidation in the presence of TEMPO, NaClO, and NaBr.

We conducted a series of rheological deformation and recovery tests by following the evolution of G' and G'' versus time under successive low and high strain deformations applied to the hydrogels in order to evaluate the self-healing ability of the hydrogel. Damage of the self-healing hydrogel after a high shear strain (200%) and fast recovery of its structure after healing at the low strain (1%) were shown in Figure 33 for the sample with 7.5% OxP and 92.5% PVA. At the large dynamic strain, the G' value of the self-healing hydrogel decreased from 690 Pa to 110 Pa due to the collapse of the hydrogel network. At the low strain (1%), the G' of the self-healing hydrogel returned quickly to the initial value due to the recovery of the hydrogel structure. Furthermore, the G' and G'' of the original hydrogel and the hydrogel after experiencing cutting-healing process were measured. The hydrogel after experiencing cutting healing process showed nearly the same values of G' and G'' with the original hydrogel, which indicated the good self-healing capacity of the hydrogels.

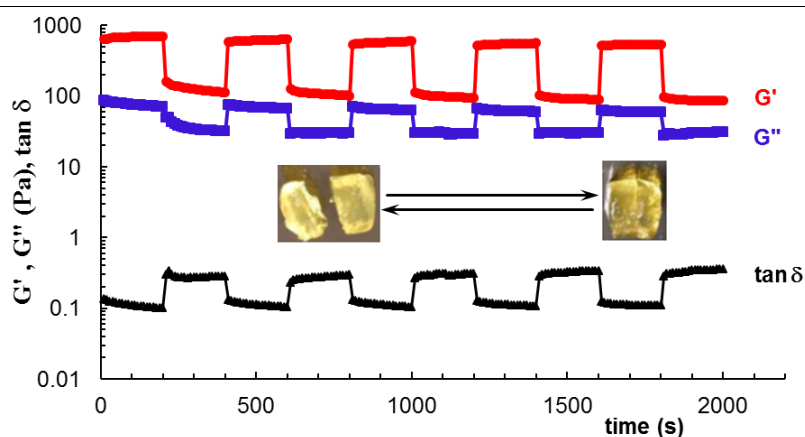


Figure 33. Self-healing test for the hydrogel with 7.5% OxP content by following the evolution of the viscoelastic parameters in time at 1 rad s^{-1} and $25 \text{ }^\circ\text{C}$; each 200 s, two successive levels of deformations were applied: 1 % and 200%, in the presence of TEMPO, NaClO, and NaBr.

The hydrogels prepared from PVA and carboxylated polysaccharides were in vitro tested for cytotoxicity, according to the ISO 10993-5:2009 standard recommendations. The results, depicted in Figure 34, reveal that all investigated samples are non-cytotoxic. As a general observation, the PVA/oxidized pullulan (OxP) hydrogels keep the cells metabolic activity in time. The best cytocompatibility has been found for the sample with OxP 10. In this case, after 72 h of exposure with cells, OxP 10 sample kept cell viability over 90%. This metabolic activity of the cells culture expresses their ability to adapt to in the vitro conditions. The MTT results recommend these hydrogels as surrogates for biomedical applications, since they do not release any cytotoxic compounds.

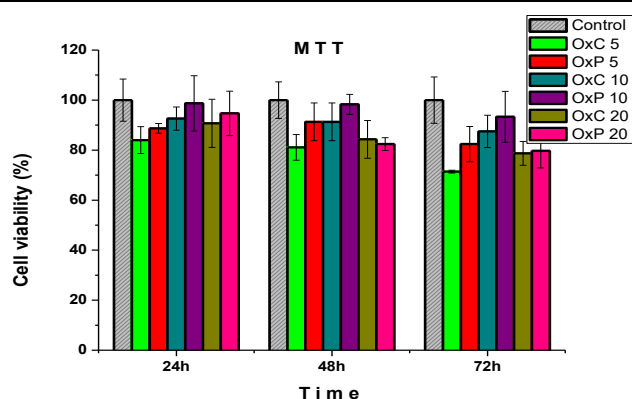


Figure 34. Significant results of the cytotoxicity evaluation, performed on the PVA/carboxylated polysaccharide hydrogels by using the MTT assay.

IV. – Curdlan and curdlan derivatives as surrogates for biomedical applications

Curdlan and its derivatives are promising for designing medical materials due to their biocompatibility and biodegradability properties. They can be used as solid matrices in different forms, such as hydrogels, beads, micro- or nanoparticles to incorporate drugs or as scaffolds for tissue engineering.

Hydrogels (HG) with different compositions were obtained by covalent cross-linking of curdlan (C) and phosphorylated curdlan (PC) using 1,4 butandiol diglycidyl ether (BDDE) as a cross-linker, at room temperature for 48h. The compositions of the samples are presented in Table 3.

Table 3. The compositions and main characteristic of the investigated samples.

Samples code	8% C : 8% PC	Exchange capacity, meq/g HG	Drug loading, mg TCH/g HG
0C-4PC	0:100	-	-
1C-3PC	25:75	6.1	131.4
2C-2PC	50:50	2.6	85.3
3C-1PC	75:25	1.1	78.0
4C-0PC	100:0	-	68.5

The structure of the HGs resembles a typical cross-linked network, with a porous, ‘sponge-like’ structure. The pores have different aspects and size, as a function of the proportion of the PC in hydrogels (Figure 35).

The swelling ratio of the hydrogels in time at 37 °C in PBS 6.8 increases with the increasing amount of PC as expected (Figure 36). Figure 37 comparatively presents the behavior of the hydrogel in water in absence and in presence of small amount of salt. As the pH increases above the pK_a of PC (pK_a = 2.8), the polar groups within the hydrogel structure become ionized and repel one another, causing the swelling of the hydrogel.

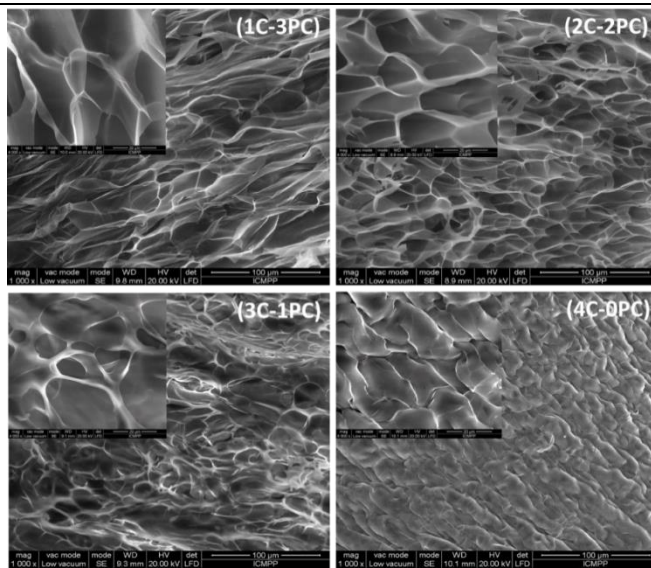


Figure 35. The morphology of the deided hydrogels with different composition.

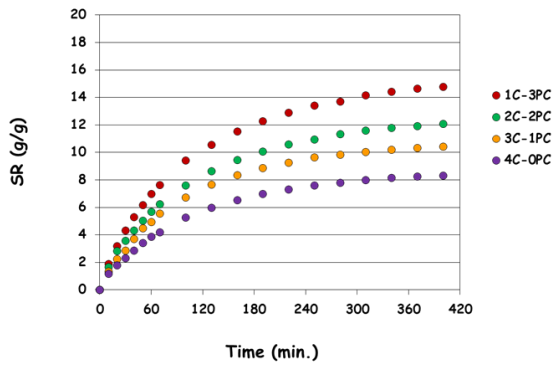


Figure 36. Evolution of swelling ratio of the HGs, in time, at 37 °C, in PBS 6.8.

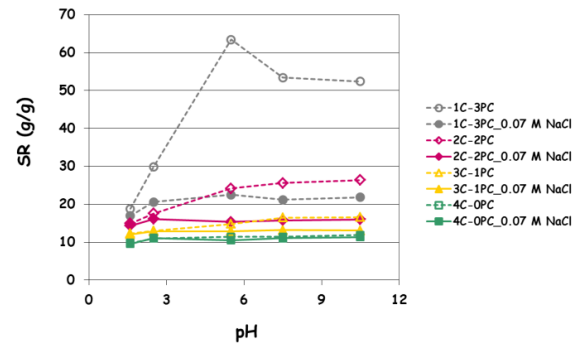


Figure 37. Variation of the HGs swelling ratio at different pH and ionic strength values.

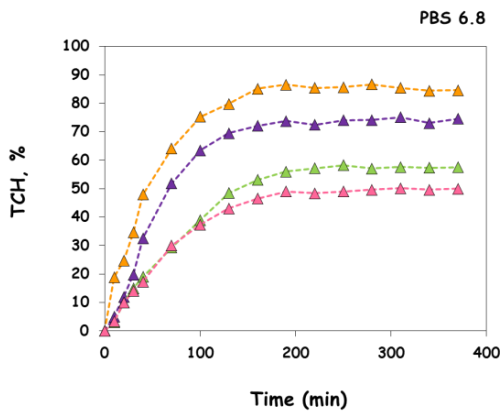


Figure 38. Variation of TCH release from HGs in time, in PBS 6.8.

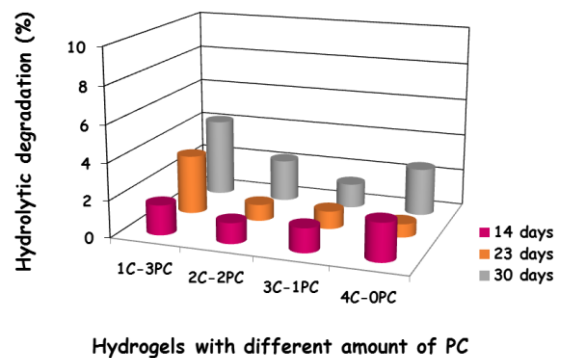


Figure 39. Hydrolytic degradation in PBS 6.8, during one month.

Drug loading capacity is largely influenced by the chemical structure of the matrix, the porosity and the exchange capacity of the polysaccharide-based matrix (Table 3). Drug loading experiments indicated that the adsorption increases with the amount of ionic component in the HGs. Release studies were performed under pseudo-physiological conditions or aqueous solutions with different ionic strength (Figure 38). The release rates depend in a greater extent to

As long as the pKa of the copolymer is approx. 8.7, under simulated physiological conditions (PBS at pH = 7.4), the amino groups are in protonated state, much more hydrophilic and thus the microgels are in the swollen state and lose the thermosensitive properties (Figure 41a). Under the same conditions (PBS at pH = 7.4), indomethacin (model biomolecule) showing a pKa = 4.5 is in the ionized form and highly reactive. After electrostatic interactions with the amino groups of APM, the hydrogel restores its thermosensitive properties (Figure 41b). At the human body temperature, the microgels collapse and can release a certain dose of drug (previously loaded), the dose being dependent to the degree of complexation with indomethacin (Figures 41c and 41d).

Biocompatibility assay

It is well-known that the cytotoxicity of a biomaterial is highly important for its biomedical applications. The cytotoxicity of poly(NIPAAm-co-APM) microspheres was investigated by MTT assay.

The extract resulted from microspheres incubation at different concentration of particles (0.5, 1.0, and 2 mg mL⁻¹) and tested for cytotoxicity through MTT method shows that poly(NIPAAm-co-APM) microspheres are completely devoid of toxicity (Figure 42a).

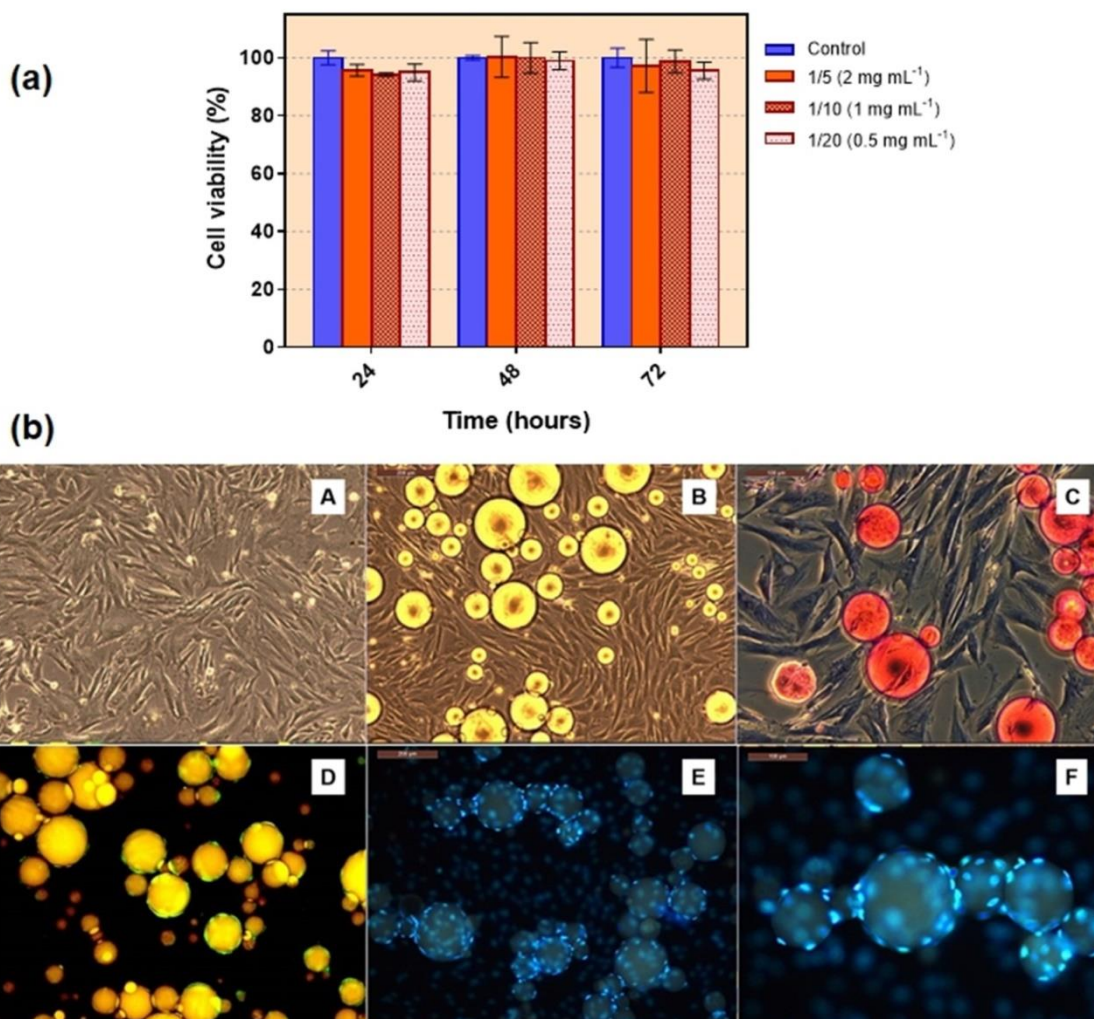


Figure 42. (a) Viability of the primary rabbit dermal fibroblasts cultured in microspheres extract, at different microspheres concentration. (b) Phase-contrast (A,B) and fluorescence micrographs (C, Giemsa; D, Calcein AM; E and F, DAPI) of the dermal fibroblasts without (A), and in the presence of poly(NIPAAm-co-APM) microspheres (B, C, D, E, F).

The captures (Figure 43b) show the microscopic images of the fibroblasts in the absence (A) and in contact with microspheres (B–F). The living cells from capture A and B (phase contrast) and D (Calcein AM) as well those fixed and stained from capture C (Giemsa staining), E and F (DAPI staining of the cell nuclei) revealed biocompatible properties of the microspheres. The direct contact of the microspheres with cells does not modify cell shape and morphology as well as their behaviour in culture media (B, C). Moreover, the rabbit dermal fibroblasts adhere in abundance to the surface of microspheres, which is highlighted in the captures E and F.

A.4. Development of micro-particulate systems applicable as mezo-porous substrata for the delivery and for the amount control of low molecular (bio)active compounds

In order to sustain the experiments on the functionality of the developed nanoplatforms, we have studied and produced two supplementary chemical entities:

- a system of particulate supports / carriers for the vehiculation and dosage of highly active low molecular compounds (for testing purposes doxorubicin, a chemotherapeutic drug used to treat several types of cancers);
- a protecting system useful to avoid genotoxic effects mediated by contaminated wastes resulted from biomedical research and usual activity (for testing purposes, the same drug, doxorubicin).

The second type of entities can be used in conjunction with the first mentioned one, for the control of the fate of the residual or excedentary amounts of nanoplatforms used in (and for now only in) *ex vivo* applications.

I. – Particulate mesoporous silica (MSi), in unfunctionalized, and in hydroxy- and aminopropyl-functionalized form

Literature reports regarding the utilization of different types of silica derivatives in the loading and release of DOX

Literature data revealed a high interest in the development of materials based on functionalized silica as support and/or carriers for the controlled release of drugs [folic acid, cisplatin, nitric oxide, dopamine, doxycycline, etc.]. Especially, mesoporous silica nanoparticles (MPSNPs) with a low level of toxicity, as compared with colloidal silica, and biocompatibility enhanced by modifying the surface, are known for their applicability in drug delivery. For such applications, the suitable size of the particles should be 50-300 nm.

The most representative types of MPSNPs are enumerated below.

- **M41S** class, with a hexagonal structure, having a porous feature, thermal stability, possessing a large surface area and a limited distribution of pore size.
- **SBA**-type MPSNPs class, similar to MCM-41 in structure, possesses excellent mechanical and thermal stability, large pore size and surface area.
- **ORMOSILs**- hybrid silica nanoparticles, with size range of 10–100 nm; their synthesis involves the use of an inorganic silica precursor (for instance, tetraethylorthosilicate [TEOS] and vinyltriethoxysilane), an organic silica precursor (e.g., diethylamine and trimethoxysilane) and a catalyst (alkaline medium). In addition, ORMOSIL nanoparticles can be surface-functionalized by attaching different targeting compounds such as carboxyl group and thiol groups for targeted drug delivery and diagnosis.

- **Hollow type-MPSNPs** used in the imaging and treatment of cancer possessing an uniform morphology, mesoporous shell, and hollow core, large surface area and high pore volume, with a high loading efficiency.
- **PMO** (periodic mesoporous organosilica), where the bridged polysilsesquioxanes are the main components of the porous framework.

Surface modification of mesoporous silica has a high impact on the interaction with cells, the uptake and accumulation of nanoparticles by the cells and tissues, etc. Different functional groups are used, like: hydroxyl, amine, carboxylate, thiol, aromatic rings, etc. The aromatic rings are responsible for the induction of surface lipophilicity, which hinders the loading of water-soluble molecules into the mesoporous system. Highest loading efficiency was exhibited by mesoporous silica containing COOH, amino and phosphoryl groups.

The stability and dispersibility of the MPSNPs can be enhanced by using biocompatible, nontoxic water-soluble polymers such as PEG. Antibodies attached on the MPSNPs surface can be targeted for cancer antigens. The results showed a twofold improvement in tumor uptake of modified MPSNPs in comparison with nonfunctionalized MPSNPs. The functionalization of MSPNPs with some molecules: vitamins, polysaccharides, proteins/peptides can improve the selective targets, which will lead to an enhanced drug delivery to the tumor cells, which involves selectivity.

Particle size should be kept <400 nm for *in vivo* applications. The diameter must be >10 nm to avoid clearance through kidney. The optimum size range of the MPSNPs for a prolonged circulation time, an improved accumulation into the tumor and an increased cellular uptake proved to be 50-300 nm.

Particle shape will affect the internalization, cell viability, adhesion, migration and distribution in the body systems. The long rod-like shaped nanoparticles exhibited a higher rate of accumulation and in the largest quantity. Doxorubicin loaded MSPNPs exhibited a higher cytotoxicity than the free DOX.

pH and the temperature: normal tissues have 7.2-7.4, inflamed tissues: 5.4-7.2, extracellular microenvironment of tumors have 6.8. Temperature ranges from 37°C (normal) to 45-50 °C in hyperthermia associated with different tumors.

Toxicity. The unique features of the MPSNPs are the external surface reactivity and the large internal surface area of pores. The reduced size of MPSNPs could be responsible for their toxicity. Generally, the toxic effect of MPSNPs is due to the oxidative stress in the cells, by production of high levels of ROS (Reactive Oxygen Species) and the suppressed levels of GSH (Glutathione, which is responsible to prevent damages of the cellular constituents caused by ROS: free radicals, peroxides, lipid peroxides, heavy metals), resulting in an apoptosis. Although silica is commonly believed as a safe material, the degradation studies on MPSNPs does not provide complete profiles of their biodegradation and biodistribution, hindering clinical advancements in MPSNPs [56].

Doxorubicin hydrochloride (DOX) represented one of the first line chemotherapeutic drugs in the treatments of various human cancers. Despite its efficacy in the treatment of carcinomas, sarcomas and hematological cancers, doxorubicin exhibits serious cumulative dose-dependent cardiotoxicity. Its therapeutical efficiency is further compromised due to the drug poor stability in biological media and low membrane permeability [57].

The scientific interest in studying the effects of this drug in different formulations and compositions is highlighting by a remarkable number of publications in which *doxorubicin* is a keyword (about 60000 ISI articles), *doxorubicin carriers* (about 5000 ISI articles) and doxorubicin formulations (about 3000 ISI articles) (Figure 43a) (ISI Web of Knowledge, November 2019). Fewer reports were recorded on Doxorubicin silica, Doxorubicin mesoporous silica or Doxorubicin functionalized mesoporous silica. For the last keyword, there are only 248 publications, from which only 41 reports in 2019 (Figure 43b), so that our interest in this area is motivated.

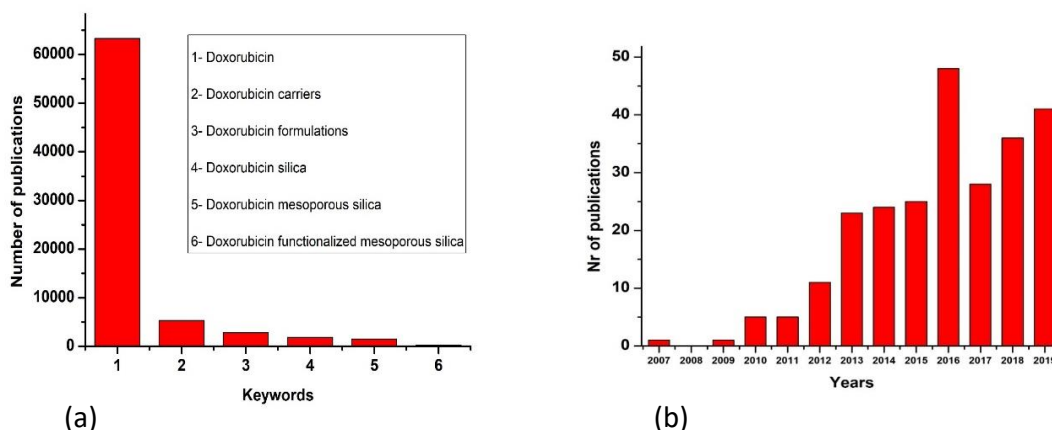


Figure 43. Number of publications with doxorubicin as keyword (a), and number of publications having doxorubicin functionalized mesoporous silica as subject (b).

Performed experiments

Materials and Methods: Doxorubicin (Figure 44) hydrochloride 2mg/ml (commercially available), and mesoporous silica particles with various functionalities (MSil1, MSil1bis, MSil4, MSil4bis and D1) were used (see Table 4). Mesoporous silica materials with MCM-41 type of structure containing a homogeneous layer of organic functional groups inside the pores were prepared using a co-condensation method in presence of a surfactant in low concentration according to reference [58].

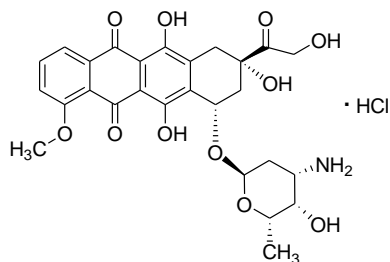


Figure 44. The chemical structure of doxorubicin hydrochloride.

Loading of DOX into selected silica

Loading experiments occurred at room temperature, at pH 5.5 and 7.4, in some cases by using ultrasonication. For loading of DOX, 10-60 mg of each silica type were dispersed in an aqueous solution 0.1wt% or 0.2 wt% DOX. In the first experiments, for the encapsulation of DOX, Millipore water (pH 5.5) was used to prepare a solution 0.1wt% of DOX.

(a) First approach

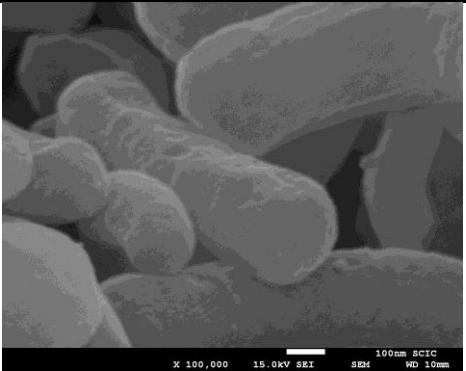
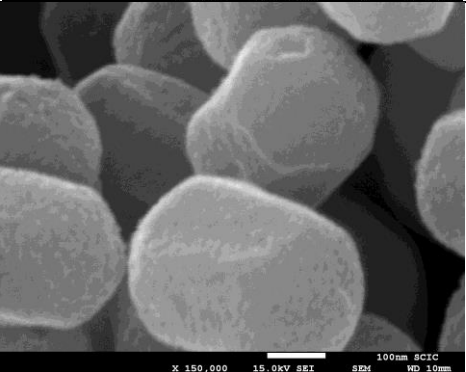
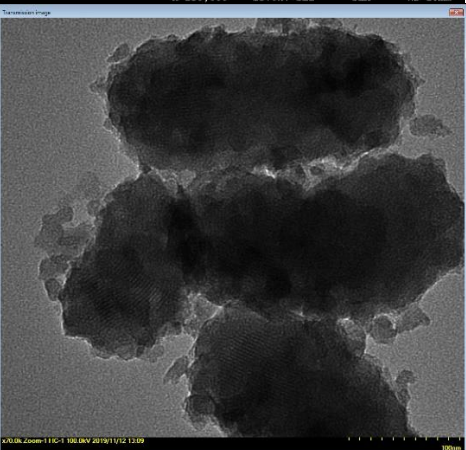
About 60 mg of each sample (MSil1, MSil1bis, MSil4, MSil4bis) was dispersed in the DOX solution 0.1% (20 mL). A rotatory shaker (25 °C, 150 rpm) was used during the loading process in dark space. The mixture was maintained in these conditions for 48 h. The drug-loading capacity was calculated by measuring the remained DOX concentration in the residual solution by UV-vis spectroscopy, by using the DOX absorbance at 482 nm.

Sample aliquots were collected after 24h and 48h and the absorbance of DOX was determined by UV-vis spectrophotometer at λ_{max} of 482 nm. The calibration curves of DOX at pH 5 and 7.4 were also plotted in order to calculate the drug-loading and release. The encapsulation of DOX occurred only in MSil1 bis, UV-vis spectra confirming this by changes in the absorbance at 482 nm (Figure 45).

The DOX solutions of MSil1, MSil4 and MSil4bis were incubated at 40 °C under magnetic stirring in order to increase the diffusion of DOX in silica pores. After 1 week, the UV absorption maximum of DOX aliquots was unchanged. After separation of silica from DOX

solution the color was slight pink, suggesting only a weak binding of DOX in the case of MSil1, MSil4 and MSil4bis, while in the case of MSil1bis the color was red (Figure 46).

Table 4. Characteristics of the functionalized silica.

Sample	Organic / functional group	BET area (m ² /g)	Morphology
MSil1	11 mol% 3-aminopropyl -CH ₂ -CH ₂ -CH ₂ -NH ₂	722	
MSil 1bis		621	
M Sil 4	27.2 mol% 3-aminopropyl -OH	1001	
M Sil 4 bis		936	
MDil_D1	27.2 mol% methyl -CH ₃	943	

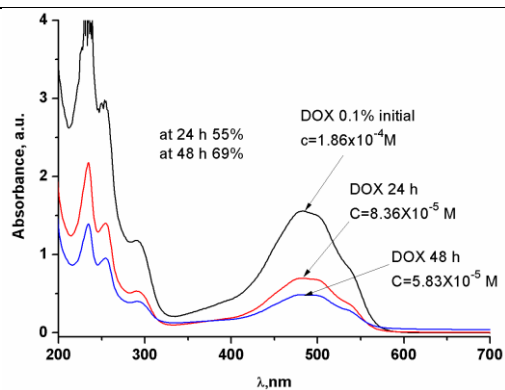


Figure 45. UV-vis spectra of DOX solution during loading of MSil1bis at pH 5.5.

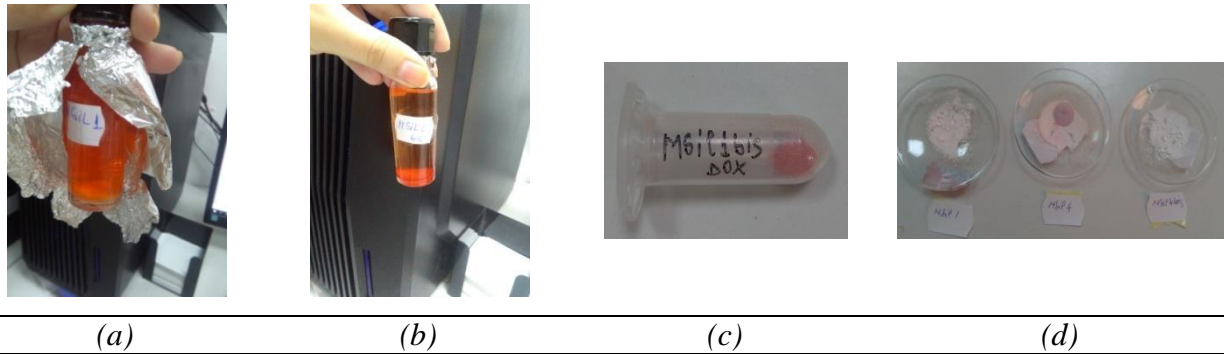


Figure 46. The color changes during the loading of DOX: (a) MSil 1 in DOX solution; (b) MSil 1bis in DOX solution and after filtration, (c, d) MSil1, MSil 4 and MSil 4bis after DOX loading.

The encapsulation efficiency (EE) and loading capacity (LC) were calculated using the following formulas:

$$EE (\%) = \frac{W(\text{drug in silica})}{W(\text{initial added drug})} \times 100$$

$$LC (\%) = \frac{W(\text{drug in silica})}{W(\text{silica})} \times 100$$

For MSil 1bis EE calculated value was 68.72 %, and LC value was 115 %.

(b) Second approach

In the second set of experiments, the loading was carried out in phosphate buffer solution of pH 7. For each 10 mg of silica (MSil 1, MSil 1 bis, MSil 4, MSil 4 bis and D1), about 2 ml of DOX 0.2% solution was used. In all samples the encapsulation took place, almost immediately in D1 (Figure 47) and after stirring on a shaker on 150 r. p. m. for 24 h in the others. The UV-vis measurements of the supernatant solution of DOX also indicated the successful loading in all silica (Table 5).

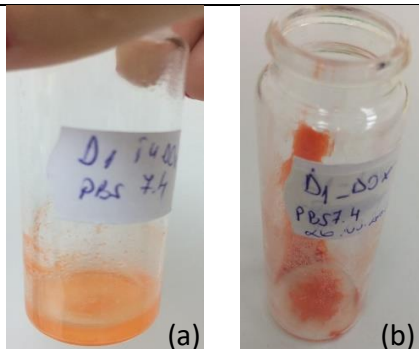


Figure 47. D1 during (a) and after (b) loading of DOX.

Table 5. Loading of DOX in terms of EE and LC in the silica

Samples	Encapsulation Efficiency (EE), %	Loading capacity (LC), %
Msil 1 bis	69.00	115.0
Msil 4	63.86	18.35
Msil 4 bis	55.89	16.05
D1	127.00	606.5

Characterization of the silica-DOX composites

FTIR spectroscopy was used to investigate the chemical modification of silica loaded with DOX. In order to evidence successful loading of DOX in MSil1bis, IR spectra of MSil1bis-DOX and DOX were subtracted and the resulting spectrum can be seen in Figure 6. The IR subtracted spectrum is compared with the IR spectrum of DOX. It can be observed that in positive range the characteristic IR vibrations of the silica are present: 1092 and 471 cm^{-1} assigned to the asymmetric stretching vibration and rocking modes of the Si-O-Si units, while in negative range all vibrations assigned to DOX can be observed. The broad vibrations at 3474 cm^{-1} and 3239 cm^{-1} in the subtracted IR spectrum are assigned to OH and NH_2 groups from silica and DOX, suggesting H-bonding interactions between them. These bands are blueshifted by 52 and 92 cm^{-1} in the IR spectrum of MSil1bis-DOX. On the other hand, the characteristic vibrations at 968 cm^{-1} and 795 cm^{-1} (Figure 48) assigned to the established mesoporous silica network are diminished after loading DOX in silica, indicating the alteration of the mesoporous framework. Based on IR spectra we can conclude that DOX was both encapsulated and surface bonded.

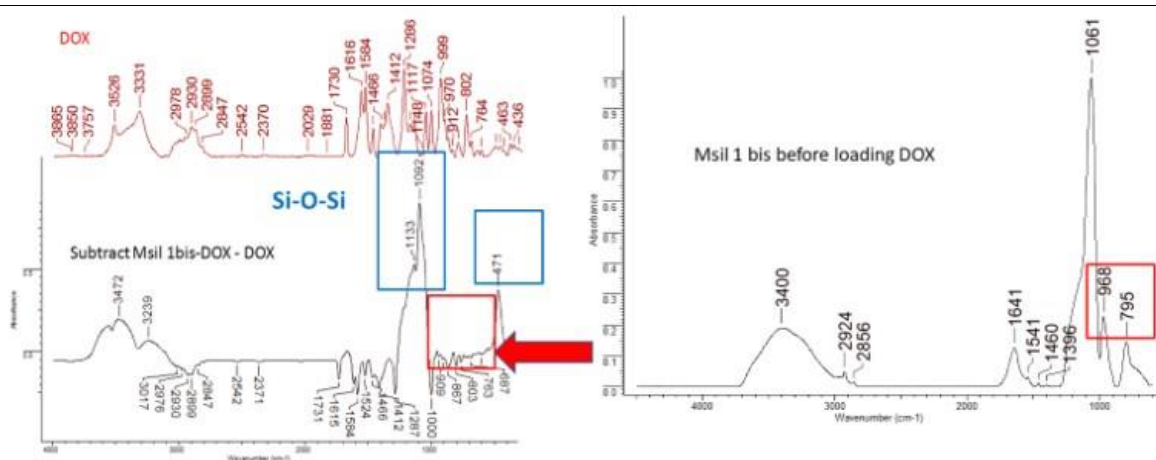


Figure 48. Subtracted FT-IR spectra between MSil1bis-DOX and DOX.

DLS and Zeta potential. In order to establish the changes occurred in silica after loading DOX, DLS and zeta potential analysis were performed. Thus, MSil1bis-DOX formed aggregates 533 nm (PDI=0.712) at a concentration of 0.01%, which are above the allowed therapeutic values (Figure 49).

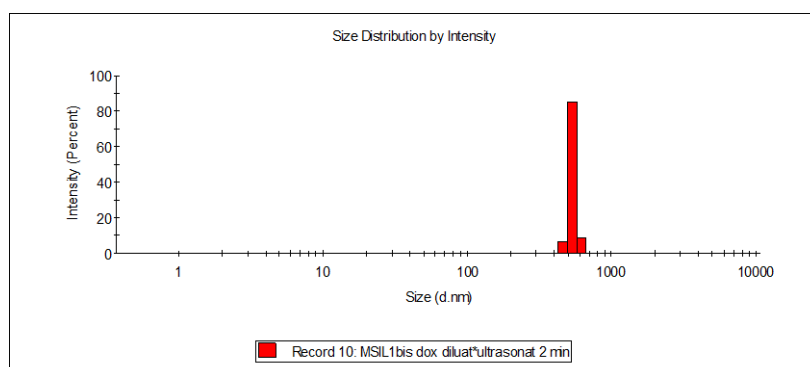


Figure 49. DLS results of the MSil1bis-DOX.

Zeta potential value of MSil1bis-DOX differs from the MSil1bis suggesting different surface chemistry. The value of -26 mV for MSil1bis-DOX is attributed to presence of hydroxyl groups on their surface, Zeta potential for MSil1bis being +38 mV (Figure 50). Meanwhile, the zeta potential values indicate stable particles in solution.

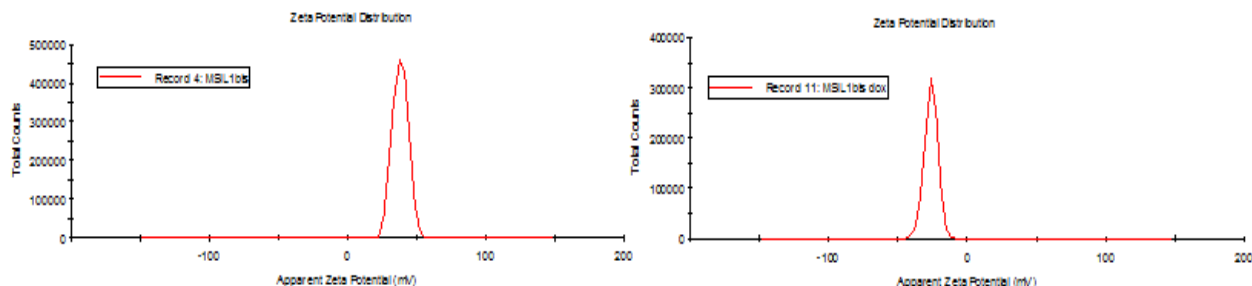


Figure 50. Zeta potential results of MSil1bis (a) and MSil1bis-DOX (b).

SEM morphology of the silica before and after loading of DOX were recorded (Figure 51). One can observe the formation of uniform, spherical aggregates after DOX loading in silica.

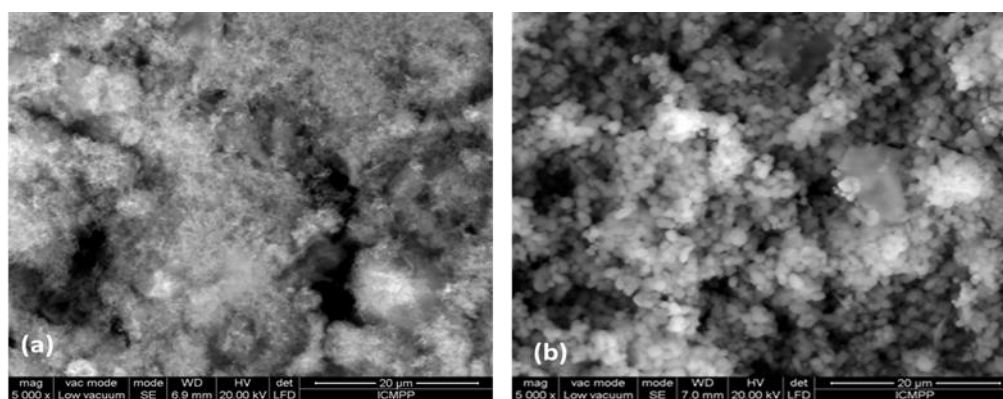


Figure 51. Zeta potential results of MSil1bis (a) and MSil1bis-DOX (b).

Release of DOX from mesoporous silica

Was investigated at 37 and 45 °C and different pH values (7.4, 5 and 1.5).

(a) Release at pH 7.4 and 5

MSil1bis loaded with DOX at pH 5 was first evaluated for the release of DOX at pH 7.4 and 5 (Figure 10). The release curves of MSil1bis-DOX revealed a higher delivery of DOX at pH 5. The DOX concentration released faster increases in the first 6 h, mainly due to the delivery of DOX from the surface of silica. In the next hours and days the release is slower but a constant concentration is maintained (Figure 52a). The cumulative release at pH 5 is 9.26% higher than at pH 7.4 (Figure 52b).

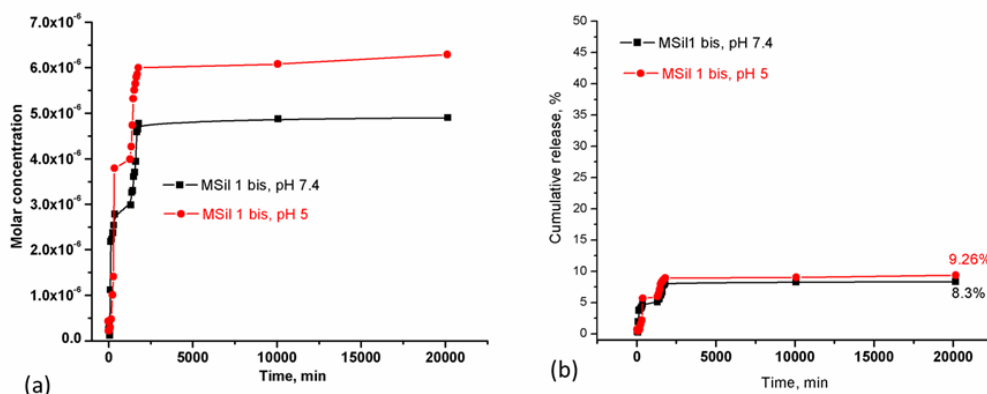


Figure 52. The release curves of MSil1bis-DOX at pH 5 and 7.4.

Table 6 presents the comparative released concentrations at pH 5 and 7.4. One can observe a complementary behavior at the two pH values: the DOX concentration released at pH 5 after 24 h is the same with those released at pH 7.4 after 2 weeks, while the concentration released at pH 7.4 after 24 h is doubled at pH 5 after 2 weeks. In the same time, the concentration released was tested on cancer cell line (HOS) and the results indicated in all cases that a concentration of DOX between 1-10 $\mu\text{g}/\text{mL}$ reduced the viability of HOS cell to 40% (Figure 52). It should be mentioned that DOX has no selectivity on tumor cells, which means that the released concentration of DOX has the same impact on the normal cells, reducing their viability to 40%.

Table 6. Comparative data of the released DOX from MSil1bis-DOX composite.

Sample	pH			
	5		7.4	
	Cumulative release	Concentration released	Cumulative release	Concentration released
MSil1 bis	6.96 % (24h)	5.08 $\mu\text{g}/\text{mL}$	5.59 % (24h)	3.54 $\mu\text{g}/\text{mL}$
	9.26 % (after 2 weeks)	6.75 $\mu\text{g}/\text{mL}$	8.3 % (after 2 weeks)	5.27 $\mu\text{g}/\text{mL}$

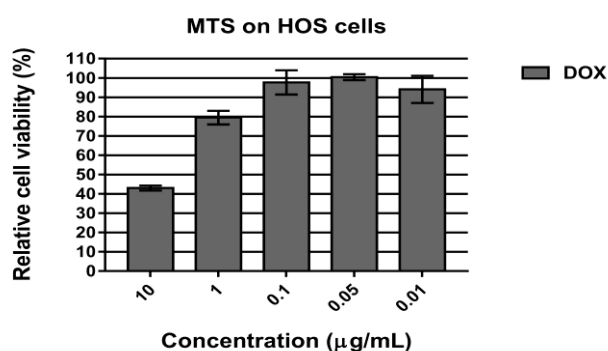


Figure 53. Viability of HOS cells at different concentrations of DOX.

(a) Release at pH 1.5

Taking into account that EE and LC of MSil 4 and MSil4 bis were lower than those of MSil1 bis and D1, the release behavior was studied at pH 1.5 for 24 h (Figure 54). One can observe a lower cumulative release, only of 2% as compared with MSil1bis, which corresponds to 0.65 $\mu\text{g}/\text{mL}$ DOX after 1 h for MSil4 and 0.73 $\mu\text{g}/\text{mL}$ DOX after 1 h for MSil4bis. These concentrations remain relative constant during 24 h, but the accumulated DOX has no a therapeutic effect on the tumor cell, as observed in Figure 53, where at a concentration of 0.1 $\mu\text{g}/\text{mL}$ DOX the HOS viability is 97%.

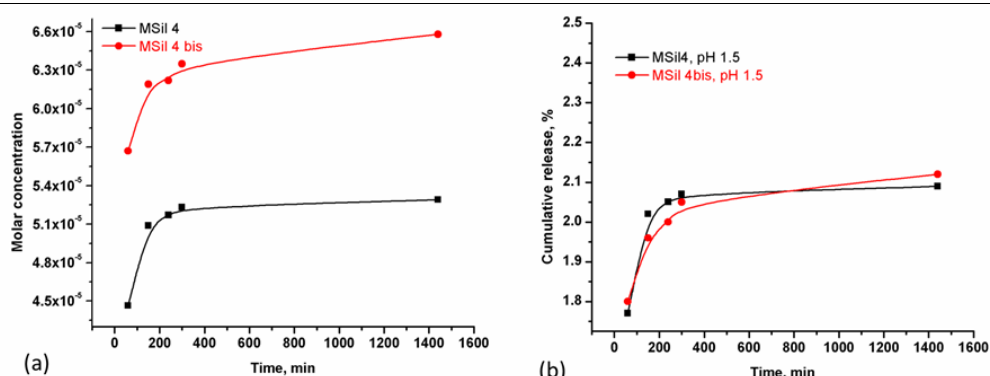


Figure 54. The release curves of MSil 4 and MSil4bis-DOX at pH 1.5.

We also studied the release behavior of D1, with the highest EE and LC of DOX. In the case of D1, a different behavior was observed. In the first 5 h a highest concentration of DOX was released in pH 7.4, after which the released concentration remained constant during 1 week (Figure 55a). At pH 5 an increased concentration of DOX was observed during 1 week, the cumulative release being 9.24 % (Figure 55b). The released concentrations are lower than MSil1bis at pH 5 (see Table 7), suggesting that a pH decreasing does not enhanced the release of DOX. The released concentrations from D1 are also considered as therapeutic, with a lower impact on the HOS cells viability as compared with MSil1bis or with the same composite at pH 7.4. Moreover, the released concentration at pH 7.4 after 24h is even higher than the concentration released after 1 week at pH 1.5, suggesting an effective lack of selectivity on tumor cells in comparison with healthy ones.

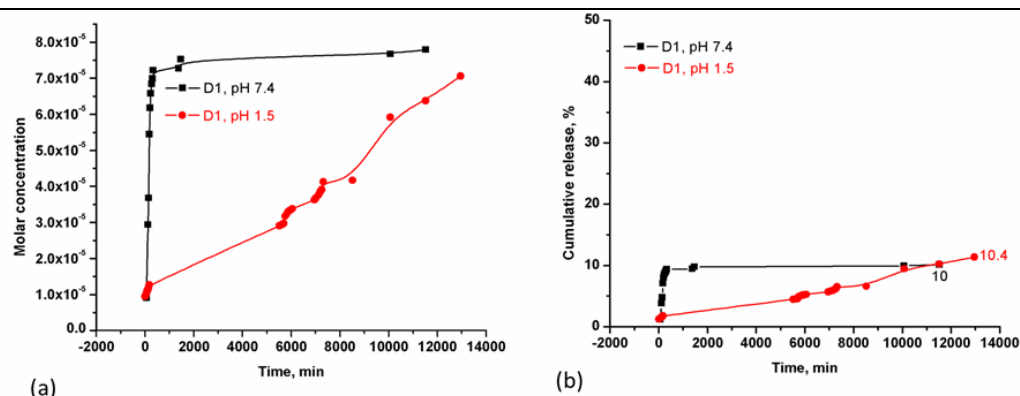


Figure 55. The release curves of D1-DOX at pH 7.4 and 1.5.

Table 7. Comparative data of the released DOX from D1-DOX composite.

Sample	pH			
	5		7.4	
	Cumulative release	Concentration released	Cumulative release	Concentration released
D1	3.38 % (24h)	1.6 µg/mL	9.44 % (24h)	5.6 µg/mL
	9.24 % (after 1 week)	4.77 µg/mL	10 % (after 1 week)	6.05 µg/mL

Comparing the cumulative release from MSil1bis-DOX and D1-DOX, one can observe a higher released at pH 7.4 after 24h for D1. At acid pH, MSil1bis has a faster release after 24h. But, after 1 week both composites have the same impact in acid medium, the cumulative release having the same value (Figure 56). Moreover, a small selectivity at pH 5 was observed for MSil1bis, suggesting a higher impact on the cancer cells than to the normal ones.

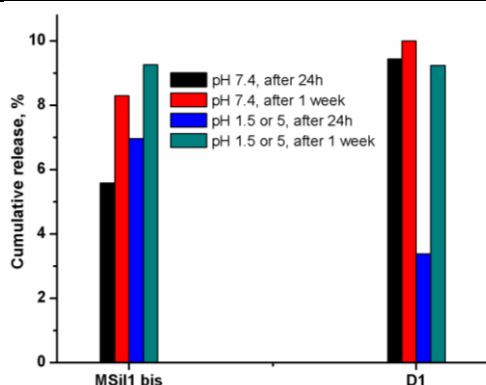


Figure 56. Comparative release data for MSil1 bis and D1 composites.

Table 8 resumes the DOX loading and releasing abilities of the silica derivatives, as reported in literature. Data can be compared with the values we obtained.

Table 8. Comparative data regarding the loading and the release of DOX from different silica derivatives.

Silica-based materials	Loading capacity		Cumulative released			Reference
	pH	%	pH	T, °C	%	
Mesoporous nanosilica templates having a diameter close to 30 nm which drive the protein (Human Serum Albumin) nanocapsule formation.	-	30 88 (nanocapsules with protein)	-	-	-	[59]
Gold nanostars coated with a mesoporous silica shell (AuNSt@mSiO ₂) using a PEG incorporated of photocleavage 2-nitrobenzyl linker as capping ensemble.	-	100	-	-	80	[60]
Graphene quantum dots capped in hollow mesoporous silica nanoparticles, GQDs@hMSN.	-	80	5 6.5 7.4	37	58 28 14	[61]
Folate-conjugated, mesoporous silica functionalized boron nitride nanospheres.	-	52.6	5 7.4	-	80 20	[62]
Multifunctional drug delivery system based on mesoporous silica nanoparticles, hyaluronic acid, polyethylene imine and DOX, HAPEI-MSNP_Dox.	-	-	7.4 4.5 6 6+Hyaluronic 4.5+Hyaluronic	-	2 3 5 50 65	[63]
Mesoporous silica nanoparticles (MSNs) loaded with doxorubicin modified with poly(lactic-co-glycolic acid) (PLGA) and conjugated with Angiopep-2 (ANG).	-	38-90	7.4 6.4	-	20 40	[64]
A complex DDS (drug delivery systems) named DOX@MSN-ZnO-PLL-PLL(DMA) (Polylysine and dodecyl methacrylate).	7.4	53.4	5 6.5 7.4	-	91 21 20	[65]
Large-pore coralline mesoporous silica microparticles (CMS)	-	26.7	5 7.4	-	32 8.5	[66]

synthesized by using the triblock polymer PEG-b-PEO-b-PEG						
Monodispersed, doxorubicin (Dox) loaded chitosan (Cts) nanospheres functionalized by mesoporous SiO ₂ and folic acid (FA).	-	82.4	5 7.4	-	82 4	[67]
Magnetic mesoporous silica nanoparticles functionalized by pH-sensitive caps.	-	-	7.4 5	-	34 83	[68]
HApt aptamer-functionalized pH-sensitive β -cyclodextrin (β -CD)-capped doxorubicin (DOX)-loaded mesoporous silica nanoparticles (termed MSN-BM/CD-HApt@DOX).	7.4	3.6	7.4 6.4 4.5	-	19 18.8 82	[69]
Mesoporous silica nanoparticles capped with cerium oxide nanoparticles (COP@MSN).	7.4	120	4 5 6 7	-	65 50 20 3	[70]
Mesoporous silica nanoparticles (MSN) that contain on their surface various types of DNA molecules.	-	-	5	-	3-80	[71]
Hollow mesoporous zirconia nanocapsules (hm-ZrO ₂) with a hollow core / porous shell structure.	-	102	3.6 5.2 6.6 7.4	-	35 20 10 4.5	[72]
Mesoporous silica nanoparticles (MSNs) covalently integrating a nitric oxide (NO) photodonor (NOPD) and a singlet oxygen (¹ O ₂) photosensitizer (PS) and encapsulating the anticancer doxorubicin (DOX).	7.4	85	7.4	-	10	[73]
Porous nanosilica (PNS) conjugated with gelatin-poly (ethylene glycol)methyl ether (GEL-mPEG) to form PNS-GELmPEGnanocarriers for doxorubicin (DOX) delivery.	-	86	4.5 7.4	-	20 70	[74]
Light/redox dual-stimuli responsive β -cyclodextrin (β -CD)-gated mesoporous silica nanoparticles (MSN).	7.4	63	-	-	17	[75]

Inorganic/organic hybrid composites based on mesoporous silica nanotubes (MSNTs) and pH-responsive polyelectrolytes	7.4	82-89	8 7.4 6.8 5.2 4 1.2	-	10 20 30 80 83 90	[76]
Novel dual-sensitive (enzyme- and redox-) MSN (mesoporous silica nanoparticles) based on functionalized dopamine containing both peptide and disulfide bonds	-	23-MSN 67-LMSN	7.4 5 7.4 5	-	80 80 14 67	[77]
Mesoporous silica nanoparticle-supported lipid bilayers (LMSNs) developed with doxorubicin (DOX)	7.4	17-90	3.5 7.4	-	65 45	[78]

Conclusions and perspectives

Based on the literature data, one can say that a conjugation of mesoporous silica with different proteins, lipids or other liposomal and polyelectrolyte derivatives has a positive impact especially on the release of DOX. The cumulative release could increase up to 90% in some cases. From this point of view, it is clear that in simple drug delivery systems based on functionalized silica the problem of release exists, and over time different strategies have been developed to overcome such disadvantage of a lower cumulative release. Our results are similar with those reported in literature for some complex delivery systems.

Our perspectives will be directed to optimization of the release conditions, taking into account the cumulative influence of different factors: dialysis membrane, Ph, temperature, ultrasonication, porosity, release time, etc. A major problem will be to reduce the size of the silica loaded with DOX in the range 10-300 nm. Also, it is necessary to study the stability of our silica-DOX composites, knowing that the stability of DOX in solution or in liposomal formulations is 24h in glucose solution 5% or 48h in saline solution 0.9%.

The advantage of our composites is the possibility of an extended release of DOX, taking into account that the half time of DOX is about 72h, which means that it reduces the number of doses administered at certain time intervals. In order to confirm the applicability of the dosing system we developed, we will study the cytotoxicity of our composites on normal and cancer cells, not only the released DOX concentrations.

II. – Metal-organic frameworks (MOFs) for the destruction of residual doxorubicin

MOF-type metal complexes (Zn (II), Cu (II), and Co (II)) with a dicarboxylic acid having a siloxane spacer, applicable for rapidly decomposing of doxorubicin, in heterogeneous system, in the presence of light

Such a process is useful in purifying health care wastes contaminated with chemotherapy drugs which are highly hazardous because of potential genotoxic effects. Doxorubicin interacts with DNA by intercalation and inhibition of macromolecular biosynthesis, thus acting unselectively on all growing cells. Therefore DOX is constantly under study to find less harmful formulations with more effective targeted delivery, as for example liposome-encapsulation, PEG-peptide conjugates, functionalized DNA nanocages or incorporation into metal-organic frameworks (MOFs). The stability of the drug in different conditions is very important from pharmaceutical perspective. DOX degradation has been studied under hydrolytic conditions at

various pH and temperature, or under photolytic and oxidative (H_2O_2) conditions, and it was shown that it is highly sensitive to alkaline pH, sensitive to acidic pH at high temperature, and also to oxidation. On the other hand, health care wastes contaminated with chemotherapy drugs and their metabolites are highly hazardous because of potential genotoxic effects, as mutagenic, teratogenic and/or carcinogenic, and may affect aquatic organisms. Several studies demonstrated that residual amounts of cytotoxic solutions represented a real occupational risk and these “should not be discarded in the domestic sewage system without prior inactivation”. In the context of environmental concerns, this motivated us to investigate the possible decontamination of waste waters, aiming to remove DOX. The destruction of wastes, un-transformed drug or its metabolites received very little attention, although it was demonstrated that the (photo)decomposition products preserve the anthracycline structure, so they can be chemical carcinogens, mutagens and exert toxic effects on humans. To our knowledge, none of the reported studies showed complete mineralization of DOX, nor proved degradation of the anthracycline structure.

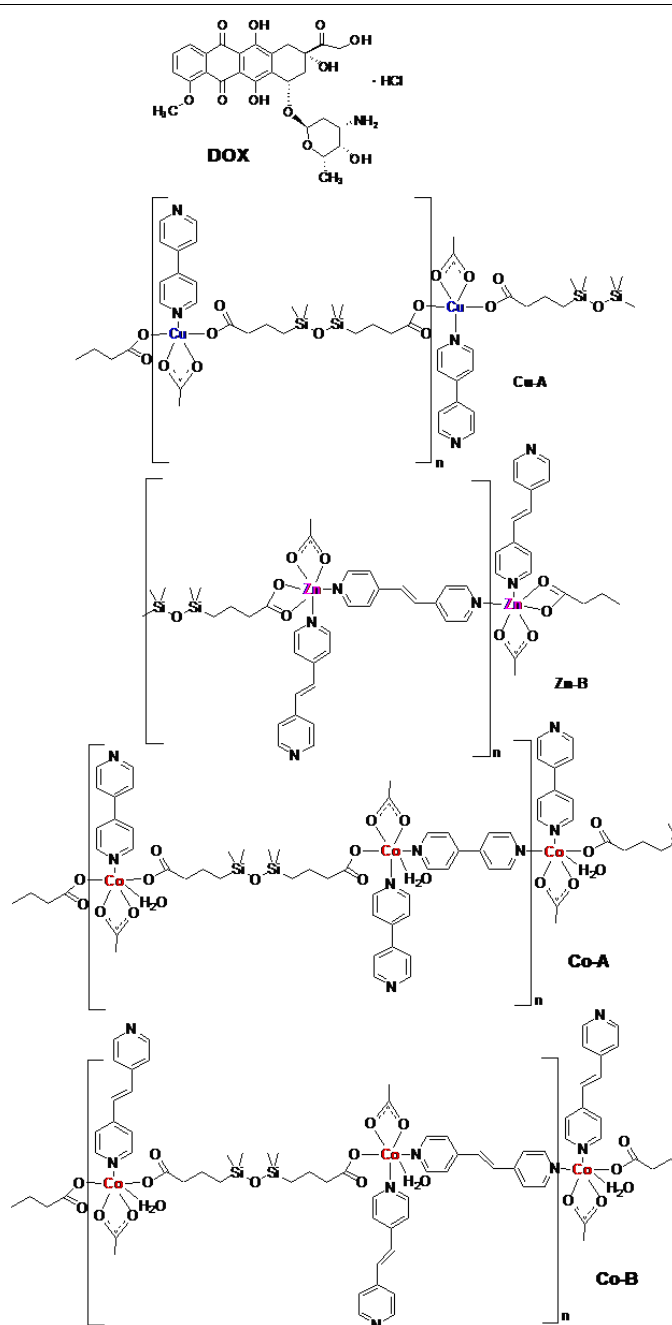


Figure 57. Structure of the metal complexes used as catalysts.

We investigated the kinetics and residual products of the photocatalytic decomposition of doxorubicin at normal pH, at ambient light and temperature, in presence of H₂O₂ and zinc(II), copper(II) and cobalt(II) MOFs based on a disiloxane carboxylic acid and bipyridine (Figure 57). We proved the destruction of the anthracycline structure of DOX and identified glycerol as the main reaction product. The siloxane-based hydrophobic MOFs are acting as heterogeneous catalysts, being stable in the reaction conditions, contrary to a model MOF without siloxane fragment.

The kinetics of the photodegradation process was followed by UV-Vis spectroscopy and by ESI-MS. According to UV-Vis data, two pseudo-first order kinetic steps describe the process, with rate constants in the order of 10⁻³-10⁻² min⁻¹ for the rate determining one. ESI-MS provided more accurate information, with a rate constant of 2.6·10⁻² min⁻¹ calculated from the variation of DOX ion abundance (Figure 58). Complete decomposition of DOX was achieved after 120 min in the shade and after only 20 min by exposure to sunlight (Figure 59). The analysis of the residual waters by mass spectrometry and 1D and 2D NMR spectroscopy showed complete disappearance of DOX in all cases, excluded any anthracycline species, which are destroyed in the tested conditions, and proved formation of an un-harmful compound – glycerol, while no trace of metal was detected by XRF.

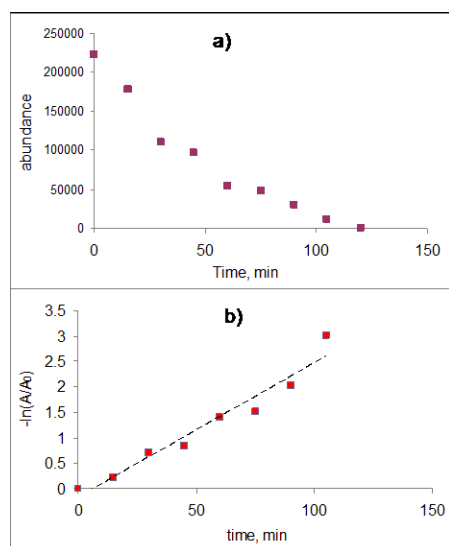


Figure 58. The decrease of doxorubicin parent ion abundance (a), and the first-order kinetic law applied to this trend (b).

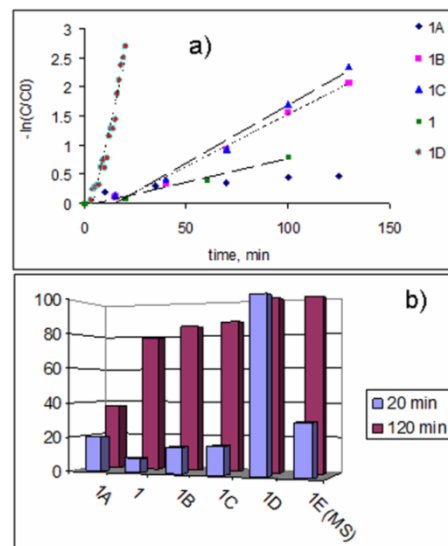


Figure 59. DOX photodecomposition with catalyst Cu-A in different conditions: pseudo-first order kinetics plots (a), and the efficiency of DOX photodecomposition (b).

By this study we brought into attention a less addressed pollution issue, and we proposed a mild and effective method for removal of DOX drug emerging pollutants.

III. – Various compounds and formulations of nanoconjugate type, implied in functional supramolecular aggregation

Formulations of diminazene aceturate designed to improve its bioavailability and to maximize the therapeutic index in animals by overcoming the rapid degradation under acidic pH of the stomach

In our day, the introduction of more concepts in supramolecular chemistry, which permits the studies of self-assembly of molecules (including polymers), has attracted more and more

scientists, becoming a popular area for experimental chemistry, creating a new way for the future not only for the chemists, but for the other researchers (biochemists, engineers, physicists, theoreticians, etc). Supramolecular chemistry is exploiting physical bonds (like hydrogen bonds, π - π stackings or coordination complexation), which are responsible in fabricating new supramolecular materials [79]. It should be mentioned that an important factor of supramolecular materials is the reversibility of the formed systems and in this respect, inclusion complexation based on cyclodextrins play a remarkable role.

In our study β -Cyclodextrin (β -CD) was used as a functional excipient used for enhancing the diminazene aceturate (DA) bioavailability (Figure 60) [80]. Most studies show that DA has both antioxidant and antimicrobial activity more or less pronounced according to the administrated dose. In the same time, an important problem that must be overcome is to prevent the administration of high dose that may be lethal [81]. As its chemical stability in aqueous solutions, DA is stable few days at neutral pH, while in acidic pH, the molecule could be transformed, in few minutes, in 4-amino-benzamidine and 4-amino-phenyl-diazonium salt. Besides this, it is strongly recommended to protect DA against direct light due to its photo-instability [82].

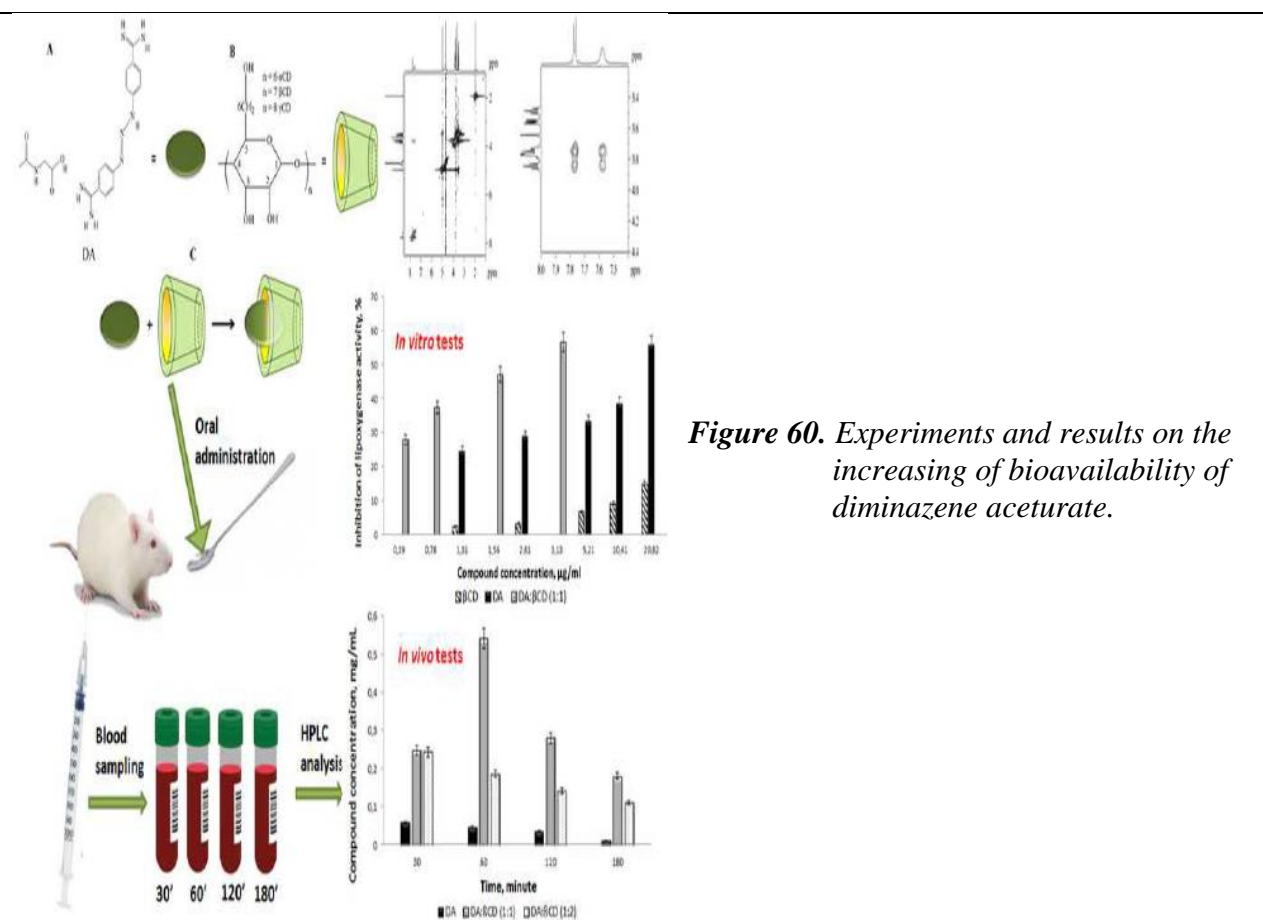


Figure 60. Experiments and results on the increasing of bioavailability of diminazene aceturate.

The formation of 1:1 molar ratio inclusion complex between DA and β CD with association constant of 608.7 M^{-1} was demonstrated by different techniques (Raman, DSC, WAXD, ^1H -RMN, ROESY), and its stoichiometry was determined from Job's plot data. IC50 value of DA: β CD (1:1) inclusion complex against lipoygenase was $1.93 \pm 0.05 \text{ } \mu\text{g/ml}$ while of parent DA was $16.53 \pm 0.24 \text{ } \mu\text{g/ml}$. *In vivo* tests have shown that the bioavailability of DA has been increased due to its protection against degradation in acidic pH of stomach through its encapsulation into β CD's cavity at amounts closed to the administrated dose. In contrast, when parent DA was administrated, the determined bioavailability was very low, meaning that high amount of DA was degraded by low pH of the stomach. Overall, the obtained data suggest that

the administration of DA, as its inclusion complex with β CD, considerably reduces the necessary administration dose, making it possible to use this formulation in the treatment of diseases that required up to now high doses of parent DA, thus eliminating the risk of lethal doses administration.

Magnetic-cerium oxide nanoconjugates with antioxidant activity [83]

The importance of magnetic nanoparticles in nanomedicine results in the possibility of their application both in targeted therapy and in diagnosis, suggesting a theranostic approach of the biomedical applications. Nanoceria has mimetic activity of superoxide dismutase, being able to inactivate the excess of reactive oxygen species correlated with a large number of pathologies, such as stents restenosis and the occurrence of genetic mutations that can cause cancer. This study presents the synthesis and biological characterisation of nanoconjugates based of nanoparticles of iron oxide interconnected with nanoceria.

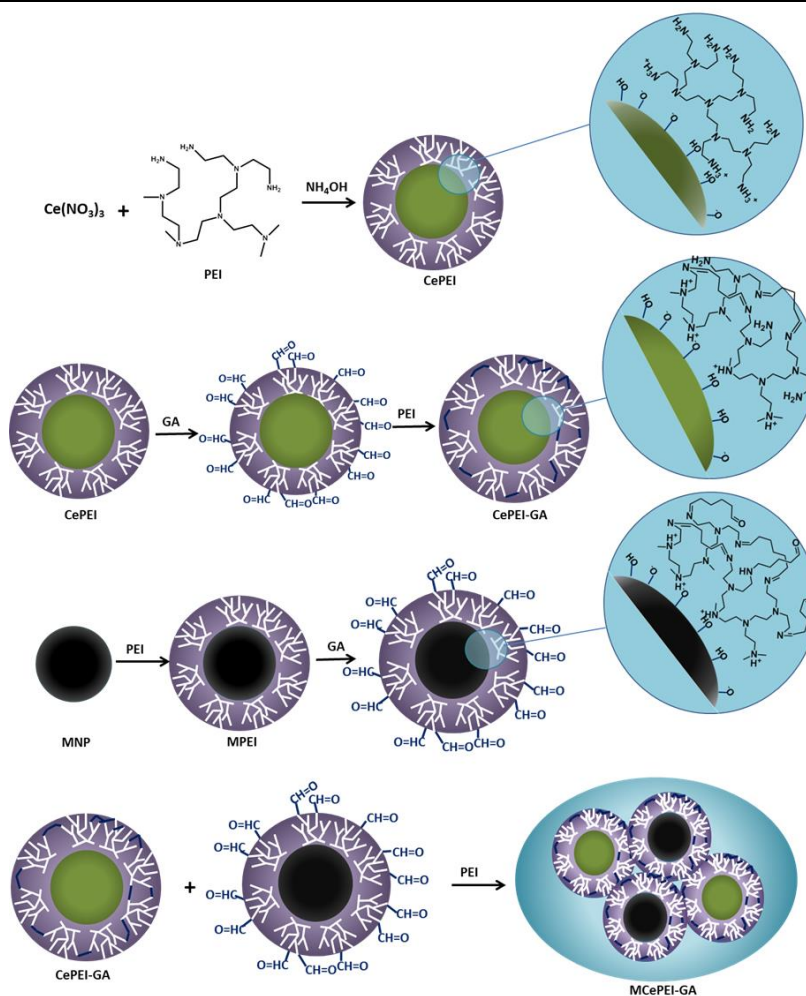


Figure 61. Schematic representation of magnetite-nanoceria nanoconjugates synthesis.

The synthesis of magnetite-nanoceria nanoconjugates has been done in several stages (Figure 61), where the key of the process is the coating of nanoparticles with polyethyleneimine and its chemical activation-reticulation with glutaraldehyde. Nanoparticles have been structurally and morphologically characterized by techniques such as FTIR, Raman, XPS, EDX and TEM. The physico-chemical characterization was done by DLS and magnetization measurements. Antioxidant activity was evaluated *in vitro* by the DPPH assay and *in vivo*, measuring total antioxidant capacity in mice. There were obtained magnetite nanoparticles interconnected with nanoceria having an average diameter of 8 nm. DLS study of aqueous dispersions of

nanoconjugates showed that they are stable and had a high positive zeta potential of about +30 mV, which is a measure of covering degree with polyethylenimine. Nanoparticles have superparamagnetic properties and the saturation magnetization varies with the addition of diamagnetic component in the system, remaining within the limits of biomedical applications. The interconnected nanoparticles have *in vitro* free-radical scavenging properties that have been shown to be improved as a result of the increased amount of the Ce³⁺ ions and crosslinking of polyethylenimine on the surface of nanoparticles. Measurement of total antioxidant activity *in vivo* revealed increased antioxidant activity in all organs and fluids collected from mice.

In conclusion, nanoconjugates based on iron-oxide and cerium oxide nanoparticles have magnetic properties with potential biomedical application such as magnetically guided drug delivery agents and contrast agents in MRI. In addition to the useful magnetic properties, they have antioxidant activity, being able to scavenge free-radicals and reducing the oxidative stress, ability demonstrated both by *in vivo* and *in vitro* experiments. The combination of the two properties mentioned above make them excellent candidates for theranostic applications.

A.5. Evaluation of the functionality of the extracellular matrix / tumors surrogates in *ex vivo* systems of cells culturing.

Two types of tissue / tumor surrogates were prepared and preliminary tested during the 2019 stage. Table 9 summarizes their characteristics.

Table 9. Coding and physical-chemical characteristics of the investigated surrogate samples.

No.	Scaffold code	Pore size (µm)	Swelling capacity in PBS	Cchemical composition of the hydrogel samples
I	HA ² G50	8 ÷ 35	41.57 %	Hydrogel made of 2% w/v hyaluronic acid (HA) and poly(methyl vinyl ether - <i>alt</i> - maleic acid) (G) 50 %
II	HA ³ G50	18 ÷ 41	40.04 %	Hydrogel made of 3% w/v hyaluronic acid (HA) and poly(methyl vinyl ether - <i>alt</i> - maleic acid) (G) 50 %

I. – Investigation of the HA²G50 as tumor surrogates populated with human tumor cells

In order to characterize the scaffolds / sponge-type hydrogels based on hyaluronic acid (HA) and poly(methyl vinyl ether-*alt*-maleic acid) (G) (HA²G50) in terms of biological properties, they were populated with two human cell lines: lung carcinoma (A549 cells) and liver carcinoma (HepG2 cells). Scaffolds were populated with HepG2 at different cellular densities (4.5x10⁴, 7.5x10⁴ and 2.5x10⁵ cells) and the cytotoxicity induced by HA²G50 was monitored over time (1 day, 7 days, 14 days after seeding). On the other hand, HA²G50 seeded with HepG2 or A549 were processed for investigation by optical and fluorescence microscopy to reveal the actin cytoskeleton (eosin staining, respectively fluorescein-conjugated phalloidin - phalloidin-FITC) and the cells nuclei (hematoxylin, respectively 4', 6-diamidino-2-phenylindole, DAPI). Thus, the effect of HA²G50 matrix on embedded cell morphology was highlighted.

1. Materials and methods

1.1. Cells

Hep G2 cells (human hepatocarcinoma cell line) and **A549 cells** (human lung carcinoma epithelial cell line) were cultured in Dulbecco's modified Eagle's medium (DMEM) supplemented with fetal calf serum (10%), penicillin (100 U / ml), streptomycin (100 µg / ml), neomycin (50 µg / ml) at 37°C in a 5% CO₂ incubator.

1.2. *In vitro* determination of HA²G50-induced cytotoxicity

To determine the cytotoxicity induced by HA²G50 on HepG2, we used the XTT colorimetric assay based on formazan. The reagent 2,3-bis- (2-methoxy-4-nitro-5-sulfophenyl) - 2H-tetrazolium-5-carboxanilide (XTT) is taken up and transformed by the metabolically active cells into orange formazan in the presence of the reduction agent, methosulfate phenazine (PMS). The intensity of the orange color of the formazan resulted in the culture medium is quantified by measuring the absorbance at 450 nm using the infinite Tecan plate reader M 200. From the absorbance recorded in the sample is subtracted the absorbance of the control (medium with XTT without cells) and this value is normalized by weight ratio of the scaffold. The final results are expressed as a percentage of cells seeded in the presence of HA²G50 and incubated for one day (Day 1) at 37 °C, in an incubator containing 5% CO₂.

1.3. *In vitro* determination of the HA²G50 effect on cellular morphology

The effect of HA²G50 on the morphology of A549 and HepG2 cells was studied by staining with hematoxylin-eosin or phalloidin-FITC and DAPI, to investigate the distribution of actin filaments and cell nuclei. In order to examine the hematoxylin-eosin staining, the bright field technique was used, while in the case of fluorescently labeled phalloidin and DAPI staining, the Inverted Microscope Olympus IX81 with fluorescence filters for excitation in UV, blue, green equipped with powerful software Cell Sense Dimensions was employed. Cell morphology and parameters such as: cell elongation, round cell appearance, nucleus / cytoplasmic ratio will provide indications of the state / condition of the cells within HA²G50 scaffold.

1.3.1. *Hematoxylin-eosin staining*

The principle of the method consists in the binding of hematin, a product of hematoxylin oxidation to the lysine residues of histones, under acidic conditions and the contrast of cellular details by eosin, an acidophilic substance that specifically binds to the positively charged amino acid residues (lysine, arginine) in the cytosolic protein composition.

At the end of the incubation period, cell-populated HA²G50 was fixed with a 4% paraformaldehyde solution (PFA) at 4 °C for 2 hours. Subsequently, the scaffold was washed with cold phosphate buffer, pH 7.4 and cryoprotected by sequential incubation in glycerol solutions of increasing concentrations:

- 5% glycerol solution, for 15 min, RT;
- 10% glycerol solution, for 1h, RT;
- 20% glycerol solution, overnight, 4 °C;
- 50% glycerol solution, for 1h, 4 °C;
- overnight incubation at -20 °C in 50% glycerol solution.

After cryoprotection, cell-populated scaffolds were included in the optimal cutting temperature (OCT) solution and subjected to final processing by performing 5-µm-thick cryosections. Briefly, the hematoxylin-eosin staining protocol consists of the following successive steps: incubation of cryosections with hematoxylin solution (6 min), treatment with 0.1% HCl (10 sec), incubation with eosin solution (30 sec), dehydration with 100% ethanol, clarification with xylene and mounting with balm from Canada. The colored cryosections are examined with the optical microscope under normal light (Nikon Eclipse Ti).

1.3.2. *Phalloidin-FITC / DAPI Staining*

The principle of the method consists in the binding of phalloidin conjugated with a certain fluorescent dye, phalloidin-FITC to the actin cytoskeletal filaments (with fluorescence in green) and staining of cell nuclei based on the strong binding of fluorescent dye 4', 6-diamidino-2-phenylindole (DAPI) to sequences rich in adenine - thymine base pairs from DNA (blue). Briefly, the protocol involves the following sequence: permeabilization of samples (cryosections

or scaffold) with cold 0.5% Triton X100 in PBS (pH = 7.4) (5 min), incubation with phalloidin-FITC 100 ng / mL in PBS (pH = 7.4) (dark, room temperature, RT, 40 min), incubation with DAPI 2 µg / ml in PBS, pH = 7.4 (dark, RT, 15 min). The examination of the samples is done using an inverted optical microscope (Inverted Microscope Olympus IX81 with fluorescence filters for excitation in UV, blue, green equipped with a powerful software Cell Sense).

In order to optimize the working conditions (seeding cell density, incubation time of scaffold populated with cells, etc.), a series of experiments, that involved HA²G50 seeding with one of the two cell lines and tracking cell viability and morphology over time, were carried out.

2. Results

2.1. The seeding of HA²G50 with A549 cells

The scaffold was previously cut (under stereomicroscope) to the following dimensions: L = 4-5 mm, l = 2-3 mm, h = 1 mm (the image corresponding to this scaffold is shown in Figure 62). It was observed that the sponge has inhomogeneous areas. At different points there are cavities that affect the perfect cutting. To obtain reproducible results we weighed the scaffold cut to the dimensions mentioned above. The scaffold was sterilized by exposure to UV radiation (3 min on each side). A549 cells were detached from culture plates with trypsin 1.25 % and resuspended in 5 mL complete medium (DMEM 1 % glucose, 10% fetal bovine serum - SFB, 1% penicillin-streptomycin - PS and 1% neomycin - N), cold. The resulting cell suspension was centrifuged at 1050 rpm, 4°C, 5 min. After this procedure, the supernatant was removed and the cell sediment was resuspended and homogenized in 1 mL DMEM 1 % completely.



Figure 62. Tested scaffold having the initial dimensions of L = 4-5 mm, l = 2-3 mm, h = 1 mm.

The cells were seeded by directly pipetting the cell suspension, corresponding to the cell density of $2.5 \cdot 10^5$ cells, on the scaffold placed in a 24-well plate. Following this procedure, the scaffold was kept idle for 10 min, and examined under the optical microscope (Figure 63).

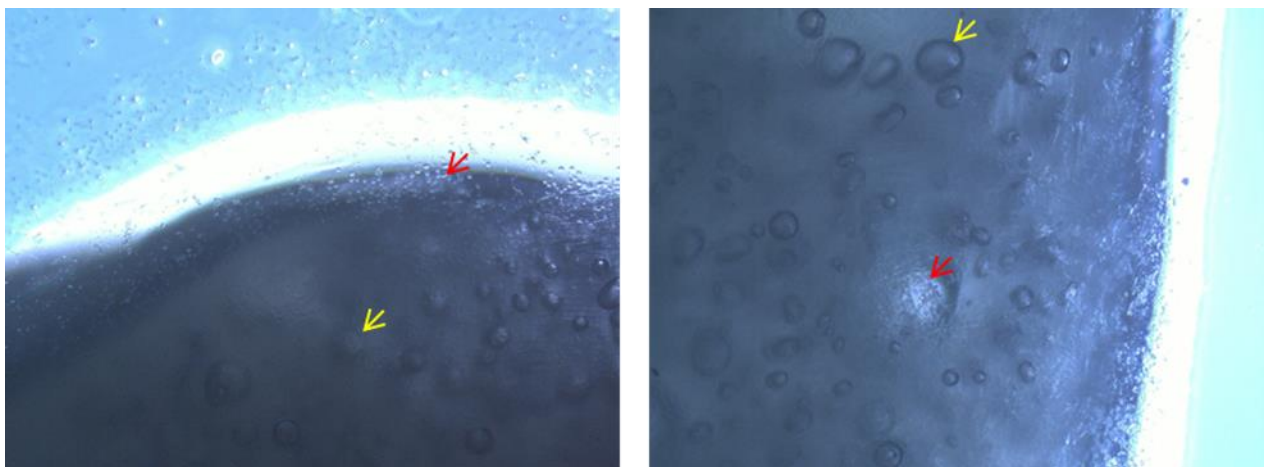


Figure 63. The examination of the scaffold immediately after the seeding with A549 ($2.5 \cdot 10^5$ cells). The yellow arrow indicates the presence of air bubbles and the red arrow highlights the cells on the surface (left), or through the scaffold pore (right). 5x objective.

At the end of the 10 min., 600 μ L of complete medium was added by pipetting on the wall of the well containing the scaffold populated with A549. The cell-populated scaffold was incubated for three days at 37°C, in the incubator. The culture medium has been changed daily. At the end of the experiment, the scaffold with the attached cells was subjected to 4% paraformaldehyde (PFA) fixation, cryoprotection in glycerol solutions of increasing concentrations (5-50%) and inclusion in OCT to perform cryosections on the Leica CM 1850 cryotome.

By optical microscope examining, it was observed the formation of a large number of air bubbles was observed inside and on the surface of the scaffold (Figure 63). Moreover, it was observed that about three thirds of the number of seeded cells remained on the scaffold, predominantly on the surface, while the difference of a quarter passed in the culture medium close to it (Figure 63-left). The color of the culture medium was rapidly changed from red (due to the existence of phenol red in the medium) to yellow, as a result of its acidification by the non-polymerized / unbound acid components of the scaffold, hyaluronic acid or maleic acid.

Before the changing of the medium and immediately after this, the scaffold seeded with A549 cells was examined at microscope. A slight deterioration of the construct within 3 days from the cells seeding was observed (small fibers detached from it and floated in the culture medium). A549 cells in the construct had a round appearance compared to the cells around the scaffold, which adhered to the plastic support of the plate (2D), these being spread out and elongated.

Scaffold cryosections populated with A549 cells obtained according to the protocol described above were stained with hematoxylin-eosin. Microscopic examination revealed that the scaffold has affinity for the two dyes, so the binding is nonspecific and the identification of cells adhering to the scaffold could not be made. Moreover, it was observed that the fibers in the scaffold were affected by the washing with hydrochloric acid, respectively xylene specific to the staining protocol (the images are not shown). Further, other cryosections obtained from this scaffold populated with A549 were stained with phalloidin-FITC (green) and DAPI (blue) (Figure 64).

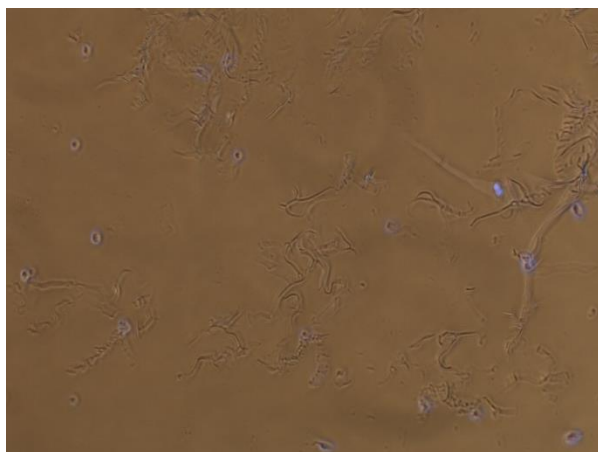


Figure 64. *The overlapping of phase contrast, DAPI (blue) and phalloidin-FITC (green) images for the same cryosection of the scaffold populated with A549 (seeding density was 2.5×10^5 cells / scaffold) and incubated at 37°C for 3 days. 10x objective.*

Following examination with the microscope, an inhomogeneous arrangement of the scaffold fibers was observed, possibly as a result of the cryoprotection processing, the cells are rare. An important observation is that the cells did not spread after adhesion (after 3 days) but remained round, as evidenced by the round appearance of the nuclei (blue) and the lack of cytoplasm, evidenced by the absence of actin filaments (that should appear in green) (Figure 64).

2.2. The seeding of HA²G50 hydrogel with HepG2 cells

(a). **In a first experiment**, 6 scaffolds were cut to the dimensions of L = 2-3 mm, l = 2-3 mm, h = 1 mm (the image corresponding to a scaffold is shown in Figure 65) were weighed

individually and sterilized by exposure to UV radiation for 3 minutes on each side. 24 h before cell seeding, the scaffolds were incubated in complete medium (DMEM 4.5 % glucose, 10% SFB, 1% PS), at 37°C, in an incubator that produces an atmosphere containing 5% CO₂, for removal of unpolymerized / unbound acids.



Figure 65. Tested scaffold having the initial dimensions of $L = 2\text{-}3\text{ mm}$, $l = 2\text{ mm}$, $h = 1\text{ mm}$.

It was observed that the culture medium rapidly changed its color from red to yellow when it came in contact with the scaffold. The culture medium was changed daily and microscopic examination was performed both before and after its replacement (Figure 66).

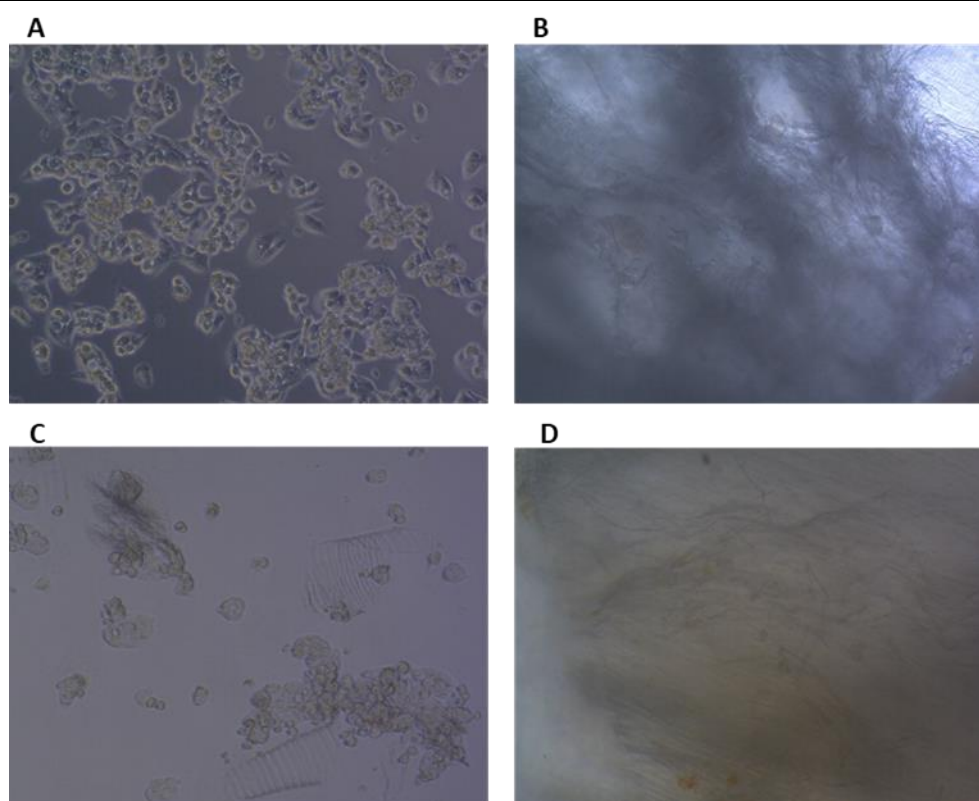


Figure 66. Optical microscopy images. A) HepG2 cells (7.5×10^4 cells / well) 24 hours after seeding on 2D cel culture plate 24 h; B) scaffold at 24 hours after seeding with 7.5×10^4 HepG2 cells; C) scaffold residues in culture medium, D) scaffold at 24 hours after seeding with 4.5×10^4 HepG2 cells and staining with XTT.

Prior to seeding with HepG2 cells, each scaffold was buffered on sterile filter paper to facilitate removal of excess media and subsequently placed in a 48-well plate. In parallel, the cells in the HepG2 line were detached from culture plates (2.5 % trypsin). The total number of cells was determined by counting on the hemocytometer using the optical microscope and the seeding was done at two cellular densities: 4.5×10^4 and 7.5×10^4 cells / scaffold. For each cell density, three scaffolds corresponding to the incubation period were seeded at 1 day (control, Day1), 7 days (Day7) and 14 days (Day14). After 24h, the scaffolds were transferred in other

wells, washed with colorless DMEM medium (without Phenol red) and incubated with XTT-PMS in DMEM for 3h, at 37°C, in an incubator. At the end of incubation, 100 µL culture medium (orange color) was transferred to a 96-well plate in duplicate and the color intensity was monitored spectrophotometrically.

It was observed that the scaffold retains the formazan removed from the cells and thus the diffusion of the dye from the cytoplasm of the cells in the culture medium is reduced (Fig. 5 D). Moreover, by daily microscopic examination, we observed that the cells in the scaffold remain round and gradually detach, floating through the culture medium, indicating that they are dead (Figure 66).

Cell viability, determined by XTT assay, supports microscopic observations, namely, cells remain in a metabolically inactive state, in which they no longer proliferate, an effect evidenced after 7 days from the cellularization of HepG2 cell scaffold at 7.5×10^4 cell density (Fig. 6). Moreover, in the case of scaffold seeded with HepG2 cells at density 4.5×10^4 for 7 days we observed a decrease in cell viability by more than 40% compared to the control scaffold (Day1) (Fig. 6). 14 days after the cellularization of HepG2 scaffolds, the complete reduction of the viability of HepG2 cells was observed (Figure 67).

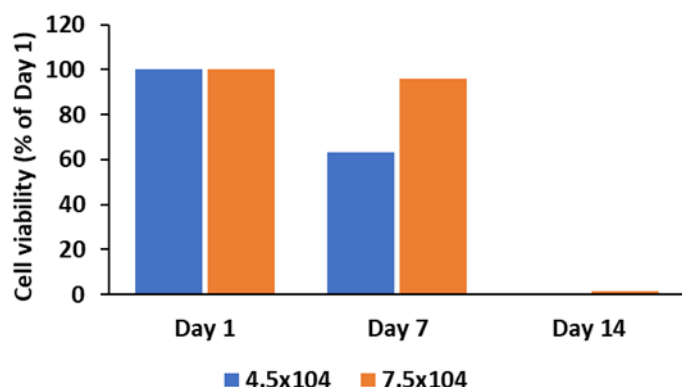


Figure 67. Effect of HA²G50 scaffold on the viability of HepG2 cells (4.5×10^4 and 7.5×10^4 cells / scaffold) at 1 (Day 1), 7 (Day 7) and 14 days (Day 14). The results are expressed as a percentage of the viability of cells incubated in the presence of scaffolds at Day 1, considered to be 100%.

Subsequently, the scaffolds were washed with PBS, pH 7.4, at room temperature, fixed, cryoprotected, included in OCT and sliced according to the procedure described above. The cryosections were stained with hematoxylin-eosin or phalloidin-FITC / DAPI. The hematoxylin-eosin staining revealed the same as observed for the scaffold populated with A549 cells. By staining with phalloidin-FITC and DAPI we observed that HepG2 cells seeded at the density of 7.5×10^4 cells / scaffold form clusters, predominantly in the scaffold pores, adhering to its filaments, but remaining round (round nuclei, lack of cytoplasm) (Figure 68).

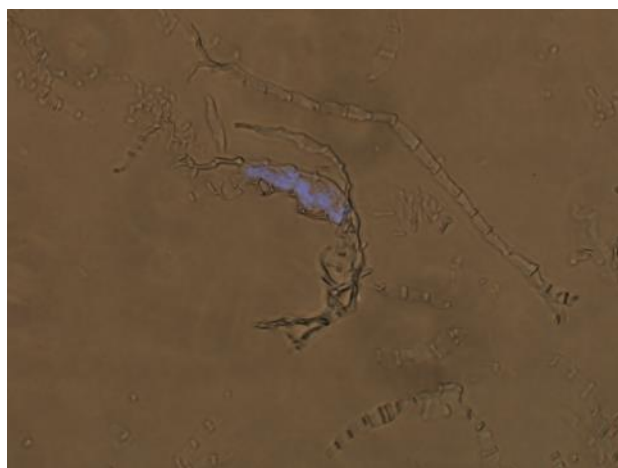


Figure 68. The overlapping of phase contrast images, DAPI and phalloidin-FITC for the same scaffold cryosection one day from the population with HepG2 cells (7.5×10^4 cells density); Objective 10x.

In conclusion, the number of HepG2 cells per section is low, likely as a result of seeding the scaffolds with cell densities too low or due to the loss of the connections established between the cells and the fibers in the scaffold's composition following cryoprotection procedures.

(b). **A second experiment:** seeding of four scaffolds with dimensions $L = 2-3$ mm, $l = 2$ mm, $h = 1$ mm with HepG2 cells at a higher density of 2.5×10^5 cells / scaffold and incubated at 37°C , in the incubator, for 1 day (Day 1, control), 7 days (Day 7), 14 days (Day 14) and 21 days (Day 21).

Sterilization of the four scaffolds was also done by exposure to UV radiation (3 min on each side). In this case, the scaffolds were immediately populated with cells at a density of 2.5×10^5 cells / scaffold. The culture medium was changed daily. Each scaffold was microscopically monitored before and immediately after the change of the culture medium and the observations were similar to those described above.

Moreover, it was noticed that the cells have a high affinity for the edges of the scaffold, where they adhere in clusters, and are missing from the central region of the construct.

At the end of each incubation period, 1 day, 7 days, 14 days and 21 days respectively, the scaffolds were carefully transferred to other plate, washed with colorless medium and incubated with XTT-PMS in complete, colorless DMEM for 3 h, at 37°C in a 5% CO_2 incubator to determine the effect of the scaffold on cellular viability.

Thus, the results of the XTT test (Figure 69) showed that after 7 days, the scaffold favors a slight proliferation of HepG2 cells as compared to day 1, but after 14 days it induces cell death in more than 25% of the cells tested day 7; the cell viability at 14 days being similar to the one observed at day 1, which suggest that either a part of the seeded cells die after 14 days as a result of detachment from the fibers of the construct or that the constructs are extremely non-homogenous and different areas of the same construct exert a completely different cytotoxic effect on the HepG2 cells that populate it. A very interesting fact is that in the time frame of 14 - 21 days after cell seeding, the cells adapt to the conditions of the scaffold and manage to proliferate, the viability of HepG2 at 21 days increasing by about 90% compared to day 1 (Figure 69).

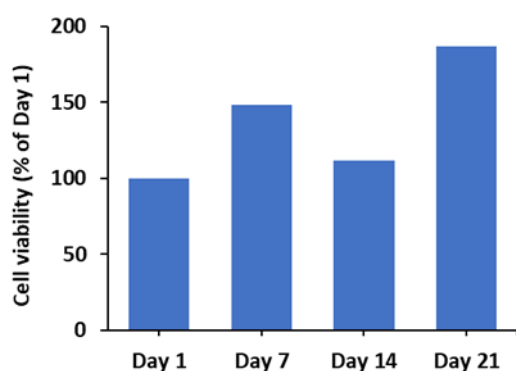


Figure 69. Effect of HA2G50 scaffold on the viability of HepG2 cells (2.5×10^5 cells / scaffold) at 1 day (Day 1), 7 days (Day 7), 14 days (Day 14) and 21 days (Day 21) after cellularization. The results are expressed as a percentage of the viability of the cells incubated in the presence of the scaffold for a day (Day 1), considered 100%.

The scaffolds subjected to the XTT test were subsequently washed with PBS, $\text{pH} = 7.4$, stained directly with phalloidin-FITC, respectively DAPI and evaluated by fluorescence microscopy, to reduce the drawbacks observed in the first experiment (when staining was performed on scaffold cryosections). After fluorescence microscopy investigation, the scaffolds were included in OCT and stored at -80°C until further processing (these determinations are in progress).

Fluorescence microscopy images support the above observations on the effect of scaffolds on cell viability, established using the XTT assay. It can be observed that the cells remain round between 1 and 14 days after seeding and further the lack of green fluorescence,

characteristic of the actin filaments marked with phalloidin-FITC, at the end of the 14 days after the scaffold's cellularization with HepG2 indicates the continuation of cells in a metabolically inactive state, which favors their detachment from the fibers of the construct (Figure 70).

Similar to the results of the XTT assay, where we showed an increase in the viability of HepG2 cells at 21 days after scaffold cellularization compared to the control (day 1), the microscopic images reveal that the cells begin to spread, around the cell nuclei (blue) a slight appearance of the actin cytoskeletal filaments (green) can be observed (Figure 70), which can be translated into the assertion that the cells that remained adhered to the construct fibers after 14 days begin to adapt to the scaffold conditions.

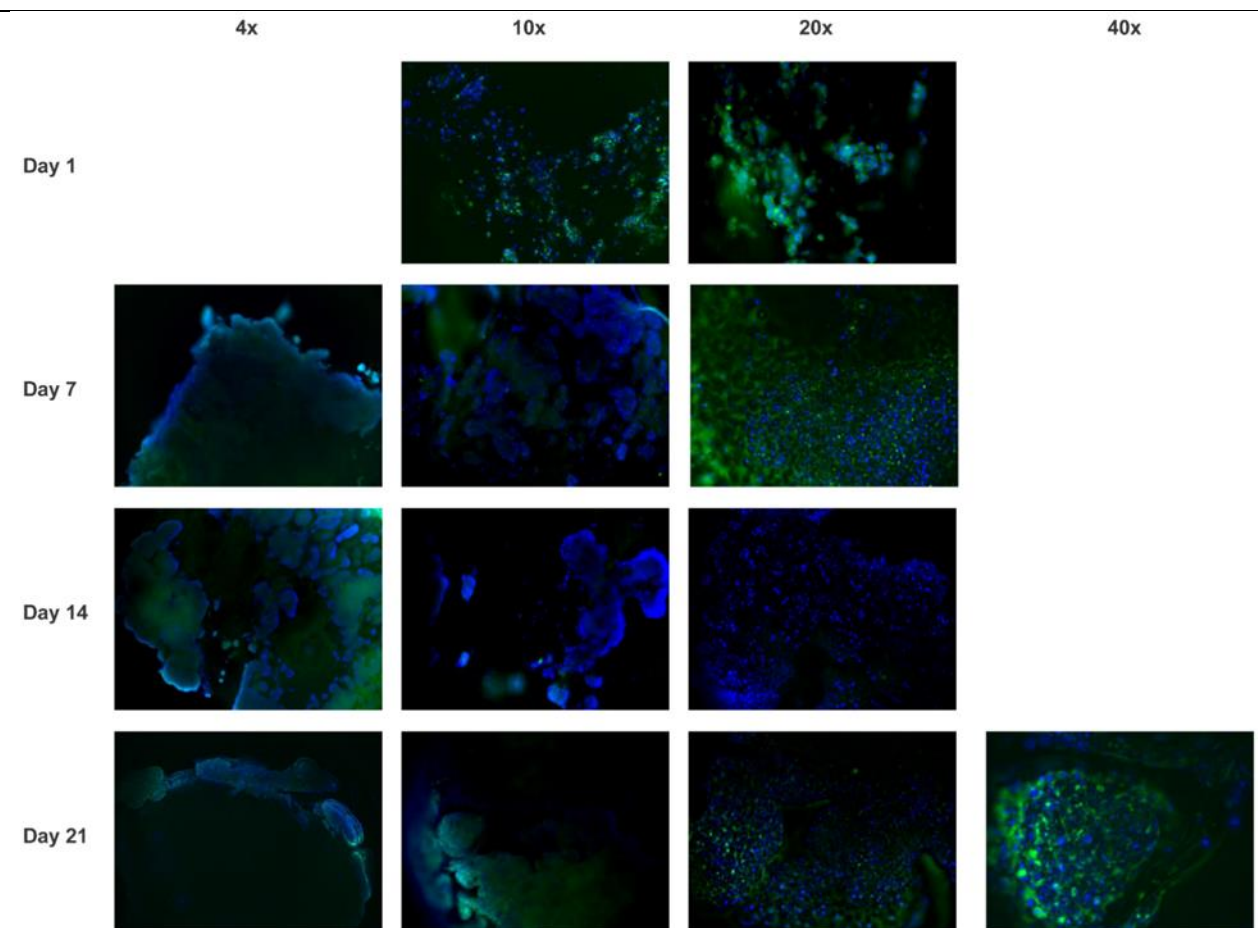


Figure 70. The overlapping of phase contrast images, DAPI and phalloidin-FITC images for scaffolds at 1 day (Day 1), 7 days (Day 7), 14 days (Day 14) and 21 days (Day 21) after the cellularization with HepG2, at 2.5×10^5 cell / scaffold density. 4x, 10x, 20x and 40x lens.

3. Conclusion

Although the results of then experiment that optimized the working conditions with the surrogate HA²G50 scaffolds are encouraging, the scaffold's inhomogeneity (pore size and possibly slightly different composition), the long time required for the cells to accommodate inside the scaffold and prolonged blocking of metabolic activity influence the expected results by phenotypic modification of the cells.

II. – Investigation of the HA³G50 as tumor surrogates populated with human tumor cells

In order to characterize scaffolds / sponge-type hydrogels based on hyaluronic acid (HA) and poly (methyl vinyl ether-alt-maleic acid) (G) (HA³G50) in terms of biological properties, they

were populated with human liver carcinoma (HepG2) cells. Scaffolds populated with HepG2 cells by seeding at a density of 2.5×10^5 cells/scaffold (2x2x1 mm) were monitored for: cell adhesion to HA³G50 (at 4 and 24 hours after seeding) and cellular cytotoxicity / proliferation induced at different time points: 1, 7, 14 and 21 days after seeding. On the other hand, HA³G50 scaffolds seeded with HepG2 cells were processed for investigation by optical and fluorescence microscopy to reveal the effect of HA³G50 matrix on embedded cell morphology, by highlighted the actin cytoskeleton (fluorescein-conjugated phalloidin - phalloidin-FITC) and the nuclei (4', 6-diamidino-2-phenylindole, DAPI).

1. Materials and methods

1.1. Cells

Hep G2 cells (human hepatocarcinoma cell line) were cultured in Dulbecco's modified Eagle's medium (DMEM) supplemented with fetal calf serum (10%), penicillin (100 U / ml), streptomycin (100 µg / ml), neomycin (50 µg / ml) at 37°C in a 5% CO₂ incubator.

1.2. Determination of HepG2 cells adhesion to HA³G50 scaffolds

For this purpose, HA³G50 scaffolds (2 mm x 2 mm x 1 mm) were individually weighed and sterilized by exposure to UV radiation for 3 minutes on each side. The scaffolds were seeded by directly pipetting the HepG2 cells suspension at a cell density of 2.5×10^5 cells/scaffold (4 mm³), on the scaffold placed in a 24-well plate. In parallel, for 2D experiments, HepG2 cells were seeded in a 24-well polystyrene plate (1.92 cm²/well) at the same cell density, 2.5×10^5 cells/2D support (control of adhesion). HepG2 cells seeded in 2D and 3D were incubated for 4 and 24 hours at 37 °C, in an incubator with 5% CO₂. At the end of the incubation period, the scaffolds were carefully moved into new wells and washed 3 times with phosphate buffer (PBS, pH = 7.4) to remove non-adherent cells. The cells seeded on 2D support were also subjected to the PBS washing procedure. Further, the cells that adhered to the scaffold and to the 2D support were trypsinized (0.25% trypsin), resuspended in PBS, centrifuged at 1050 rpm, 5 min, 4°C and counted. The number of adhered cells was normalized to the 2D surface or 3D scaffold volume.

1.3. Determination of HepG2 cells viability in 3D HA³G50 scaffolds

To determine the viability of HepG2 cells seeded in HA³G50 scaffolds, the XTT colorimetric assay was used. The reagent 2,3-bis- (2-methoxy-4-nitro-5-sulphophenyl) -2H-tetrazolium-5-carboxanilide (XTT) is taken up and transformed by the metabolically active cells into orange formazan in the presence of the reduction agent, methosulfate phenazine (PMS).

Four scaffolds were cut to the dimensions of 2 mm x 2 mm x 1 mm (as shown in Figure 71), weighed individually and sterilized by exposure to UV radiation, for 3 minutes on each side.



Figure 71. The tested scaffolds having the dimensions of about $L = 2$ mm, $l = 2$ mm, $h = 1$ mm.

The experiment consisted in seeding the HA³G50 scaffolds (placed in the wells of a 24-well plate) with HepG2 cells at a density of 2.5×10^5 cells / scaffold and incubating them at 37°C, in an incubator that produces an atmosphere of 5 % CO₂, for 1 day (Day 1, considered as control), 7 days (Day 7), 14 days (Day 14) and 21 days (Day 21). In parallel, HepG2 cells were seeded on 2D plastic supports (d = 15.6 mm, in 24-well plate) at the same cellular density and maintained under the same conditions as the scaffolds. The culture medium was changed daily throughout the incubation period.

After 24 h (Day 1) , the scaffolds were carefully moved into a new well. At the end of each incubation period, 1 day, 7 days, 14 days and 21 days respectively, the scaffolds were carefully transferred from in a new plate, washed with colorless medium and incubated with XTT-PMS in complete, colorless DMEM for 3 hours at 37°C, in a 5% CO₂ incubator. Also, the cells grown on the 2D supports were washed with colorless medium and incubated with XTT-PMS in colorless DMEM for 3 hours at 37 °C. The intensity of the orange color of the formazan resulted in the medium was quantified by measuring the absorbance at 450 nm using the infinite Tecan plate reader M 200. From the absorbance recorded in the sample is subtracted the absorbance of the control (medium with XTT without cells) and this value is normalized by weight ratio of the scaffold. For HepG2 cells grown on 2D supports, the difference between the recorded absorbance and that of the control was reported to the area of the 2D well.

The results were expressed as percentages relative to the results obtained for cells seeded on 2D and 3D HA³G50 scaffolds and incubated for one day (Day 1) considered to be 100% viability.

1.4. Determination of the HA³G50 scaffold effect on cellular morphology

The effect of HA³G50 scaffold on the morphology of HepG2 cells was studied by staining the cells grown in scaffolds with phalloidin-FITC, to investigate the distribution of actin filaments and with DAPI, for nuclei staining. The principle of the method consists in the binding of phalloidin conjugated with a certain fluorescent dye, phalloidin-FITC to the actin cytoskeletal filaments (with fluorescence in green) and staining of cell nuclei based on the strong binding of fluorescent dye 4', 6-diamidino-2-phenylindole (DAPI) to sequences rich in adenine - thymine base pairs from DNA (blue). Briefly, the protocol involves the following sequence: permeabilization of samples (scaffolds) with cold 0.5% Triton X100 in PBS (pH = 7.4) (15 min), incubation with phalloidin-FITC 100 ng / mL in PBS (pH = 7.4) (dark, room temperature, RT, 90 - 120 min), incubation with DAPI 2 µg / ml in PBS, pH = 7.4 (dark, RT, 15 min). The examination of the samples is done using an inverted optical microscope (Inverted Microscope Olympus IX81 with fluorescence filters for excitation in UV, blue, green equipped with a powerful software Cell Sense). For this purpose, the scaffolds subjected to the XTT test were subsequently washed for 2-3 times with PBS, pH = 7.4, stained directly with phalloidin-FITC, respectively DAPI and evaluated by fluorescence microscopy.

2. Results

2.1. Determination of HepG2 cells adhesion to HA³G50 scaffolds

It can be observed that approximately 50% of HepG2 cells seeded on 3D HA³G50 scaffold adhere and infiltrate to/in the scaffold volume at 4 hours after seeding, whereas in the case of 2D support almost all seeded cells adhere to the well' surface (Figure 72a, and 72b). This result can be explained by the fact that the scaffold placed in a 24-well plate cover a surface of 0.004 cm² from the total of 1.92 cm². Although the seeding was done in a small volume (6 µl) of medium on each side of scaffold to allow the cells to infiltrate into the depth of the scaffold, half of them migrate from the scaffold and attach to the well surface. However, the ratio between number of adhered cells at 24 hours and 4 hours is approximately 1.4 for both 2D supports and 3D scaffolds, suggesting that HepG2 cells proliferate at a same rate both in the case of seeding on 2D support, and in the case of seeding on 3D HA³G50 scaffolds. This observation indicate that the HA³G50 scaffold is a non-cytotoxic support for HepG2 cells, ensures the interaction of the cells with the fibers in its composition and promotes their proliferation.

The cells were seeded at the cell density of 2.5x10⁵ cells / scaffold or 2D support. The number of attached cells was reported to the volume (4x10⁻³ cm³) of 3D scaffolds or to the area (1.92 cm²) of 2D support. Control represents the initial number of cells seeded on 3D-scaffold or 2D support (2.5x10⁵ cells) / cm³ or cm²). The results are expressed as mean ± SD of values from 2 independent experiments made in duplicate and analyzed using the independent t-student test; **p < 0.01 vs. 2D and 3D HA³G50 scaffold at 4 hours.

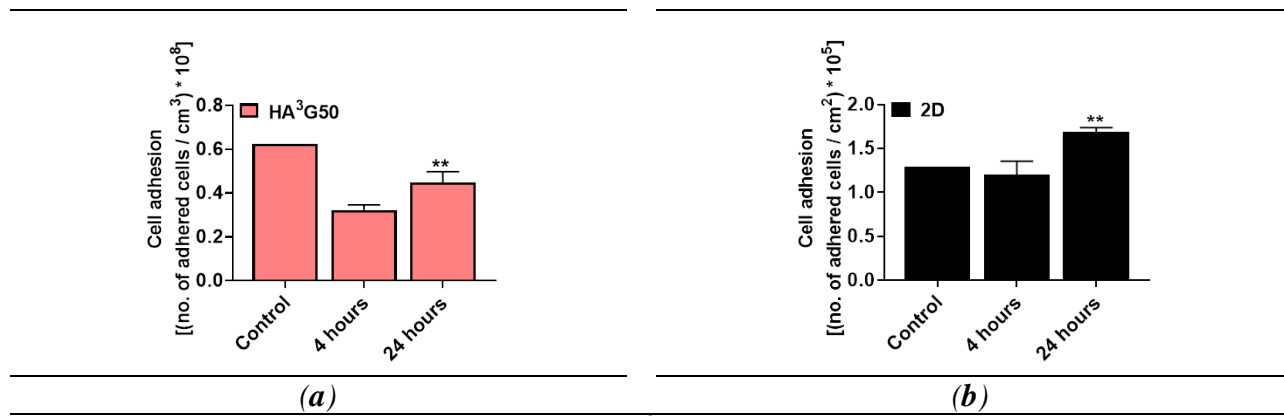


Figure 72. HepG2 cell adhesion to the HA³G50 scaffold (a) and to the 2D support (b).

2.2. Determination of HepG2 cells viability in 3D HA³G50 scaffolds

The results of the XTT assay (Figure 73) demonstrated an increase in terms of the cells' metabolic activity at 7 days after seeding, indicating that the scaffold promote the proliferation of HepG2 cells compared to day 1 (59 % increase, $p < 0.01$). The metabolic activity of HepG2 cells seeded on 2D support slightly decreased at 7 days compared to day 1 (by 20 %, $p < 0.001$), due to overpopulation of the available surface and formation of cell cluster (with apoptotic, inactive cells) instead of a monolayer with active, viable cells, in the absence of trypsinization recommended at 3-5 days.

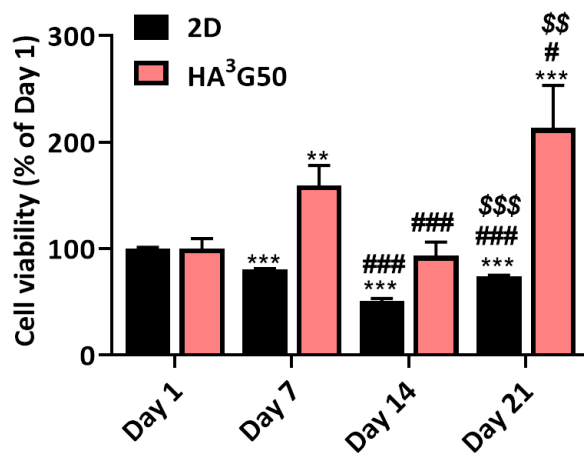


Figure 73. The viability of HepG2 cells seeded on 2D support and HA³G50 scaffold and grown for 1 day (Day 1), 7 days (Day 7), 14 days (Day 14) and 21 days (Day 21) from seeding.

The results are expressed as a percentage of viable cells grown on 2D support or 3D HA³G50 scaffold for 7, 14 and 21 days relative to the values obtained at Day 1, considered as 100%. *** $p < 0.001$ versus Day1, # $p < 0.05$, ### $p < 0.001$ versus Day 7, \$\$ $p < 0.01$, \$\$\$ $p < 0.001$ versus day 14.

At 14 days after seeding, the viability of HepG2 cells was significantly lower in both the scaffold (41.5%, $p < 0.001$) and the 2D support (37.5%, $p < 0.001$) as compared to day 7 (Figure 74). This may be due to the detachment of cell clusters whose cells directly attached to the 2D substrate or to the lose of contacts between cells and 3D scaffold, causing the entire cell cluster to be removed when replacing the medium. At 21 days, it can be observed increases in the proliferation of HepG2 in 3D scaffolds by approximately 100% ($p < 0.001$) compared to day 1, by 34% ($p < 0.05$) as compared to day 7 and by 129% ($p < 0.01$) versus day 14 (Figure 73). In the case of cells grown on 2D support, a slight increase in cells' metabolic activity is observed at day 21 (48%, $p < 0.001$) compared to day 14, a fact that can be explained by the creation of new cell-free areas, as a result of cell detachment from the substrate and subsequent proliferation of remaining attached cells in these spaces.

2.4. Evaluation of the HA³G50 scaffold effect on cellular morphology

Fluorescence microscopy images (Figure 74) support the observations mentioned above regarding the effect of scaffolds on cell adhesion and viability/proliferation (Figures 72 and 73).

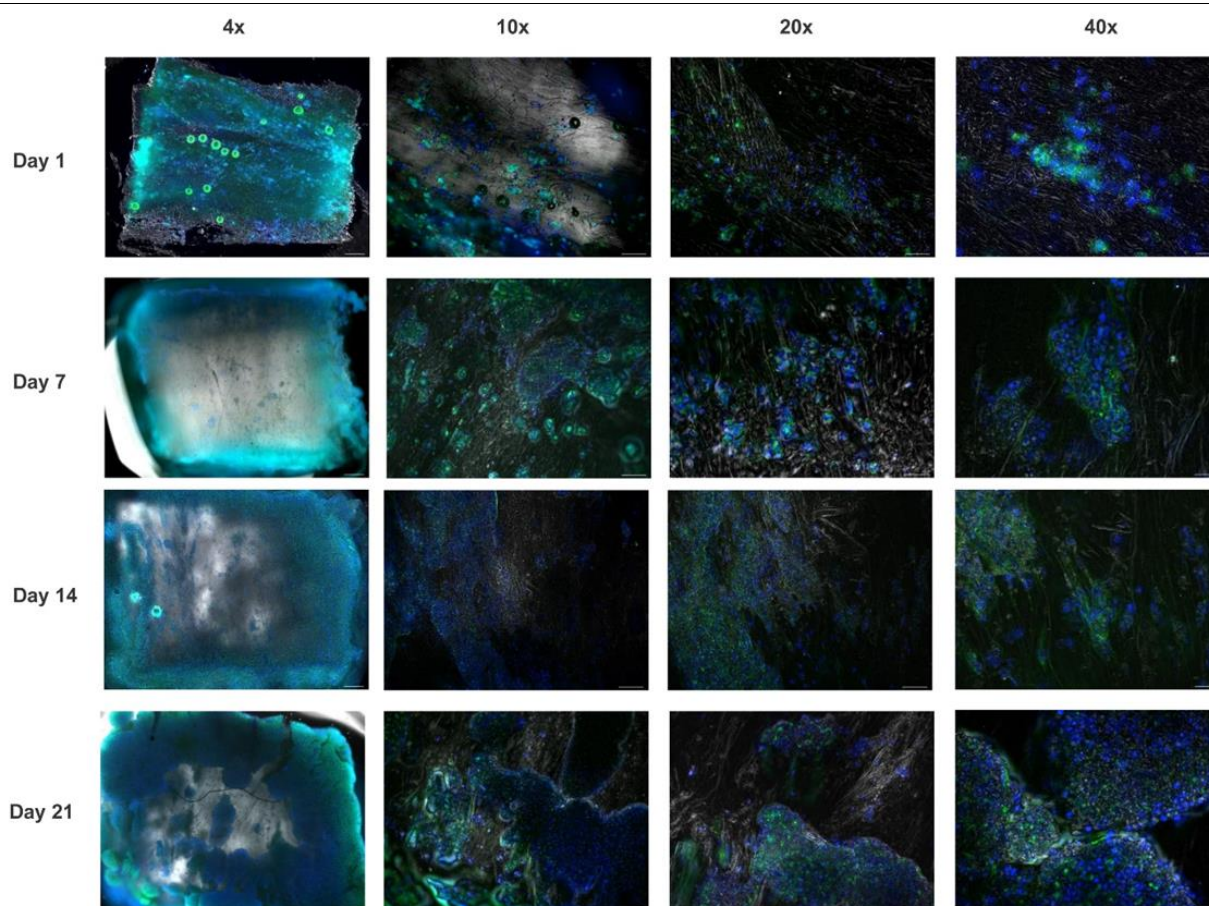


Figure 74. The overlapping of phase contrast images, and fluorescence images for DAPI and phalloidin-FITC taken at Day 1, Day 7, Day 14 and Day 21 after HepG2 cells seeding on scaffolds. Images taken with objectives 4x (scale bar: 200 μm), 10x (scale bar: 100 μm), 20x (scale bar: 50 μm), and 40x (scale bar: 20 μm) are shown.

It was observed that the cells adhere to the scaffold fibers and spread in the time range Day 1 - Day 21 from the seeding, an aspect highlighted by the green fluorescence amplification, characteristic of the actin filaments (phalloidin-FITC) around the blue fluorescence, specific to nuclei (DAPI) (Figure 74). The images obtained with the 10x, 20x and 40x objectives were taken in the central zone of the scaffold. The cellular proliferation at the edges of the scaffold is significantly enhanced in comparison with that observed in the middle of scaffold, probably due to an increased diffusion of nutrients from medium. Nevertheless, the fluorescence images show that HepG2 cell also proliferate at a high rate in the center of the scaffold. This increased tendency of the cells to proliferate and to form cell clusters, especially on the scaffold edge was more pronounced at Day 14 after seeding, which may explain the easy detachment of the cellular clusters from the support (Figure 74). After 21 days from seeding, cells proliferate in almost all available areas of the 3D scaffold (extremities and center), outweighing the tendency of formed clusters to detach and to be removed when the used medium is refreshed.

It can be concluded that HepG2 cells grown in HA³G50 scaffolds are metabolically active, proliferate and manage to populate a large area of scaffold at 21 days after seeding.

3. Conclusion

The biological investigations indicate that HA³G50 scaffolds are non-cytotoxic and able to support attachment, proliferation and viability of HepG2 cell, being thus suitable for using as tissue/tumor surrogate.

III. – Evaluation of the efficacy of natural antioxidants by electrochemical methods

In the past years, a great level of attention focused spices as sources of antioxidants. The antioxidant properties are caused by the presence of compounds from different classes, such as vitamins, flavonoids, terpenes, carotenoids and phytoestrogens, which enable the use of spices as food preservatives. Natural antioxidants in spices are particularly attractive because they do not possess high toxicity [84].

Among the various natural antioxidants, phenolic compounds are reported to be active, quenching oxygen-derived free radicals by donating hydrogen atom or an electron to the free radical. Recent studies point to the capability of plant extracts (like black pepper) to have similar patterns of phenolic compounds and their antioxidant activity was attributed mainly to their active principle, piperine [85]. Piperine, a naturally occurring alkaloid extracted from *piper nigrum*, has numerous demonstrated health effects and beneficial therapeutic properties which are systematically reviewed [86]. The antiinflammatory effect of piperine has been demonstrated in *in vitro* experiments, showing to protect against oxidative damage by inhibiting or quenching free radicals and reactive oxygen species and hydroxyl radicals [87]. The reported studies based on *in vitro* experiments point out that piperine has become one of potential candidates of antioxidants, but little attention has been paid to its chemical or electrochemical oxidation mechanism.

Our study focused on the electrochemical investigation of piperine using voltammetric techniques and different conditions to fully understand its oxidation mechanism. Electrochemistry is particularly useful to characterize the reducing potency of a compound, and controlled-potential techniques, such as cyclic voltammetry is commonly applied to rapidly assess the possible antioxidant activity. Low oxidation potentials values reflect the propensity of a given molecule for electron donation and thus, for exhibiting significant antioxidant (antiradical) activity. Therefore, determinations of the oxidation potentials can be employed to investigate the antioxidant activity. For many phenolic antioxidants, the reaction involves the transformation of a phenol moiety to a quinone, a typical feature for the oxidation process taking place in the 300–700 mV region [88]. Since piperine has no –OH groups, their redox behaviour was compared to that of some phenolic antioxidants chosen as reference: ascorbic acid, protocatechuic acid, syringic acid and tyrosine, given their ability to engender great electro-oxidation current.

The electro-oxidation of ascorbic, syringic, protocatechuic acids, tyrosine and piperine was followed by cyclic voltammetry in 0.1 M HClO₄ at carbon electrodes (Figure 75).

It is found that the individual reference antioxidants used in this study (ascorbic acid, syringic acid, protocatechuic acid and tyrosine) are oxidized in acidic media at rather low positive potentials, which is probably depending on the number of their hydroxyl groups [89]. The standard antioxidants are oxidized in one step to form the corresponding o-quinone. In contrast to the studied phenolic antioxidants, piperine has no –OH groups at the aromatic rings that can be further oxidized. The most probable and unique site for oxidation is situated at the central segment of the molecule at carbon atoms involved in the two double bonds. The oxidation processes occurs in three steps as indicated by the three anodic peaks (Figure 75e) probably involving the formation of a piperine diol, followed by subsequent oxidation to a dione compound, which is further oxidized by breaking the bond between the two carbon atoms, with the formation of two carboxylic acids. When scanning the potential in the reverse direction, the process is accompanied by a reduction reaction, followed by dimerization and gradual passivation of the electrode surface, as indicated by the strong diminution of the peaks for repeated scans (fig. 1e, dotted line). The dimerization of piperine was intensively studied by Nikaido et al [90], who examined the cycloaddition reaction in the presence of cobalt-phosphine complexes as catalysts.

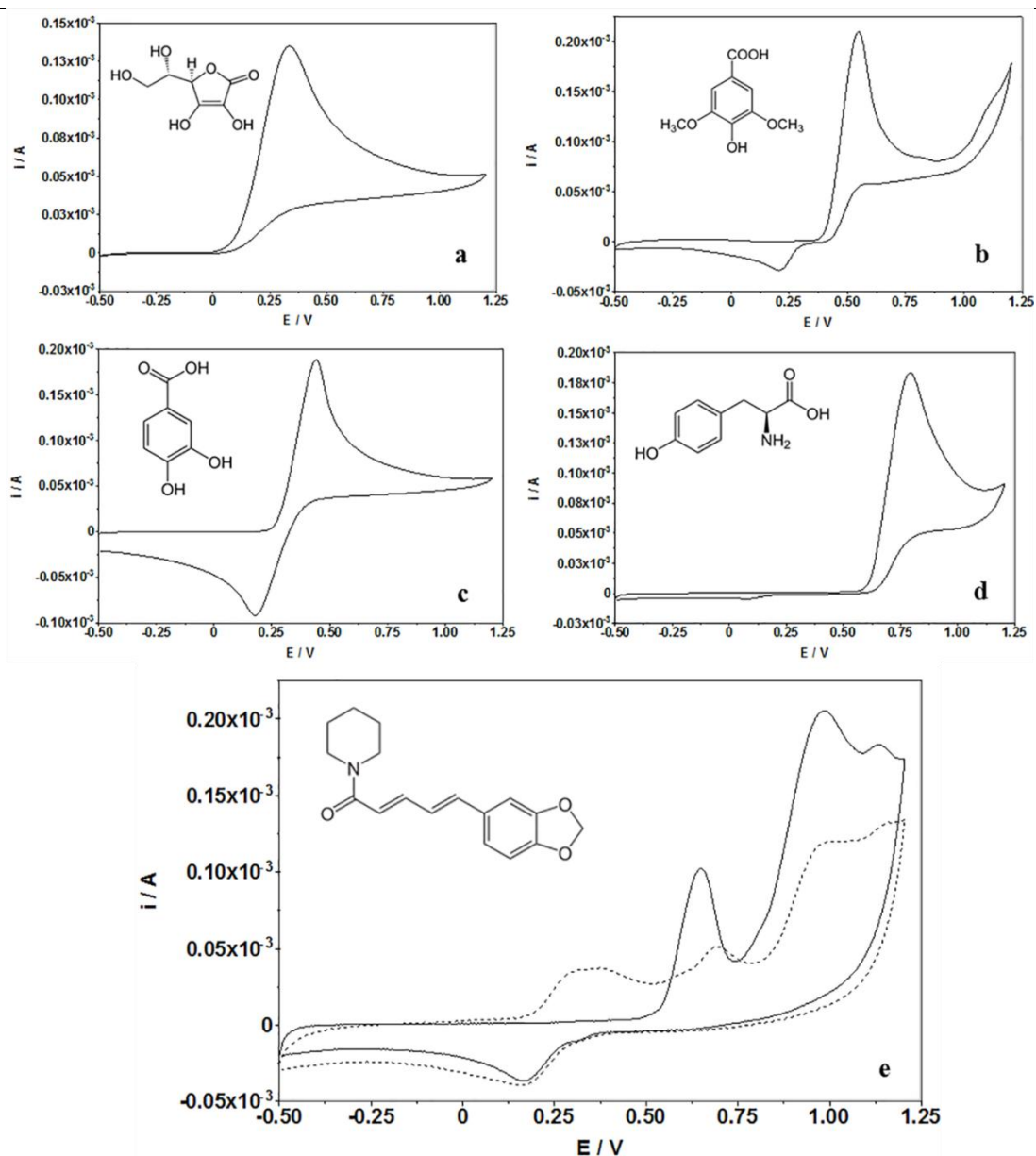


Figure 75. Cyclic voltammograms of 0.5 mM (a) ascorbic acid, (b) syringic acid, (c) protocatechuic acid, (d) tyrosine, and (e) piperine in 0.1 M HClO₄.

The antioxidant ability of piperine, along with the reference antioxidants are evaluated comparatively by means of cyclic voltammetry and differential pulse voltammetry adjusted to different peroxidation models assays: (i) 2,2,6,6-tetramethylpiperidiny-1-oxyl (TEMPO) scavenging; (ii) 1,1-diphenyl-2-picryl-hydrazyl-free radical (DPPH) scavenging; (iii) ferric ions (Fe³⁺) reducing power; (iv) hydrogen peroxide (H₂O₂) scavenging. The typical example of a radical scavenging assay is presented in Figure 76, showing the ability of piperine to change the redox peaks characteristic for DPPH[•] after their incubation. The decrease of all the peaks after mixture incubation indicates the partial consumption of DPPH[•] with the formation of neutral DPPH-H by taking up a proton from piperine.

The assay developed and optimized within the scope of this study can be recommended as simple, rapid, reliable and inexpensive for the determination of antioxidant activity of different molecules. The proposed assay does not require enzymes, artificial radical species, chemiluminescent reagents or biological tissue.

The results showed that piperine readily reacts with highly oxidizing radicals and can also bind redox-active metal ions, thus underlying that piperine can probably operate as a

proficient antioxidant. Also, the present studies indicate that the potential scavenging abilities of antioxidants might be due to the active hydrogen donor ability.

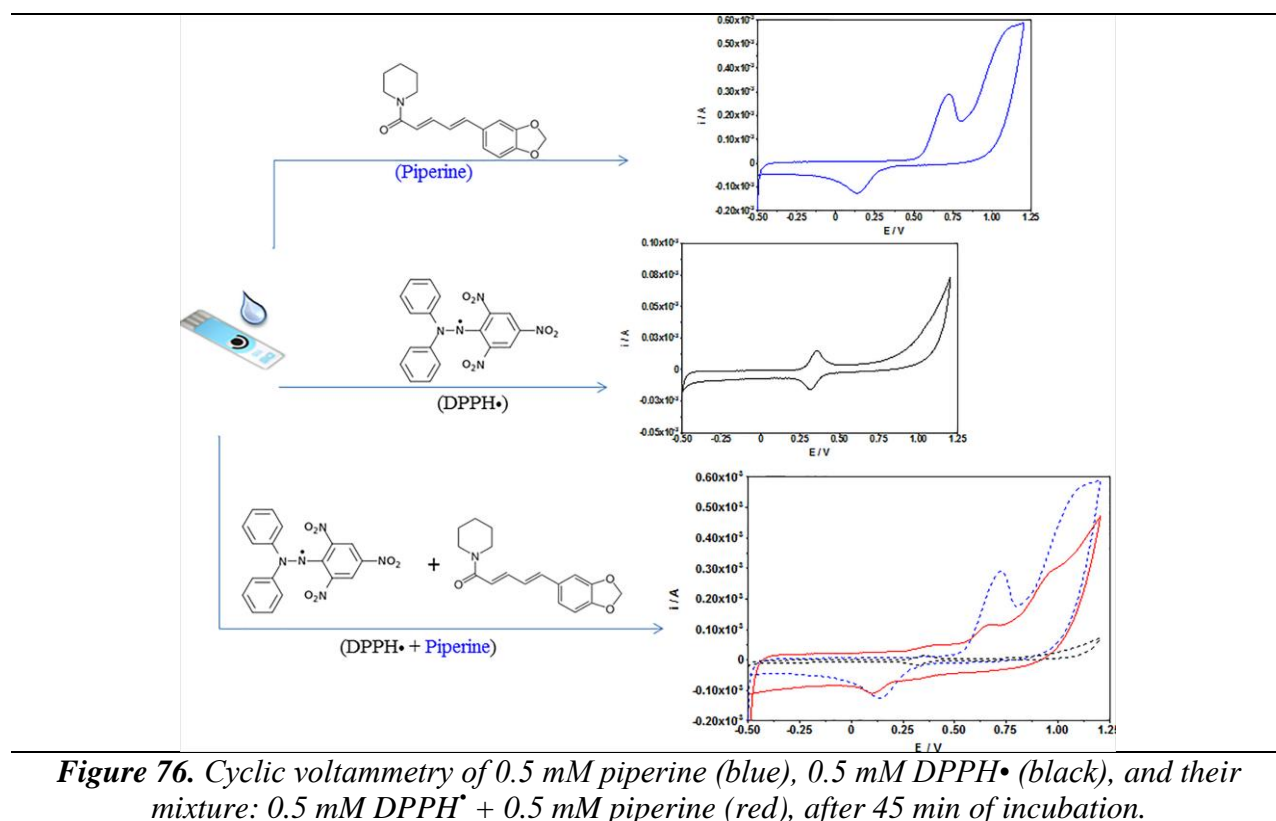


Figure 76. Cyclic voltammery of 0.5 mM piperine (blue), 0.5 mM DPPH• (black), and their mixture: 0.5 mM DPPH• + 0.5 mM piperine (red), after 45 min of incubation.

A.6. *In silico* approaches on delivering systems adapted for macro- and supra-molecular constructs

I – *In silico* studies of multi-responsive polymers as vectors for drug / gene delivery and controlled release

Using tools from atomistic to meso-scale we will simulate the chain of processes needed to describe a cancer drug delivery and its controlled release using an amphiphilic multiple stimuli-responsive block copolymer vehicle. In this respect, the systematic approach consists of six steps (shown schematically in the Figure 77): (1) finding the polymer system, tuning its responses to the specific internal conditions found in tumour cells and loading the drug inside the vehicle, (2) transport of the vehicle in the blood flow to the target, (3) its binding to membrane of the cancer cell, followed by its endosomal uptake and translocation and (4) the endosomal escape followed by (5) controlled release of the drug by stimuli and finally (6) degradation of the vehicle.

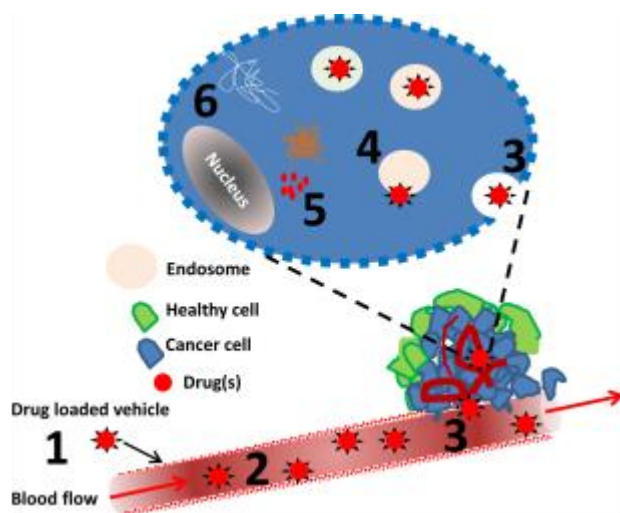
The simulations are carried out in parallel with experiments (synthesis, characterisation and performance of the delivery) with the same polymers and drugs, as well as conditions (as close as it gets). Completing the above steps will allow us to construct a kinetic model with the average times and rate constants extracted from simulations to identify possible bottle necks and to optimize the delivery and release process. And if detailed enough, also to perform stochastic simulations covering same time scales as in the experiments. Of the steps above (2), (3) and (5), have been modelled previously (also by us), but not the entire chain.

Introduction of the problem and motivation behind the work

Research and technology on nanoscale have brought together scientists from most diverse disciplines to discover new smart and functional materials. The fast development in

nano-technology, focusing on innovative nanomaterials and their applications in nanomedicine and diagnostics during the last two decades, make us to hope for a healthier future and longer life [91], but also worried as some of the development with the tiny nanoparticles may turn out to be (bio)toxic and things go out of control. Although not having delivered much so far, nanomedicine continues to have a large hype factor so an objective analysis of its status, promises and benefits would be required and weighted against its potential hazards to humans and nature. More (self-) critical research and better communication to public are needed to balance our hopes and worries.

Figure 77. The steps in studying complex delivery systems of biomedical relevance.



In a forward approach, the engineering pathway of loading, transport, transfer, releasing, tunneling, and diffusion-reaction and action-kinetics of active macro- / supra-molecular species are considered as unit processes able to be modelled.

In a backward approach, the molecular biology elementary actions are treated, starting from the requirements of internal cell delivery, and, in a manner of deconstructing complex systems, ending with the (bio)chemical steps of design and synthesis of both active species and their engineered vectors.

The human genome project has taught us that a majority of our diseases have a genetic origin in specific mutations of our DNA. To either knock out the mutated gene or to use healthy genes as medicine to replace the mutated one would be ideal therapy [92]. To administrate naked DNA same way as commonly used medicines is not a reliable option and a technology to deliver DNA directly right to the target cell, avoiding all the barriers, is still only a vision. Meanwhile a great variety of delivery and release systems have been suggested using biocompatible functional nanomaterials to build a vehicle (vector) for either passive or active targeting of the gene. The basic idea is to embed the gene inside a carrier which gives a good protection but also has the functionality to guide and assist the vector to the diseased cell and penetrate the cell membrane via endocytosis or other mechanisms and release the gene to enter the cell nucleus to take part in the next cell cycle. Soon after delivering its cargo the vehicle should degrade itself without leaving any toxic waste.

Viruses did evolve during the evolution to highly efficient parasites and carriers of biological material, developing ingenious ways to enter the cells to transfer genes to infect them. Before getting there they have to pass successfully many barriers and defeat the immune system. For this, the viruses, with a character of armoured vehicles, have developed their own efficient counter mechanisms. To engineer viruses by replacing the infecting gene with a therapeutic gene appears therefore appealing and was tried first time already a half a century ago. Unfortunately, these modified viruses are difficult to produce in large amounts and their fixed size is a limitation. But more severely, when used in gene therapy they may introduce immunogenic reactions. There is a high continued interest in developing them [93] in spite of incidents where things have gone wrong in testing them on humans. Along with viral vectors there is development of non-viral vectors as safer and more flexible alternatives.

Non-viral vectors have many benefits compared to viral vectors when used in gene therapy and drug delivery, such as their safety and high stability, low immune response, and are cheap to produce and modify in large quantities [94]. They exist in a great diversity such as polymeric systems, inorganic nanoparticles, lipid based carriers and many types of conjugates. However, they suffer from a low transfection efficiency compared to viral vectors, especially *in vivo*. Both viral and non-viral, these vectors are like Trojan horses trying to carry a small guerrilla group (genes/drugs) unnoticed from the patrolling troops (immune system) to get inside the city walls (cell) to win the battle by surprise (combat the source of sickness). In spite of this simple resemblance it is a highly complicated enterprise and the ingenuity on how it can be done is quite incredible in those thousands of published scientific articles in the topic. Still, very few of these ideas did reach *in vivo* stage. As only very few of the experimental studies are carried out combined with molecular modelling we think it is about time to change it. And there are many good reasons.

Molecular modelling and simulations as *bottom up* methods meet today several experimental *top down* techniques to study the very same phenomena at the corresponding length and time scales (meso-scale). Also, practically all analytical instrumental techniques in laboratories and their principles of operation on molecular samples can be connected to, and compared with results from computer modelling. However, molecular modelling has not been used very much to study gene/drug delivery and controlled release because of the high biological complexity and extensive length and time scales required. Also conventional particle and physics based models and techniques are not sufficient but need to be combined with stochastic and kinetic methods when approaching cellular environments and also complemented with data-based tools and informatics, including machine learning to obtain reliable input data and find correlations and dependencies at all stages of simulations. New methodological developments and interdisciplinary approaches provide finally an opportunity to carry out a project like this. However, it should be stressed that at the very end a modelling study will be successful only when deeply coordinated step-by-step collaboration with skilful experimentalists telling how reality looks like.

In 5D-nanoP project we use polymers to construct the vehicle for drug and gene delivery. With “polymers” we mean here synthetic polymers omitting at the moment natural polymers like chitosan since they are not structurally stable enough and may induce immune response. With the “drug” in this work we mean a cancer drug used in chemotherapy and typically Doxorubicin (DOX) as it is used as a prototype in many studies. Near to its isoelectric point $pI = 8.25$, the net charge is roughly zero and the electrostatic interactions are minimized so it can easily get physically adsorbed in the pores of polymeric structures. DOX is soluble in water at low pH but insoluble at alkaline pH. With the “gene” we mean here a small DNA oligomer used in gene therapy. In this project we can consider them both in equal terms from the computational point of view as they both will be targeted to cancer cells. The term “drug” from now on also means “gene”.

Polymeric systems offer a high flexibility and a large number of architectures and interactions to close drugs/genes inside or at the periphery. Cationic polymers, in particular, interact with negatively charged DNA through electrostatic interactions preserving a part of the positive net charge to interact with negatively charged cell membrane in endocytosis. Polymers offer nearly endless possibilities to permute different types of monomers with tailored substituent groups and by combining differently charged polymeric structures as block copolymers they can be made partly hydrophobic partly hydrophilic and as amphiphilic structures they assemble in water to micelles and vesicles and other three dimensional structures. They can form hydrogels in which physically or chemically connected backbones form matrices filled with a large amount of water providing a tissue mimicking environment. The most useful property in this project is that certain polymers are (or can be made) stimuli-responsive [95]. As the interior of tumour tissues has a microenvironment which differs from that of healthy ones, our polymers can be tailored to react to these conditions. For example, the temperature is locally

higher than normal body temperature and the pH is lower than in the blood where we assume that the vector is injected. Also, the redox potential is high and also the concentration enzymes associated with the specific types of cancer. Concentration of ions and their ratios differ in cancer cells compared to healthy.

The mechanisms to respond to stimuli are important in (i) cellular uptake and in (ii) controlled release of the drug/gene and in (iii) degradation processes of the carrier. With all local (T, pH etc) gradients in mind we can design our vehicle to respond to one or several *internal* sources of stimuli. In this project we choose three: temperature, pH and redox potential. It should be mentioned that there are also possibilities to design nano carriers responding to *external* stimuli such as ultra sound, electric/magnetic fields and light (radiation) etc, but these are not considered here, even if all of them could be modelled. *Besides responding to stimuli* it is important to design the vehicle to protect well the drug/gene, including itself, during the transport. The vehicle should be able to travel in blood flow without getting attention from macrophages (white blood cells) trying to dispose it because it is very important that the vectors have a long lifetime in the vascular circulation, this way increasing the chances to find the target cell and enter in it.

Details on the six steps involved

The whole project with its six steps (see Figure 77) will be described here as a pure computational project. However, it is performed in parallel and tightly coupled with experiments. Modelling and experiments are inter-dependent at several levels from synthesis to characterisation and measurement of the performance of delivery system. The project itself has an iterative character and failing at any of the steps **2-6** sends us back to step **1** for a further adjustment. Below we describe each step, giving first an overview and thereafter the key computational details. We use mainly methods, models and tools developed in my group or developed together with other groups. Also for visualisation we use gOpenMol software [96, 97] we did develop with Leif Laaksonen from CSC.

Molecular Dynamics (MD): M.DynaMix [98] and Dissipative Particle Dynamics (DPD): Galamost [99, 100] are the main tools throughout the project. All-atom MD is used whenever specific interactions are important, as well as to obtain effective coarse-grained (CG) potentials from atomistic simulations using the Inverse Monte Carlo (IMC). The IMC method [101, 102] is an accurate scheme for coarse-graining of complex general and biological systems. It can be used even for super-coarse-graining (coarse-graining of already coarse-grained models) and as a general tool for multi-scale modelling [103]. In delivery simulations to cover extended length and time scales all molecular systems (polymers, ligands, DNA, drug and water) are composed of CG beads. As soft potentials to obtain the conservative forces for DPD, we use *either* Flory-Huggins (FH) polymer models for which we need to obtain/calculate the interaction (repulsion) χ parameters for the conservative soft forces (PPPD has already many), *or* effective solvent mediated potentials calculated using IMC [104]. Electrostatic interactions are important in describing the pH-responsive mechanisms. Galamost uses (*ENUF*) the linearly scaling accurate Ewald summation method based on *Non-Uniform FFTs* [105].

Step 1. Optimizing the polymer material and packaging the drug/gene.

As the temperature-sensitive part we will use the hydrophilic homo polymer *N*-isopropylacrylamide (NIPAM). It undergoes a coil-to-globule transition above its lowest critical solution temperature (LCST) which is 32 °C in aqueous solution. By adding ionisable co-polymers to NIPAM will elevate the LCST over the normal body temperature (as in a cancer cell). By adding hydrophobic co-polymers containing an acidic-sensitive part will create a system responding to certain pH. By further connecting the hydrophilic and hydrophobic blocks with a redox sensitive linker, for example a disulfide bridge, can create altogether a triply sensitive block copolymer. Above the LCST after the collapse, the system is all hydrophobic and insoluble in water while at lower pH it becomes hydrophilic and dissolves in water. Also the linker bond is made to break in simulations.

More specifically, we plan to use block copolymers of type p(NIPAM_{xx}-SS-co-AA_{yy}...) as starting structures. Following [106] the “AAA” block is initially chosen as 2-hydroxyethyl methacrylate (HEMA) which is pH-sensitive. The alcohol group is protected with a tetrahydropyran (THP) derivative. Lowering the pH will expose the THP moiety from the polymer converting the hydrophobic block to PHEMA which is essentially hydrophilic. We will also test 4-vinyl-pyridine as AAA. The molar ratios of the monomers are denoted as “xx” and “yy”. As initially amphiphilic polymer placed in water it is expected to form micelles but also liposomal structures including polymersomes depending on block composition and block lengths and other details, where it is possible to load the drug/gene.

The suggested two starting structures above are chosen only as examples to initiate the project, while we need to explore carefully both the molecular and the chemical space to find the optimal polymeric structures. There are many data bases available of molecular structures: experimental, theoretical and even hypothetical. Similarly there are databases with physical and chemical properties of polymer materials, for example the Polymer Property Predictor and Database (PPPDB) [107] and PolyInfo [108]. We make much use of machine learning in the process following [109]. Already from the very beginning we start to build an ontology [110] of the materials and properties, which is a graph containing all data and meta-data we can collect. It will help us to navigate and see all inter-relationships between structures, properties, models and methods thereby giving us new ideas. We hope that it can be later linked to large established ontologies like the Open Biological and Biomedical Ontology (OBO) Foundry [111] to provide us a wealth of well-structured biological information.

Computational details: We will perform screening from databases and if needed using DFT calculations. Desired filters and descriptors are set and combined with (supervised) machine learning to add a predictive power to our search [109]. Using DFT and MD we can compute several characteristics such as pKa as well as solubilities, logP etc for the drugs and polymers involving free energy simulations [112, 113]. Using MD simulations we tune the LCST from 32 °C to ca 40 °C and to adjust the pH response we use the standard Henderson-Hasselbalch equation to estimate the number deprotonated carboxylic and other deprotonated groups at low pH conditions. We use the radius of gyration or number of H-bonds in MD simulations as indicators for collapse/swelling of the polymers. We use MD to simulate the loading of drugs either by diffusion or “mimicking” *in situ* loading and inserting the drug molecule inside and controlling the stability of the loaded vehicle. We have previously studied pH-responsive hydrogels as drug carriers [114] and drug loading in vesicles [115]. The final task in this step is to coarse-grain all the used molecules by mapping the atomistic molecular structures onto molecular CG structures made of large beads and verify them by comparing several AA and CG results. Note, that we can, when needed, do back-mapping from CG models to AA same way as we have done previously in [116].

Step 2. Transport of the vector in the blood flow to specific target cell

We simplify the blood to a constant flow with a parabolic hydrodynamic profile, as any viscous fluid in a capillary. Blood is a very complicated liquid mixture where the solvent is plasma (>90 vol% water) in which blood cells; red (containing haemoglobin to transport oxygen) and white (in duty for our immune system) and also platelets (for coagulation) are accompanied by proteins, fat, electrolytes, gases, and many other substances. Blood is a shear-thinning non-Newtonian fluid where viscosity increases by slowing down the flow. In our simulations we keep only the most important/ abundant components, namely, water, red blood cells (RBC) and the human serum albumin (HSA) proteins. One important reason to keep HSA is its role in moving metabolites, fatty acids and also drugs in our body. HSA also tends to bind to the nanoparticles and cover their surface to form a corona. How strongly it may bind depends on the size and shape, charge distribution and functional groups etc of the nanoparticle. In this way the vector can become unintentionally modified during the transport, affecting its selectivity to find the target as it may cover the crafted receptor-specific ligands. With the corona it can also make the

vehicle a target to macrophages swallowing it as part of immune defence. In modelling we investigate the forming of HSA corona and the effect of PEGylation (PEG = polyethylene glycol) which can reduce the adsorption of HSA. However, we do not model the macrophages.

Computational details: To make the blood and all its components to flow, an external force (pressure) is applied on them along the vessel which will get soon stabilized to a steady state. It is also important to describe well the behaviour of healthy RBCs in the flow and close to capillary wall. At the rest RBCs have a biconcave shape which is transformed to a parachute-like in the flow [117]. The high deformability of RBCs is important for them to get through narrow passages (not studied in this project). Several computational models exist for RBCs able to reproduce the behaviour of getting deformed. Normally 300+ beads are connected to a 2D network made of triangles kept together with harmonic springs within slightly fluctuating constant surface area and volume [117]. Both the diameter of the capillary and its molecular details and the flow velocity affect the morphology of RBCs. Blood flow is a complex molecular system and our aim is not to focus too much on the details but rather find a robust compromise in how to treat the rheology and boundary conditions. CG model is constructed for HSA which has 585 amino acids. In the direction of the flow periodic boundary conditions are used to describe a pseudo-infinite linear blood vessel with no branches or narrowings. Reflecting boundary conditions are applied on particles trying to penetrate the blood vessel wall. We use LAMMPS [118] which is already prepared for this type of non-equilibrium simulation and we have used it for other related systems [119], while in Galamost we need to implement a method with more realistic reflection boundaries together with proper adhesion behaviour for this problem. The simulations are performed at in blood normal physical/chemical conditions ($T=37^{\circ}\text{C}$ and $p\text{H}=7.4$). No corresponding experiment is planned though.

Step 3. Binding to the target cell membrane followed by endosomal uptake

As tumour tissues are already from the very beginning connected to the blood supply in order to get nutrients and oxygen to grow, our nano-carrier has found it thanks to the “enhanced permeability and retention (EPR) effect” which is universal to all types of tumour cells. EPR effect makes large macromolecules and nanoparticles to concentrate around tumour tissue more than healthy ones due to the leaky blood capillaries of the tumour tissue. EPR is connected to several characteristics such as lower pH and higher temperature but also a higher concentration of enzymes and reactive oxygen species (ROS) which is also the typical environment inside the cancer cell. There are many ways for nanoparticles to translocate across the cell membrane from endocytosis to direct penetration. Here we consider endocytosis and in particular with some help from receptors in the membrane and ligands we did attach to the nano-vehicle to get recognized by these receptors and to better initiate the engulfment of the vehicle.

Computational details: Computationally we study in this equilibrium simulation the cellular uptake by endocytosis using DPD and fine-tune the process of engulfment of the nano-carrier by lipid bilayer with receptors on the surface. In modelling the process, we have all nanoparticles we constructed in **Step1** but now we add also the CG lipids and receptors to be embedded in the lipid membrane. In the course of modelling the endocytosis we have the opportunity to further optimize both the amphiphilic stimuli-responsive polymer (its length and other characteristics) and its interactions with the cell membrane and also test systematically suitable combination of ligand(s) in the nanoparticle and receptor(s) in the membrane. Very important to study is also the effect of the carried drug/gene to endocytosis as well as PEGylation of the vehicle. We have performed a similar engulfment of PAMAM dendrimers by lipid membrane [120]

Step 4. Endosomal escape

Once inside both in the cancer cell and still in the endosome the vector needs to come out to cytoplasm. This is very tricky as non-viral vectors lack biological mechanisms for that in the same way the viruses and bacterial toxins have [91]. Obviously this part is also the most difficult

one to model as it is the most biological process taking place in a very complex environment the cell is. For us it appears to have very much a character of a “road block”. Currently no efficient escape mechanisms have been suggested in experiments either for non-viral vectors to escape from the endosome, which does not make it better for us. Here we think that modelling can scratch this problem and give important insight. In fact, in this subproject we can allow us to move outside the original system to test new ideas. In summary, this step leads us to test both agents and mechanisms to disrupt the endosomal membrane for a great escape.

Computational details: For letting the vehicle to escape from endosome we basically would need make a hole in the endosome or destabilise it with a shock to allow the vehicle to come out. However, we can test some hypotheses [30] of how facilitate the escape: We can drastically change the environment and use both internal and external stimuli. Using MD we will test mechanisms from [121] and specific agents to make a pore in the endosomal membrane in a way mimicking bacteria. For example, we can test fusogenic agents. We can use charged dendrimers like PAMAM connected to a so called proton sponge effect in which the radius of hydration (gyration) of dendrimers increases with lowering pH. This in turn is connected to increasing osmotic gradient/pressure inside. Finding ways to induce a destabilization or even a phase transition in the cytoplasmic membrane is another strategy. We use entirely AA MD in this step due to delicate interactions involved.

Step 5. Stimuli-responsive controlled release of the cargo

The interior of various tumour tissues have similar environment which differs that of healthy ones. This gives many opportunities to design a vehicle to respond to these internal sources of stimuli from the beginning in choosing the material to build the vehicle for a controlled release. We did choose temperature-, pH- and redox- sensitive polymers/copolymers. To use multiple responsive polymers increases generally the release efficiency [91] and will be now evaluated here.

Computational details: Our block copolymer which consists of acid-sensitive hydrophobic part and temperature sensitive hydrophilic part connected together with a disulphide bond. The polymer carrier with protonatable groups responds to low pH by swelling or gets degraded or dissolved. If we have applied PEGylation (to protect the carrier and prolong its life in blood), the lower pH in the vicinity of the cancer tissue could be now used to detach the PEG shield in. Unfortunately PEGylation makes the uptake of the nanocarrier more difficult so it should be removed before the contact with the cell membrane. A large part of the work is already done in **Step1** where we did tune separately the temperature and pH responses. Now we verify how all the stimuli-responses work together. These are equilibrium simulations to monitor collapse and swelling of the hydrophilic and hydrophobic parts, respectively by calculating end-to-end distances or radius of gyration in MD simulations to monitor these changes.

Step 6. Biodegradation of the vector after its release

We have chosen synthetic polymers in this study simply because it offers us numerous choices in designing them and they are mechanically stable [91]. At this last step the choice of natural polymers would have been better due to their higher biocompatibility/ biodegradability. However, they would not have survived the journey. We will study and optimize the degradation of the carrier and look into the toxicity aspects.

Computational details: Here we follow the degradation process which closely connected to the stimuli-responsive release of the drugs as the polymer vehicles are already broken. There are force field models and simulation techniques which allow breaking (and forming) of the disulfide bridge on due thermal agitation/destabilisation. To simulate the breakage of the disulfide bridge caused by high oxidation potential is not really doable using classical models and we will test three strategies (i) we parameterize it to break at the same temperature as the hydrophilic block collapses by higher temperature ($> LCST$), (ii) we apply QM/MM methodology [122] or (iii) we use our fast tight-binding-like DFT method [123] as *ab*

initio simulation engine. Experimentally it is expected break due to the high oxidation potential and we may use these results to parameterize our models for classical MD simulations. The purpose of this step is simply to follow the disintegration of the polymer vehicle. The vehicle should have a good biodegradability even as synthetic polymer. We will also perform MD simulations to study the interactions between the vehicle fragments and lipid bilayers for a possible toxicity.

Kinetic model (the final step)

After completing the steps (1) to (6) we should have information about the barriers and average times for different processes which we can translate to rate constants. This information can be used to create a kinetic model. Drug delivery and release using polymers is largely a diffusion-controlled stochastic process where convection, swelling, collapse, erosion and degradation (non-catalytic or autocatalytic) affect the diffusion. Steps and fragments of the whole process are now considered using molecular modelling across different length and time scales, however, only the main steps, with the fastest rate constants, have been included. We can also correlate our kinetic parameters with the data and parameters from our experimental colleagues. If we can estimate the kinetics even in rough terms, it will help us to further optimize the steps and remove bottle necks. However, we wish to go further and set up a stochastic simulation. The stochastic simulation algorithm (SSA) of Gillespie [124] is well rooted in cellular computing but we will use kinetic Monte Carlo (kMC) as we are more familiar with the method [125], and as both methods are closely related.

Computational details: In every step we need to identify the key processes and estimate their mean times to obtain the rate constants. We collect data of diffusivities of the particles (individually and in clusters) based on mean square displacements. We measure average times for shrinkage and swelling, packing and unpacking the vectors, rates of degradation etc. There is a very large number of processes and events, both transport and reaction (association, dissociation etc). We will start with a limited number and we add more when obtained from analysis of the trajectories. The purpose is primarily to have a rough model telling us which step needs improvement. We have to accept that we cannot model everything what our experimental colleagues can measure but also they cannot measure many things we can simulate. Here we should be able to see the fruits of combining the both worlds. Kinetic Monte Carlo needs a landscape as input where every state leads to several other states and the rate constants exist for a passage to the new states. On a long run the kinetic model can be extended to other types of vehicles as the steps are roughly the same but there are differences in the rates. If we succeed to create a detailed enough kinetic model (better than “rough”) containing also rate constants for less probable transitions we could simulate the delivery and release in more details, covering very long time scales corresponding those in the experiments [121]. The ontology will be found very useful [110] for creating the landscape.

State-of-the-art in the field of *in silico* modeling

5D-nanoP is an interdisciplinary project combining physics and knowledge-based materials modelling as well as multiple level life science modelling. We utilize here the most efficient methods, models and computational tools. For the current state-of-the-art we refer to following papers (which did inspire us): [126] for physics-based multi-scale modelling (connecting electronic, atomistic, mesoscopic and continuum models), for drug/gene delivery and release, [127] for pharmacokinetic multi-scale modelling, [128] for computational life science modelling, [129] for materials informatics, including high-throughput screening and Bayesian optimization, [130] for machine learning and statistical analysis for materials science.

As a very simple example how we can work together within **Step 1**, where the responses to certain temperature and pH, causing polymers to collapse and swell, respectively, can be tuned in a systematic way by modifying the polymer in simulations and simultaneously tested in

laboratory. Once the LCST transition for a thermo-responsive polymer takes place the appearance of the polymer solution changes from transparent to milky and can be quantified when transmittance makes a sharp drop from 100 to 0. In simulations we see the radius of gyration to decrease drastically at the same temperature interval. In this way we vary parameters, such as concentration, ionic strength, chain lengths, functional groups and hydrophobicity / philicity of the blocks, etc first in simulations before it is tested in laboratory. The **Steps (1) – (6)** can be performed both in simulations and in experiments (although not the one in the blood flow) and the results compared/verified. Occasionally data is also obtained from experiments to improve and calibrate the simulation model.

II – Identifying the interaction between PEG and PEI, and explaining the role these interactions have in DNA complexation

Efficient gene-therapy could be the holy grail of modern medicine, so the development of a perfect – non-viral carrier that will be able to fulfill all the administration, transfection and biocompatibility requirements is mandatory. We propose a vector that is composed of 4 parts, Squalene (as an aggregation agent and as a cellular membrane penetrator), Poly Ethylene Glycol (PEG) (as a biocompatibility agent and as a stealth agent), a phenol derivative as a fluorescent marker, and branched Poly Ethylene imine (PEI) (as a DNA binding agent). In order to understand the exact role these components have in DNA binding and condensation and how they interact with each other and with DNA, we have performed molecular dynamics (MD) simulations. The emphasis of these simulations was to determine how PEG interacts with PEI and if these interactions have any influence on the DNA binding capabilities. During our experimental work we had synthesized 3 vectors with three PEG chain lengths of 500 Da, 1500Da and 3000 Da, which were also used in our simulations (see Figure 78).

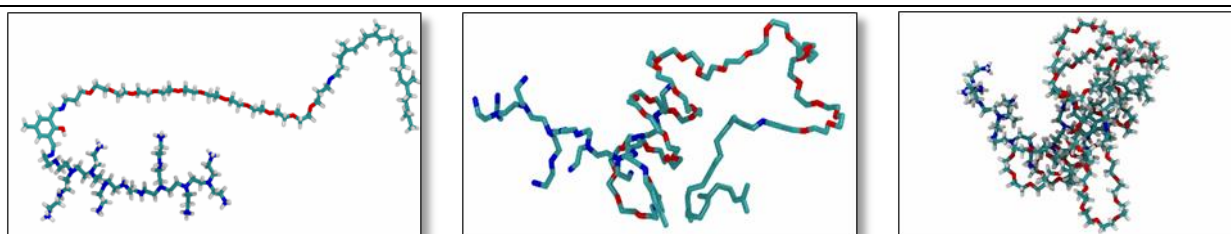


Figure 78. The three SQ-PEG-PEI vectors with a PEG chain (from left to right) of 500Da, 1500Da and 3000Da.

Prior to simulations, the vectors had to be built and parametrized. The structures were built using the Avogadro software and the atom type, bonds angles and dihedral parameters were obtained using AmberTools and GAFF2 forcefield. In order to increase the accuracy of the simulations, Quantum Mechanical calculations (QM) were used to fit the partial atomic charges. Because the entire molecules were too big for QM calculations they were split in smaller parts and the charges were calculated for each fragment and then put back together. The PEI segment of the vector was partially protonated (10 out of the 19 nitrogen atoms) in order to simulate a pH of about 7.4.

The actual simulations were done using the Gromacs 2018 software with the Amber Force Field. Six simulations were done in total: 3 to see the micellization process of the vector in water and 3 to study the interactions between the previously formed micelles and DNA. In order to simulate the micellization process 30 molecules were randomly distributed in a 15x15x15 nm simulation box with water and ions, to neutralize the PEI charge where added. Figure 79 shows an example of the micelles obtained.

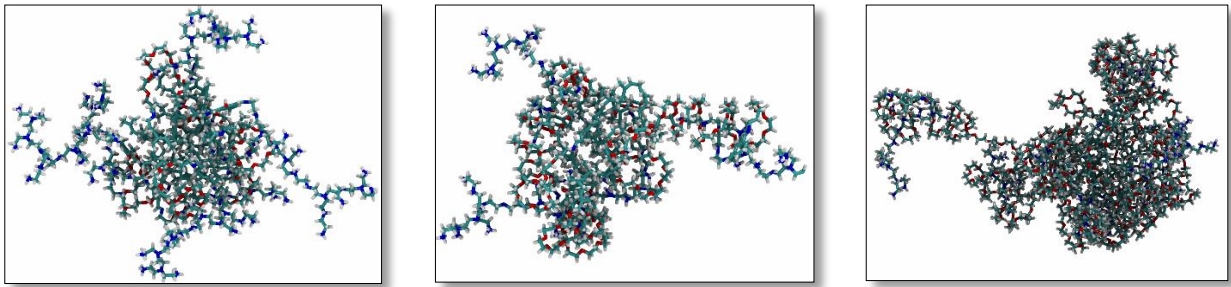


Figure 79. Examples of micelles obtained for the SQ-PEG-PEI vectors with a PEG chain (from left to right) of 500Da, 1500Da and 3000Da.

After the micelles reached equilibrium, the water was removed and three 25 base-pairs DNA molecules were added to the system in a random position. We chose three DNA molecules in order to reach an N/P ratio of about 5, known from experiment. After that, water and ions were added in order to solvate and neutralize the system and to reach a physiological ion concentration. Figure 80 depicts how the previously shown micelles interact with the DNA molecules.

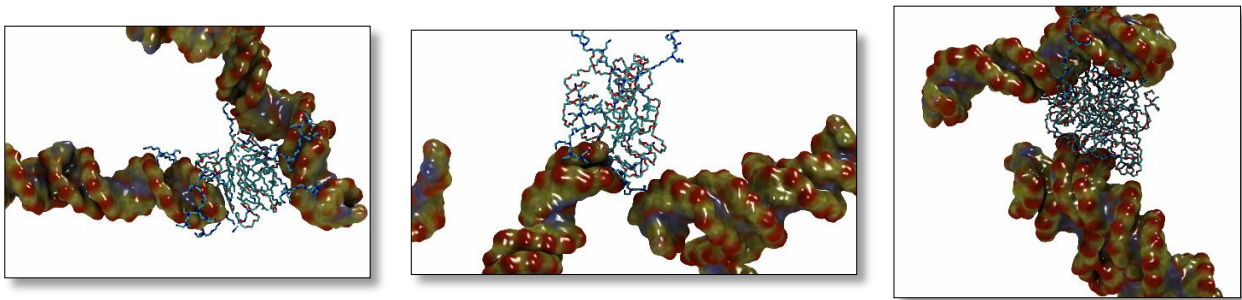


Figure 80. MD snapshots of vector DNA interactions for the SQ-PEG-PEI vectors with a PEG chain (from left to right) of 500Da, 1500Da and 3000Da.

The preliminary conclusions that can be seen are as follows. (i) The PEG interacts through hydrogen bonds with the protonated nitrogen atoms of the PEI. (ii) These hydrogen bonds are stable and still present even when the DNA is added. (iii) The number of nitrogen atoms that form hydrogen bonds with the PEG increased with the length of the PEG chain.

III – Conformational changes and $[Ca^{2+}]$ /temperature interplay in STIM1 activation

Store-operated Ca^{2+} entry (SOCE) mediates a myriad of cell functions. Stromal interaction molecule 1 (STIM1) detects $[Ca^{2+}]$ decrease in the endoplasmic reticulum (ER), using the EF-SAM machinery: helix-loop-helix motif (EF-hand) coupled to a sterile α motif (SAM). In lower ER $[Ca^{2+}]$ the STIM1 intraluminal EF-SAM undergoes substantial loss of secondary structure, exposure of hydrophobic residues, and dimerization/oligomerization, thus initiating SOCE. The puzzle of conformational dynamics of STIM1 activation has now been largely resolved, but some issues remain unclear, such as the mechanism of luminal EF-SAM dimerization, how this is transduced into cytoplasmic domain oligomerization, and STIM1 temperature sensitivity. The aim of this study was to determine the conformational changes in the EF-SAM domain of STIM1, immediately after Ca^{2+} dissociates from its binding site. For this we used MD simulations of the NMR structure of EF-SAM (Sthatopoulos, 2008) ensuing several scenarios. The overall simulation approach is schematized in Figure 81.

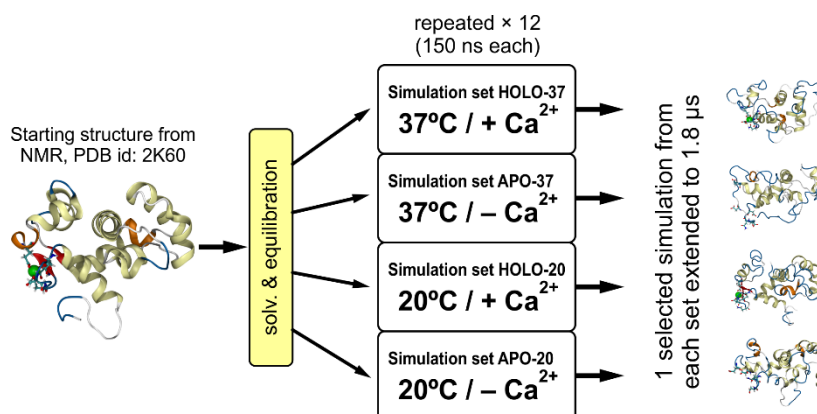


Figure 81. Strategy for molecular dynamics simulations of the EF-SAM domain of stromal interaction molecule 1 (STIM1).

Preliminary simulations showed that the RMSD of the protein backbone at 37 °C with Ca^{2+} displayed large deviations from the NMR structure over the first several hundred ns, similar to those recorded for the Ca^{2+} free form. While for the Ca^{2+} free form this could be anticipated, it would rather not be for the Ca^{2+} bound form. This was attributed to the temperature difference between the simulations (37 °C) and the NMR experiment (20 °C). Also, early in the Ca^{2+} free simulation (50 to 150 ns) a profound conformational alteration of cEF in the Ca^{2+} binding site loop developed. While the Ca^{2+} binding site expansion is an expected consequence of Ca^{2+} removal in EF-hand proteins, the large EF-SAM binding loop unfolding is atypical, though previously mentioned for some EF-hand proteins. Still, the uncommon structure of EF-SAM, which pairs together a Ca^{2+} sensitive (cEF) and a Ca^{2+} insensitive (hEF) EF-hand, may impose particular structural responses upon Ca^{2+} loss. To further investigate these aspects four simulation conditions were used in terms of temperature and Ca^{2+} presence: $T = 20^\circ\text{C}$ with Ca^{2+} , $T = 20^\circ\text{C}$ without Ca^{2+} , $T = 37^\circ\text{C}$ with Ca^{2+} and $T = 37^\circ\text{C}$ without Ca^{2+} . The simulations performed within each combination of parameters will be referred here as HOLO-20, APO-20, HOLO-37, and APO-37 respectively. Initially, for each combination, 12 short individual simulations (150 ns) were performed starting with different initial velocities. This was necessary to test the reproducibility of the observed large binding loop expansion in the Ca^{2+} free form and its stability in the Ca^{2+} loaded form. To investigate longer time scale behavior, four simulations (one per each set of 12) were extended to 1.8 μs . For APO-37 and APO-20 sets, the simulations with the largest binding site RMSD were chosen for continuation. For HOLO-37 and HOLO-20, the simulations to be continued were randomly chosen within each set. Due to the long-time scale of the extended simulations, one major concern over the accuracy of HOLO simulations was Ca^{2+} stability inside the binding site. A possible Ca^{2+} separation from the protein would have had the undesirably effect of converting HOLO to APO form. Distances between Ca^{2+} and different representative carbon atoms (Asp76 ($\text{C}\gamma$), Asp78($\text{C}\gamma$), Asn80($\text{C}\gamma$), Asp82($\text{C}\gamma$), and Glu87($\text{C}\delta$)) were plotted against simulation time (Fig. S1). The Ca^{2+} has never dissociated from the binding site, in neither HOLO-37 nor HOLO-20, so these simulations do describe the dynamics of the EF-SAM Ca^{2+} -loaded form, with the preservation of the pentagonal bipyramidal geometry of the bound cation. Given that the correlations in low-frequency atomic displacements (i.e. large conformational changes) are under sampled in conventional MD, even on the microsecond time scale, we have decided to perform also extended ensemble simulations. Advanced replica exchange with solute tempering (REST2) simulations were undertaken to evaluate the EF-SAM conformation at different reference temperatures and to assess EF-SAM thermal unfolding curves. The latter ones could be directly compared with the experimental data. The REST2 simulations were performed both in the presence and in the absence of Ca^{2+} ions. The results showed that hEF-hand is highly sensitive to temperature compared to cEF. While

hEF is mainly folded at 20 °C in the Ca^{2+} presence, at 37 °C it is much less structured. Moreover, even at a lower temperature of 20 °C, the unfolding “threshold” is more efficiently reached when Ca^{2+} is lost. In Ca^{2+} depleted state, cEF becomes highly unstable which further destabilizes the hEF to become completely “unfolded“. SAM is stable displaying no Ca^{2+} dependency (see Figure 82).

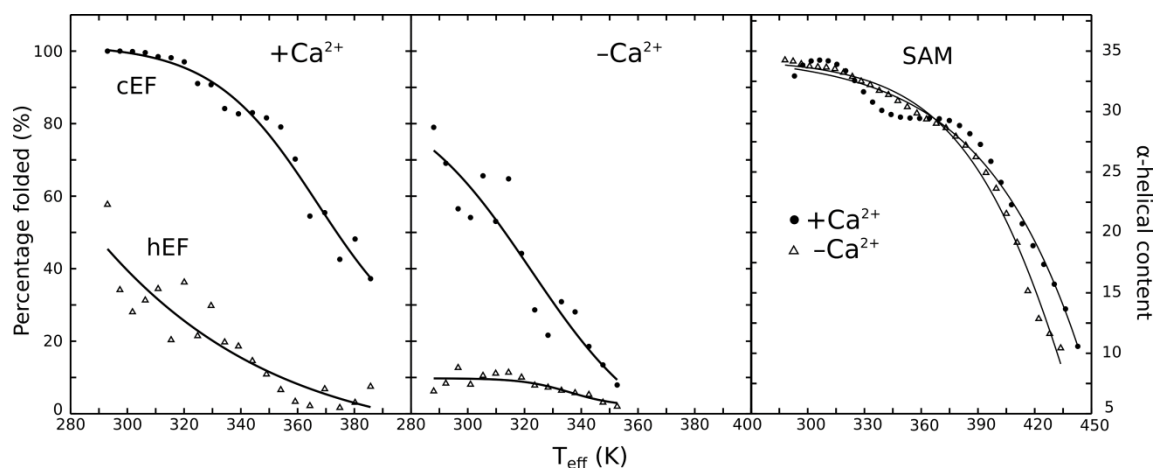


Figure 82. Temperature/ Ca^{2+} interplay in EF-SAM sensor domain.

References

- [1] Badger M.R., Price G.D., *The role of carbonic anhydrase in photosynthesis*. Annu. Rev. Plant Physiol. Plant Mol. Biol., 45, **1994**, 369-392. DOI:10.1146/annurev.pp.45.060194.002101.
- [2] *PDB101: Molecule of the Month: Carbonic Anhydrase*. RCSB: PDB-101. Retrieved **2018-12-03**.
- [3] Supuran C.T., *Carbonic Anhydrases: Catalytic and Inhibition Mechanisms, Distribution and Physiological Roles*; in *Carbonic Anhydrase. Its Inhibitors and Activators*, Editors: Supuran C.T., Scozzafava A., Conway J., CRC Press LLC, Boca Raton (FL, USA), **2004**, p. 1-24.
- [4] Supuran C.T., *Structure and function of carbonic anhydrases*, Biochem J., 473, **2016**, 2023-2032.
- [5] Supuran C.T., *Advances in structure-based drug discovery of carbonic anhydrase inhibitors*. Expert Opin Drug Discov, 12, **2017**, 61-88.
- [6] Supuran C.T., *Carbonic anhydrases: novel therapeutic applications for inhibitors and activators*. Nat Rev Drug Discov, 7, **2008**, 168-181.
- [7] Neri D., Supuran C.T., *Interfering with pH regulation in tumours as a therapeutic strategy*. Nat Rev Drug Discov, 10, 2011, 767-777.
- [8] Supuran C.T., Vullo D., Manole G., et al., *Designing of novel carbonic anhydrase inhibitors and activators*, Curr Med Chem Cardiovasc Hematol Agents, 2, **2004**, 49-68.

- [9] Canto de Souza L., Provensi G., Vullo D., et al., *Carbonic anhydrase activation enhances object recognition memory in mice through phosphorylation of the extracellular signal-regulated kinase in the cortex and the hippocampus*, *Neuropharmacology*, 118, **2017**,148-56.
- [10] Wang X., Schroder H.C., Schlossmacher U., et al., *Modulation of the initial mineralization process of SaOS-2 cells by carbonic anhydrase activators and olyphosphate*, *Calcif Tissue Int*, 94, 2014, 495-509.
- [11] Sanku R.K.K., John J.S., Ilies M.A., Walker E.A., *Potential learning and memory disruptors and enhancers in a simple, 1-day operant task in mice*, *Behav Pharmacol*, 29, 2018, 482-492.
- [12] Margheri F., Ceruso M., Carta F., et al., *Overexpression of the transmembrane carbonic anhydrase isoforms IX and XII in the inflamed synovium*, *J Enzyme Inhib Med Chem*, 31 (suppl 4), **2016**,60-63.
- [13] Bua S., Di Cesare Mannelli L., Vullo D., et al., *Design and synthesis of novel nonsteroidal anti-inflammatory drugs and carbonic anhydrase inhibitors hybrids (NSAIDs-CAIs) for the treatment of rheumatoid arthritis*, *J Med Chem*, 60, **2017**, 1159-1170.
- [14] Del Prete S., Vullo D., Osman S.M., et al., *Anion inhibitors of the b-carbonic anhydrase from the pathogenic bacterium responsible of tularemia, Francisella tularensis*, *Bioorg Med Chem*, 25, 2017, 4800-4804.
- [15] Angeli A., Del Prete S., Pinteala M., Maier S.S., Donald W.A., Simionescu B.C., Capasso C., Supuran C.T., *The first activation study of the β carbonic anhydrases from the pathogenic bacteria Brucella suis and Francisella tularensis with amines and amino acids*, *Journal of Enzyme Inhibition and Medicinal Chemistry*, 34, **2019**,1178-1185.
- [16] Capasso C., Supuran C.T., *Bacterial carbonic anhydrases*, in: *Zinc Enzyme Inhibitors - Volume 1: Enzymes from microorganisms*, Editors: Supuran C.T., Capasso C., Topics in Medicinal Chemistry, 22, **2017**, 135-152.
- [17] Supuran CT, Capasso C., *Protozoan carbonic anhydrases*, in: *Zinc Enzyme Inhibitors - Volume 1: Enzymes from microorganisms*, Editors: Supuran C.T., Capasso C., Topics in Medicinal Chemistry, 22, **2017**, 114-134.
- [18] Lehneck R, Poggeler S., *Fungal carbonic anhydrases and their inhibition*, in: *Zinc Enzyme Inhibitors - Volume 1: Enzymes from microorganisms*, Editors: Supuran C.T., Capasso C., Topics in Medicinal Chemistry, 22, **2017**. 95-110.
- [19] Angeli A., Pinteala M., Maier S.S., Del Prete S., Capasso C., Simionescu B.C, Supuran C.T, *Inhibition of bacterial α -, β - and γ class carbonic anhydrases with selenazoles incorporating benzenesulfonamide moieties*, *Journal of Enzyme Inhibition and Medicinal Chemistry*, 34, **2019**, 244-249.
- [20] Supuran C.T., *Carbonic anhydrase inhibitors and their potential in a range of therapeutic areas*, *Expert Opin Ther Pat.*, 28, **2018**. 709-712.
- [21] Supuran C.T., *Applications of carbonic anhydrases inhibitors in renal and central nervous system diseases*, *Expert Opin Ther Pat.*, 28, **2018**, 713-721.

- [22] Nocentini A., Supuran C.T., *Carbonic anhydrase inhibitors as antitumor/antimetastatic agents: a patent review (2008-2018)*, Expert Opin Ther Pat., 28, **2018**, 729-740.
- [23] Supuran C.T., Capasso C., *Biomedical applications of prokaryotic carbonic anhydrases*, Expert Opin Ther Pat., 28, **2018**, 745-754.
- [24] Annunziato G., Angeli A., D'Alba F., et al., *Discovery of new potential anti-infective compounds based on carbonic anhydrase inhibitors by rational target-focused repurposing approaches*, ChemMedChem, 11, **2016**, 1904-1914.
- [25] Ozensoy Guler O., Capasso C., Supuran C.T., *A magnificent enzyme superfamily: Carbonic anhydrases, their purification and characterization*, J Enzyme Inhib Med Chem., 31, **2016**, 689-694
- [26] Del Prete S., Vullo D., De Luca V., et al., *Sulfonamide inhibition studies of the beta-carbonic anhydrase from the pathogenic bacterium vibrio cholerae*, Bioorg Med Chem, 24, **2016**, 1115-1120.
- [27] Cobaxin M., Martinez H., Ayala G., et al., *Cholera toxin expression by el tor vibrio cholerae in shallow culture growth conditions*, Microb Pathog, 66, **2014**, 5-13.
- [28] Abuaita B.H., Withey J.H., *Bicarbonate induces vibrio cholerae virulence gene expression by enhancing toxt activity*, Infect Immun, 77, **2009**, 4111-4120.
- [29] Limmathurotsakul D., Golding N., Dance D.A.B., et. al., *Predicted global distribution of Burkholderia pseudomallei and burden of melioidosis*, Nature Microbiology, 1 (1), **2016**, 15008.
- [30] Angeli A., Pinteala M., Maier S.S., Del Prete S., Capasso C., Simionescu B.C., Supuran C.T., *Inhibition of α -, β -, γ -, δ -, ϵ - and η - class carbonic anhydrases from bacteria, fungi, algae, diatoms and protozoans with famotidine*, Journal of Enzyme Inhibition and Medicinal Chemistry 34, **2019**, 644-650.
- [31] Angeli A., Ferraroni M., Supuran C.T., *Famotidine, an Antiulcer Agent, Strongly Inhibits Helicobacter pylori and Human Carbonic Anhydrases*, ACS Med Chem Lett, 9, **2018**, 1035-1038.
- [32] Turcan-Trofin G.-O., Zaltariov M.-F., Roman G., Shova S., Vornicu N., Balan-Porcarasu M., Isac D. L., Neamtu A., Cazacu M., *Amphiphilic silicone-bridged bis-triazoles as effective, selective metal ligands and biologically active agents in lipophilic environment*, Journal of Molecular Liquids, 294, **2019**, 111560; <https://doi.org/10.1016/j.molliq.2019.111560>.
- [33] Warrilow A.G., Parker J.E., Kelly D.E., Kelly S.L., *Azole Affinity of Sterol 14 α -Demethylase (CYP51) Enzymes from Candida albicans and Homo sapiens*, Antimicrobial Agents and Chemotherapy, 57 (3), **2013**, 1352-1360; DOI: 10.1128/AAC.02067-12.
- [34] Patton A.J., Poole-Warren L.A., Green R.A., *Mechanisms for Imparting Conductivity to Nonconductive Polymeric Biomaterials*, Macromol. Biosci., 16, **2016**, 1103-1121.
- [35] Zimmermann J., Porcarelli L., Rödlmeier T., Sanchez-Sanchez A., Mecerreyes D., Hernandez-Sosa G., 2018. *Fully Printed Light-Emitting Electrochemical Cells Utilizing Biocompatible Materials*, Adv. Funct. Mater., 2018, 1705795, 8 pp.

- [36] Suna Q., Qian B., Uto K., Chen J., Liu X., Minari T., Functional biomaterials towards flexible electronics and sensors *Biosens. Bioelectron.*, 119, **2018**, 237-251.
- [37] Huang F., O'Reilly R., Zimmermann S.C., *Polymer self-assembly: a web themed issue*, *Chem. Commun.*, 50, **2014**, 13415-13416.
- [38] Verma G., Haasan P., 2016 *Self-Assembly Approach for Biomaterials Development*; in: *Trends in Biomaterials*, Editors: Kothiyal G.P., Srinivasan A., CRC Press, Taylor and Francis Group, **2016**, Boca Raton (FL, USA), p. 49-84.
- [39] Evans R.C., *Harnessing self-assembly strategies for the rational design of conjugated polymer based materials*, *J. Mater. Chem. C.*, 1, 2013, 4190-4200.
- [40] (a) Yuksel. M., Goen Colak D., Akin M., Cianga I., Kukut M., Medine E. I., Can M., Sakarya S., Unak P., Timur S., Yagci Y., *Nonionic, Water Self-Dispersible "Hairy-Rod" Poly(p-phenylene)-g-poly(ethylene glycol) Copolymer/Carbon Nanotube Conjugates for Targeted Cell Imaging*, *Biomacromolecules*, 13, **2012**, 2680-2691; (b) Xie G., Krys P., Tilton R., Matyjaszewski K., *Heterografted Molecular Brushes as Stabilizers for Water-in-Oil Emulsions*, *Macromolecules*, 50, **2017**, 2942-2950; (c) Yang C., Huang S., Wang X., Wang M., *Theranostic unimolecular micelles of highly fluorescent conjugated polymer bottlebrushes for far red/near infrared bioimaging and efficient anticancer drug delivery*, *Polym. Chem.*, 7, **2016**, 7455-7468; (d) Molina B., Bendrea A.-D., Cianga L., Armelin E., delValle L., Cianga I., Aleman C., *The biocompatible polythiophene-g-polycaprolactone copolymer as an efficient dopamine sensor platform*, *Polym. Chem.*, 8, **2017**, 6112-6122; (e) Molina B., Cianga L., Bendrea A.-D., Cianga I., delValle L., Estrany F., Aleman C., Armelin E., *Amphiphilic polypyrrole-poly(Schiff base) copolymers with poly(ethylene glycol) side chains: synthesis, properties and applications*, *Polym. Chem.*, 9, **2018**, 4218-4232.
- [41] (a) Demirel A.L., Yurteri S., Cianga I., Yagci Y., *Synthesis and morphological characterization of poly(ϵ -caprolactone) and poly(2-methyloxazoline) substituted phenyl rings and phenylene oligomers*, *J. Polym. Sci. Part A: Polym. Chem.*, 45, **2007**, 2091-2104; (b) Wu D., Xu F., Huang Y., Chen C., Yu C., Feng X., Yan D., Mai Y., *Effect of Side Chains on the Low-Dimensional Self-Assembly of Polyphenylene-Based "Rod-Coil" Graft Copolymers in Solution*, *Macromolecules*, 51, **2018**, 161-172.
- [42] Li L., Raghupathi K., Song C., Prasad P., Thayumanavan S., *Self-assembly of random copolymers*, *Chem. Commun.*, 50, **2014**, 15417-15432.
- [43] (a) Xie G., Krys P., Tilton R., Matyjaszewski K., *Heterografted Molecular Brushes as Stabilizers for Water-in-Oil Emulsions*. *Macromolecules*, 50. **2017**, 2942-2950; (b) Yang C., Huang S., Wang X., Wang M., *Theranostic unimolecular micelles of highly fluorescent conjugated polymer bottlebrushes for far red/near infrared bioimaging and efficient anticancer drug delivery*, *Polym. Chem.*, 7, **2016**, 7455-7468.
- [44] Hattori G., Hirai Y., Sawamoto M., Terashima T., *Self-assembly of PEG/dodecyl-graft amphiphilic copolymers in water: consequences of the monomer sequence and chain flexibility on uniform micelles*, *Polym. Chem.*, 8, **2017**, 7248-7259.
- [45] (a) Gou M. L., Zheng L., Peng X.Y., Men K., Zheng X.L, Zeng S., Guo G, Luo F., Zhao X., Chen L. J., Wei Y. Q., Qian Z.Y., *Poly(ϵ -caprolactone) – poly(ethylene glycol)- poly(ϵ -caprolactone) (PCL-PEG-PCL) nanoparticles for honokiol delivery in viro*, *Int. J. Pharm.*, 375, **2009**, 170-176; (b) Li Z., Tan B.H., *Towards the development of polycaprolactone*

based amphiphilic block copolymers: molecular design, self-assembly and biomedical applications, Mater. Sci. Eng. C, 45, **2014**, 620-634.

[46] Rodriguez-Arco L., Poma A., Ruiz-Perez L., Scarpa E., Ngamkham K., Battaglia G., *Molecular bionics - engineering biomaterials at the molecular level using biological principles*, Biomaterials, 192, 2019, 26-50.

[47] Li S., Ye C., Zhao G., Zhang M., Zhao Y., *Synthesis and properties of monocleavable amphiphilic comblike copolymers with alternating PEG and PCL grafts*, J. Polym. Sci. Part A: Polym Chem., 50, **2012**, pp. 3135-3148.

[48] Johnson J. A., Lu Y.Y., Burts A.O., Lim Y.-H., Finn M.G., Koberstein J.T, Turro N. J., Tirrell D.A., Grubbs R.H., *Core-Clickable PEG-Branch-Azide Bivalent-Bottle-Brush Polymers by ROMP: Grafting-Through and Clicking-To*, J. Am. Chem. Soc., 133, **2011**, 559-566.

[49] Finne A., Andronova N., Albertsson A.-C., *Well-Organized Phase-Separated Nanostructured Surfaces of Hydrophilic/Hydrophobic ABA Triblock Copolymers*, Biomacromolecules, 4, **2003**, 1451-1456.

[50] Kerstetter J.L., Gramlich W., *Nanometer-scale self-assembly of amphiphilic copolymers to control and prevent biofouling*, J. Mater. Chem. B., 2, **2014**, 8043-8052.

[51] Du W., Ohayon D., Combe C., Mottier L., Maria I.P., Ashraf R.S., Fiumelli H., Inal S., McCulloch I., *Improving the Compatibility of Diketopyrrolopyrrole Semiconducting Polymers for Biological Interfacing by Lysine Attachment*, Chem. Mater., 30, **2018**, 6164-6172.

[52] Valente C.A., Chagastelles P.C, Nicoletti N.F., Garcez G.R., Herrmann B.S.F., Pesenatto G., Goldani E., Zanini M.L., Campos M.M., Papaleo R.M., da Silva J.B., de Souza Basso N.R., *Design and optimization of biocompatible polycaprolactone/poly (l-lactic-co-glycolic acid) scaffolds with and without microgrooves for tissue engineering applications*, J Biomed Mater Res Part A, 106, **2018**, 1522-1534.

[53] Dalby M.J., Childs S., Riehle M.O., Johnstone H.J.H, Affrossman S., Curtis A.S.G., *Fibroblast reaction to island topography: changes in cytoskeleton and morphology with time*, Biomaterials, 24, **2003**, 927-935.

[54] Ajami-Henriquez D., Rodríguez M., Sabino M., Castillo R.V., Müller A.J., Boschetti-de-Fierro A., Abetz C., Abetz V., Dubois P., *Evaluation of cell affinity on poly(L-lactide) and poly(ϵ -caprolactone) blends and on PLLA-*b*-PCL diblock copolymer surfaces*, J. Biomed. Mater. Res., Part A, 87A, **2008**, 405-417.

[55] Rotariu L., Istrate O.M., Bala C., *Poly(allylamine hydrochloride) modified screen-printed carbon electrode for sensitive and selective detection of NADH*, Sens. Actuators, B, 191, **2014**, 491-497.

[56] Aquib M., Farooq M.A., Banerjee P., Akhtar F., Filli M.S., Boakye-Yiadom K.O., Kesse S., Raza F., Maviah M.B.J., Mavlyanova R., Wang B., *Targeted and stimuli-responsive mesoporous silica nanoparticles for drug delivery and theranostic use*, J Biomed Mater Res., 107A, **2019**, 2643-2666.

- [57] Vasconcelos I.B., da Silva T.G., Militao G.C G., Soares T.A., Rodrigues N.M., Rodrigues M.O., da Costa Jr. N.B., Freiree R.O., Severino A. Jr., *Cytotoxicity and slow release of the anti-cancer drug doxorubicin from ZIF-8*, RSC Adv., 2, **2012**, 9437-9442.
- [58] Huh S., Wiench J.W., Yoo J.-C., Pruski M., Lin, V.S.-Y., *Organic Functionalization and Morphology Control of Mesoporous Silicas via a Co-Condensation Synthesis Method*, Chemistry of Materials, 15(22), 2003, 4247-4256; DOI:10.1021/cm0210041.
- [59] Ménard M., Meyer F., Parkhomenko K., Leuvre C., Francius G., Bégin-Colin S., Mertz D., *BBA - General Subjects*, <https://doi.org/10.1016/j.bbagen.2018.10.020>
- [60] Hernandez-Montoto A., Gorbe M., Llopis-Lorente A., Terres J.M., Montes R., Cao-Milan R., Diaz de Grenu B., Alfonso M., Orzaez M., Dolores Marcos M., Martnez-Manez R., Sancenon F., *A NIR light-triggered drug delivery system using core-shell gold nanostars-mesoporous silica nanoparticles based on multiphoton absorption photo-dissociation of 2-nitrobenzyl PEG*, Chem. Commun., DOI: 10.1039/c9cc04260a.
- [61] Dong J., Yao X., Sun S., Zhong Y., Qiana C., Yang D., *In vivo targeting of breast cancer with a vasculature-specific GQDs/hMSN nanoplatfom*, RSC Adv., 9, **2019**, 11576.
- [62] Fenga S., Zhangb H., Xua S., Zhic C., Nakanishia H., Gaoa X.D., *Folate-conjugated, mesoporous silica functionalized boron nitride nanospheres for targeted delivery of doxorubicin*, Mater. Sci. Eng. C, 96, **2019**, 552-560.
- [63] Fortuni B., Inose T., Ricci M., Fujita Y., Van Zundert I., Masuhara A., Fron E., Mizuno H., Latterini L., Rocha S., Uji H., *Polymeric Engineering of Nanoparticles for Highly Efficient Multifunctional Drug Delivery Systems*, Scientific Reports, 9, **2019**, 2666; <https://doi.org/10.1038/s41598-019-39107-3>
- [64] Heggannavar G.B., Vijeth S., Kariduraganavar M.Y., *Development of dual drug loaded PLGA based mesoporous silica nanoparticles and their conjugation with Angiopep-2 to treat glioma*, Journal of Drug Delivery Science and Technology, 53, **2019**, 101157.
- [65] Kuang Y., Chen H., Chen Z., Wan L., Liu J., Xu Z., Chen X., Jiang B., Li C., *Poly(amino acid)/ZnO/mesoporous silica nanoparticle based complex drug delivery system with a charge-reversal property for cancer therapy*, Colloids and Surfaces B: Biointerfaces, 181, **2019**, 461-469.
- [66] Li Y., Song F., Cheng L., Qian J., Chen Q., *Functionalized Large-Pore Mesoporous Silica Microparticles for Gefitinib and Doxorubicin Codelivery*, Materials, 12, **2019**, 766; DOI:10.3390/ma12050766.
- [67] Ren X., He L., Tian X., Zhang Z., Chen Z., Mei X., *pH and folic acid dual responsive polysaccharide nanospheres used for nuclear targeted cancer chemotherapy*, Colloids and Surfaces B: Biointerfaces, 178, **2019**, 445-451.
- [68] Shahmoradi S., Bahram M., Hoseinpour F., *Magnetic mesoporous silica nanoparticles functionalized by pH-sensitive caps for DOX release*, Journal of the Iranian Chemical Society, <https://doi.org/10.1007/s13738-019-01652-z>
- [69] Shen Y., Li M., Liu T., Liu J., Xie Y., Zhang J., Xu S., Liu H., *A dual-functional HER2 aptamer-conjugated, pH-activated mesoporous silica nanocarrier-based drug delivery system*

provides in vitro synergistic cytotoxicity in HER2-positive breast cancer cells, International Journal of Nanomedicine, 14, **2019**, 4029-4044.

[70] Singh R.K., Patel K.D., Mahapatra C., Parthiban S.P., Kim T.-H., Kim H.-W., *Combinatory Cancer Therapeutics with Nanoceria-Capped Mesoporous Silica Nanocarriers through pH-triggered Drug Release and Redox Activity*, ACS Appl. Mater. Interfaces, 11, **2019**, 288-299.

[71] Sun P., Leidner A., Weigel S., Weidler P.G., Heissler S., Scharnweber T., Niemeyer C.M., *Biopebble Containers: DNA-Directed Surface Assembly of Mesoporous Silica Nanoparticles for Cell Studies*, Small, **2019**, 1900083.

[72] Tang S., Huang X., Chen X., Zheng N., *Hollow Mesoporous Zirconia Nanocapsules for Drug Delivery*, Adv. Funct. Mater, 20, **2010**, 2442-2447.

[73] Tessaro A.L., Fraix A., Pedrozo da Silva A.C., Gazzano E., Riganti C., Sortino S., *“Three-Bullets” Loaded Mesoporous Silica Nanoparticles for Combined Photo/Chemotherapy*, Nanomaterials, 9, **2019**, 823; DOI:10.3390/nano9060823.

[74] Vo U.V., Nguyen C.K., Nguyen V.C., Tran T.V., Thi B.Y.T., Nguyen D.H., *Gelatin-poly (ethylene glycol) methyl ether-functionalized porous Nanosilica for efficient doxorubicin delivery*, Journal of Polymer Research, 26 (6), **2019**; <https://doi.org/10.1007/s10965-018-1654-8>.

[75] Wu Y., Xu Z., Sun W., Yang Y., Jin H., Qiu L., Chen J., Chen J., *Co-responsive smart cyclodextrin-gated mesoporous silica nanoparticles with ligand-receptor engagement for anti-cancer treatment*, Materials Science & Engineering C, 103, **2019**, 109831.

[76] Yang Y.J., Tao X., Hou Q., Maa Y., Chen X.-L., Chen J.-F., *Mesoporous silica nanotubes coated with multilayered polyelectrolytes for pH-controlled drug release*, Acta Biomaterialia, 6, **2010**, 3092-3100.

[77] Zhu D., Hu C., Liu Y., Chen F., Zheng Z., Wang X., *Enzyme-/Redox-Responsive Mesoporous Silica Nanoparticles Based on Functionalized Dopamine as Nanocarriers for Cancer Therapy*, ACS Omega, 4, **2019**, 6097-6105.

[78] Yang S., Song S., Han K., Wu X., Chen L., Hu Y., Wang J., Liu B., *Characterization, in vitro evaluation and comparative study on the cellular internalization of mesoporous silica nanoparticle-supported lipid bilayers*, Microporous and Mesoporous Materials, 284, **2019**, 212-224.

[79] Garg R., *Supramolecular Chemistry of Host-Guest Inclusion Complexes*, GRIN Verlag, Munich, **2012**; <https://www.grin.com/document/187894>

[80] Marangoci N., Timpu D., Corciova A., Mircea C., Petrovici A.-R., Nicolescu A., Ursu E.-L., Nastasa V., Bostanaru A.C., Mares M., Perteala M., *β -Cyclodextrin as a Functional Excipient Used for Enhancing the Diminazene Acetate Bioavailability*, Pharmaceutics, 11, **2019**, 295-311.

[81] Miller D.M., Swan G.E., Lobetti R.G., Jacobson L.S., *The pharmacokinetics of diminazene acetate after intramuscular administration in healthy dogs*, J. S. Afr. Vet. Assoc., 76 (3), **2005**, 146-150.

- [82] Akode R.M., Shantier S.W., Gadkariem E.A., Mohamed M.A., *Simultaneous determination and stability studies on diminazene diacetate and phenazone using developed derivative spectrophotometric method*, Hindawi International Journal of Analytical Chemistry, Volume **2017**, Article ID 4269587, 6 pages; <https://doi.org/10.1155/2017/4269587>
- [83] Turin-Moleavin I.-A., Fifere A., Lungoci A.-L., Rosca I., Coroaba A., Peptanariu D., Nastasa V., Pasca S.-A., Bostanaru A.-C., Mares M., Pinteala M., *In vitro and in vivo antioxidant activity of the new magnetic-cerium oxide nanoconjugates*, Nanomaterials, 9, 2019, Article no. 1565; DOI:10.3390/nano9111565.
- [84] Calucci L., Pinzono C., Zandomenighi M., Capocchi A., Ghiringhelli S., Saviozzi F., Tozzi S., Galleschi L., J. Agric. Food Chem., *Effects of gamma-irradiation on the free radical and antioxidant contents in nine aromatic herbs and spices*, 51 (4), **2003**, 927-934.
- [85] Vijayakumar R.S., Surya D., Nalini N., *Antioxidant efficacy of black pepper (Piper nigrum L.) and piperine in rats with high fat diet induced oxidative stress*, Redox Rep., 9, **2004**, 105-110.
- [86] Gorgani L., Mohammadi M., Najafpour G.D., Nikzad M., *Piperine - The Bioactive Compound of Black Pepper: From Isolation to Medicinal Formulations*, *Comprehensive Reviews*, Food Science and Food Safety, 16, **2017**, 124-140.
- [87] Mittal R., Gupta R.L., *In vitro antioxidant activity of piperine*, Methods Find Exp Clin Pharmacol., 22, **2000**, 271-274.
- [88] Zettersten C.C.M., Wende S., Turner C., Nyholm L., Sjöberg P J R., *Identification and Characterization of Polyphenolic Antioxidants Using On-Line Liquid Chromatography, Electrochemistry, and Electrospray Ionization Tandem Mass Spectrometry*, Analytical Chemistry, 81(21), **2009**, 8968-8977.
- [89] Ziyatdinova G.K., Budnikov H.C., *Evaluation of the antioxidant properties of spices by cyclic voltammetry*, Journal of Analytical Chemistry, 69 (10), **2014**, 990-997.
- [90] Wei K., Li W., Koike K., Nikaido T., *Cobalt(II)-Catalyzed Intermolecular Diels–Alder Reaction of Piperine*, Org. Lett., 7 (14), **2005**, 2833-2835.
- [91] Borrajo E., Vidal A., Alonso M.J., Garcia-Fuentes M., *How regenerative medicine can benefit from nucleic acids delivery nanocarriers?*, in: *Polymers in Regenerative Medicine: Biomedical Applications from Nano- to Macro-Structures*, Editors: Pradas M.M, Vicent M.J., John Wiley & Sons, Inc., Hoboken (NJ, USA), **2015**, p. 285-336.
- [92] Fumoto S., Nishida K, *Methods for Evaluating the Stimuli-Responsive Delivery of Nucleic Acid and Gene Medicines*, Chem. Pharm. Bull., 65, **2017**, 642-648.
- [93] Wang D., Tai P.W.L., Gao G., *Adeno-associated virus vector as a platform for gene therapy delivery*, Nature Rev. Drug Discovery, 18, **2019**, 358-378; DOI: 10.1038/s41573-019-0012-9.
- [94] Foldvari M., Chen D.W., Nafissi N., Calderon D., Narsineni L., Rafiee A., *Non-viral gene therapy: Gains and challenges of non-invasive administration methods*, Journal of Controlled Release, 240, **2016**, 165-190.

- [95] Gao D., Duan L., Wu M., Wang X., Sun Z., Zhang Y., Li T., He P., *Preparation of thermo/redox/pH-stimulative poly(N-isopropylacrylamide-co-N,N'-dimethylaminoethyl methacrylate) nanogels and their DOX release behaviors*, J Biomed Mater Res Part A, 9999A, **2019**, 1-9.
- [96] Bergman D., Laaksonen L., Laaksonen A., *Visualization of solvation structures in liquid mixtures*, Journal of Molecular Graphics & Modelling, 15 (5), **1997**, 301-306.
- [97] Kusalik P.G., Laaksonen A., Svishchev I.M., *Spatial Structure in Molecular Liquids*, in: *Theoretical and Computational Chemistry, Volume 7: Molecular Dynamics. From Classical to Quantum Methods*, Editors: Balbuena B., Seminario M, Elsevier Science B.V, Amsterdam, **1999**, p. 61-97.
- [98] Lyubartsev A., Laaksonen A., *MDynaMix - A scalable portable parallel MD simulation package for arbitrary molecular mixtures*, Comp. Phys. Comm., 128 (3), 2000, 565-589.
- [99] Zhu Y.-L., Liu H., Li Z.-W., Qian H.-J., Milano G., Lu Z.-Y., *GALAMOST: GPU-accelerated large-scale molecular simulation toolkit*, J. Comp. Chem., 34 (25), 2013, 2197-2211; DOI:10.1002/jcc.23365.
- [100] Zhu Y.L., Xuc D., Hed K.J., Pei H.W., Li Z.-W., Lu Z.Y., Laaksonen A., Sun Z.Y., *Exploiting the pure GPU power with GALAMOST in large-scale MD simulations*, Computational Materials Science, under review, April **2019**.
- [101] Lyubartsev A., Laaksonen A., *Calculation of effective interaction potentials from radial distribution functions: A reverse Monte Carlo approach*, Phys. Rev. E, 52 (4), **1995**, 3730-3737; DOI:10.1103/physreve.52.3730.
- [102] Lyubartsev A., Mirzoev A., Chen L.J., Laaksonen A., *Systematic coarse-graining of molecular models by the Newton inversion method*, Faraday Discuss., 144, **2010**, 43-56; DOI:10.1039/b901511f.
- [103] Lyubartsev A., Tu Y., Laaksonen A., *Hierarchical Multiscale Modelling Scheme from First Principles to Mesoscale*, J. Comp. Theor. Nanosci., 6 (5), **2009**, 951-959.
- [104] Lyubartsev A., Karttunen M., Vattulainen I., Laaksonen A., *On Coarse-Graining by the Inverse Monte Carlo Method: Dissipative Particle Dynamics Simulations Made to a Precise Tool*, in Soft Matter Modeling, Soft Mater., 1 (1), **2003**, 121-137.
- [105] Hedman F., Laaksonen A., *Ewald summation based on nonuniform fast Fourier transform*, Chem. Phys. Lett., 425, **2006**, 142-147.
- [106] Klaikherd A., Nagamani C., Thayumanavan S., *Multi-Stimuli Sensitive Amphiphilic Block Copolymer Assemblies*, J. Am. Chem. Soc., 131 (13), **2009**, 4830-4838.
- [107] <http://pppdb.uchicago.edu/>
- [108] https://polymer.nims.go.jp/index_en.html
- [109] Bejagam K.K., An Y., Singh S.K., Deshmukh S.A., *Machine-Learning Enabled New Insights into the Coil-to-Globule Transition of Thermosensitive Polymers Using a Coarse-*

- Grained Model*, J. Phys. Chem. Lett., 9 (22), **2018**, 6480-6488; DOI: 10.1021/acs.jpcclett.8b02956.
- [110] Thomas D.G., Klaessig F., Harper S.L., Fritts M., Hoover M.D., Gaheen S., Stokes T.H., Reznik-Zellen R., Freund E.T., Klemm J.D., Paik D.S., Baker N.A., *Informatics and standards for nanomedicine technology*, Wiley Interdiscp. Rev. Nanomed. Nanobiotechnol., 3 (5), **2011**, 511-522.
- [111] <http://www.obofoundry.org/>
- [112] Lyubartsev A., Jacobsson S., Sundholm G., Laaksonen A., *Solubility of Organic Compounds in Water/Octanol Systems. A Expanded Ensemble MD Simulation Study of log P Parameters*, J. Phys. Chem. B, 105, **2001**, 7775-7778.
- [113] Åberg K.M., Lyubartsev A., Jacobsson S., Laaksonen A., *Determination of solvation free energies by adaptive expanded ensemble molecular dynamics*, J. Chem. Phys., 120 (8), **2004**, 3770-3376.
- [114] Sun T.Y., Liang L.J., Wang Q., Laaksonen A., Wu T., *A molecular dynamics study on pH response of protein adsorbed on peptide-modified polyvinyl alcohol hydrogel*, Biomater. Sci., 2 (3), **2014**, 419-426.
- [115] Jämbeck J.P.M., Eriksson E.S.E., Laaksonen A., Lyubartsev A., Eriksson L.A., *Molecular Dynamics Studies of Liposomes as Carriers for Photosensitizing Drugs: Development, Validation, and Simulations with a Coarse-Grained Model*, J. Chem. Theory Comput., 10 (10), **2014**, 5-13.
- [116] Naômé A., Laaksonen A., Vercauteren D.P., *A Coarse-Grained Simulation Study of the Structures, Energetics, and Dynamics of Linear and Circular DNA with Its Ions*, J. Chem. Theory Comput., 11 (6), **2015**, 2813-2826.
- [117] Tang Y.H., Lu L., Li H., Evangelinos C', Grinberg L., Sachdeva V., Karniadakis G.E., *OpenRBC: A Fast Simulator of Red Blood Cells at Protein Resolution*, Biophysical Journal, 112 (10), **2017**, 2030-2037.
- [118] Plimpton S., *Fast Parallel Algorithms for Short-Range Molecular Dynamics*, J. Comp. Phys., 117, **1995**, 1-19.
- [119] Sarman S., Wang Y., Laaksonen A., *Variational principle for nonequilibrium steady states tested by molecular dynamics simulation of liquid crystal model systems*, in: *Non-Equilibrium Particle Dynamics*, IntechOpen Limited, London (UK), **2018**; DOI: 10.5772/intechopen.80977
- [120] Wang Y.L., Lu Z.Y., Laaksonen A., *Specific binding structures of dendrimers on lipid bilayer membranes*, Phys. Chem. Chem. Phys., 14, **2012**, 8348-8359.
- [121] Smith S.A., Selby L.I., Johnston A.P.R., Such G.K., *The Endosomal Escape of Nanoparticles: Toward More Efficient Cellular Delivery*, Bioconjugate Chem., 30 (2), **2019**, 263-272.
- [122] Tu Y., Laaksonen A., *Implementing Quantum Mechanics into Molecular Mechanics Combined QM/MM Modeling Methods*, Advances in Quantum Chemistry, 59, **2010**, 1-15.

- [123] Tu Y., Jacobsson S., Laaksonen A., *Efficient ab initio tight-binding-like method for electronic structure calculations*, Phys. Rev. B, 74 (20), **2006**, article 205104; DOI: 10.1103/PhysRevB.74.205104
- [124] Gillespie D.T., *Stochastic simulation of chemical kinetics*, Annu. Rev. Phys. Chem., 58 (1), **2007**, 35-55; DOI:10.1146/annurev.physchem.58.032806.1046.
- [125] Mace A., Leetmaa M., Laaksonen A., *Temporal Coarse Graining of CO₂ and N₂ Diffusion in Zeolite NaKA: From the Quantum Scale to the Macroscopic*, J. Chem. Theor. Comput., 11 (10), **2015**, 4850-4860; DOI: 10.1021/acs.jctc.5b00401.
- [126] Shi X., Tian F., *Multiscale Modeling and Simulation of Nano-Carriers Delivery through Biological Barriers - A Review*, Adv. Theory Simul., **2018**, article 1800105; DOI: 10.1002/adts.201800105.
- [127] Ziemys A., Kojic M., Milosevic M., Schrefler B., Ferrari M., *Multiscale models for transport and biodistribution of therapeutics in cancer*, Chapter 7 in: *Computer Aided Chemical Engineering*, Vol. 42, **2018**, p. 209-237; <https://doi.org/10.1016/B978-0-444-63964-6.00007-6>.
- [128] Neufeld E., Lloyd B., Schneider B., Kainz W., Kuster N., *Functionalized Anatomical Models for Computational Life Sciences*, Front. Physiol., 9, **2018**, article 1594; DOI: 10.3389/fphys.2018.01594.
- [129] Rickman J.M., Lookman T., Kalinin S.V., *Materials informatics: From the atomic-level to the continuum*, Acta Materialia 168, **2019**, 473-510.
- [130] Pankajakshan P, Sanyal S., de Noord O.E., Bhattacharya I., Bhattacharyya A., Waghmare U., *Machine Learning and Statistical Analysis for Materials Science: Stability and Transferability of Fingerprint Descriptors and Chemical Insights*, Chem. Mater., 29 (10), **2017**, 4190-4201.

III. Quantifiable results of the project, up to the current date

The **5D-nanoP** project delivered, during the year 2019, the quantifiable results which are summarized below.

1. *Published / accepted / submitted for publication papers*

All of them are mentioning the project in the Acknowledgment section.

- [1] Dong Y., Ji X., Laaksonen A., Cao W., An R., Lu L., Lu X., Determination of the small amount of proteins interacting with TiO₂ nanotubes by AFM-measurement, Biomaterials 192, **2019**, 368-376.
- [2] Angeli A., Del Prete S., Pinteala M., Maier S.S., Donald W.A., Simionescu B.C., Capasso C., Supuran C.T., *The first activation study of the β carbonic anhydrases from the pathogenic bacteria *Brucella suis* and *Francisella tularensis* with amines and amino acids*, Journal of Enzyme Inhibition and Medicinal Chemistry, 34, **2019**, 1178-1185.

- [3] Angeli A., Pinteala M., Maier S.S., Del Prete S., Capasso C., Simionescu B.C., Supuran C.T., *Inhibition of bacterial α -, β - and γ class carbonic anhydrases with selenazoles incorporating benzenesulfonamide moieties*; Journal of Enzyme Inhibition and Medicinal Chemistry, 34, **2019**, 244-249.
- [4] Angeli A., Pinteala M., Maier S.S., Del Prete S., Capasso C., Simionescu B. C., Supuran C.T., *Inhibition of α -, β -, γ -, δ -, ϵ - and η - class carbonic anhydrases from bacteria, fungi, algae, diatoms and protozoans with famotidine*, Journal of Enzyme Inhibition and Medicinal Chemistry, 34, **2019**, 644-650.
- [5] Isac D.L., Airinei A., Maftai D., Humelnicu I., Mocci F., Laaksonen A., Pinteala M., *On the charge-transfer excitations in azobenzene maleimide compounds. A theoretical study*, Journal of Physical Chemistry A, 123, **2019**, 5525-5536.
- [6] Perepelytsya S., Ulicny J., Laaksonen A., Mocci F., *Pattern preferences of DNA nucleotide motifs by polyamine putrescine²⁺, spermidine³⁺ and spermine⁴⁺*, Nucleic Acid Research, 47, **2019**, 6084-6097.
- [7] Marangoci N., Timpu D., Corciova A., Mircea C., Petrovici A.-R., Nicolescu A., Ursu E.-L., Nastasa V., Bostanaru A.C., Mares M., Perteza M., Pinteala M., *β -Cyclodextrin as a Functional Excipient Used for Enhancing the Diminazene Aceturate Bioavailability*; Pharmaceutics 11, **2019**, 295-311.
- [8] Liang S., Hall K.W., Laaksonen A., Zhang Z., Kusalik P.G., *Characterizing key features in the formation of ice and gas hydrate systems*, Philosophical Transactions of the Royal Society A: Mathematical, Physical and Engineering Sciences, 377, **2019**, Article no. 20180167/1-28.
- [9] Sarman S., Wang Y.L., Laaksonen A., *Shear flow simulations of smectic liquid crystals based on the Gay-Berne fluid and the soft sphere string-fluid*, Physical Chemistry Chemical Physics, 21, **2019**, 292-305.
- [10] Racles C., Zaltariov M.F., Silion M., Maxim A.M., Cozan V., *Photo-oxidative degradation of doxorubicin with siloxane MOFs by exposure to daylight*, Environmental Science and Pollution Research, 26, **2019**, 19684-19696.
- [11] Turin-Moleavin I.-A., Fifere A., Lungoci A.-L., Rosca I., Coroaba A., Peptanariu D., Nastasa V., Pasca S.-A., Bostanaru A.-C., Mares M., Pinteala M., *In vitro and in vivo antioxidant activity of the new magnetic-cerium oxide nanoconjugates*, Nanomaterials 9, **2019**, Article no. 1565.
- [12] Molina B.G., Cianga L., Bendrea A.-D., Cianga I., Aleman C., Armelin E., *An amphiphilic, heterografted polythiophene copolymer containing biocompatible /biodegradable side chains for use as (electro) active surface in biomedical applications*, Polymer Chemistry, 10, **2019**, 5010-5022; DOI:10.1039/C9PY00926D.
- [13] Fundueanu G., Constantin M., Bucatariu S., Ascenzi S.P., *Poly(N-isopropylacrylamide-co-N-vinylpyrrolidone) thermoresponsive microspheres: The low drug loading ensures the pulsatile release mechanism*, Express Polym. Lett., 14(1), **2020**, 63-76.
- [14] Iacob M., Racles C., Dascalu M., Tugui C., Lozan V., Cazacu M., *Nanomaterials developed by processing iron coordination compounds for biomedical application*, Journal of

Nanomaterials, **2019**, Article ID 2592974, 14 pages. <https://doi.org/10.1155/2019/2592974> (open access).

[15] Racles C., Cazacu M., Zaltariov M., Iacob M., Butnaru M., *Siloxane-based compounds with tailored surface properties for health and environment*, Phosphorus, Sulfur, and Silicon and the Related Elements, 194 (10), **2019**; 6 pages; DOI:10.1080/10426507.2019.1630405.

[16] Turcan-Trofin G.-O., Zaltariov M.-F., Roman G., Shova S., Vornicu N., Balan-Porcarasu M., Isac D.L., Neamtu A., Cazacu M., *Amphiphilic silicone-bridged bis-triazoles as effective, selective metal ligands and biologically active agents in lipophilic environment*, Journal of Molecular Liquids, 294, **2019**, 111560, <https://doi.org/10.1016/j.molliq.2019.111560>.

[17] Tugui C., Tiron V., Dascalu M., Sacarescu L., Cazacu M., *From ultra-high molecular weight polydimethylsiloxane to super-soft elastomer*, European Polymer Journal, 120, **2019**, 109243; DOI:10.1016/j.eurpolymj.2019.109243.

[18] Constantin M., Bucatariu S., Ascenzi P., Butnaru M., Fundueanu G., *Smart drug delivery system activated by specific biomolecules*, Mat. Sci Eng C (accepted).

[19] Tarabukina E., Rozanova A., Fundueanu G., Constantin M., Harabagiu V., Filippov A., *Thermo-sensitivity of poly-n-isopropylacrylamide with statistically introduced d,l-allylglycine betainic units*, J. Macromol. Sci. B: Phys. (accepted).

2. Participation in conferences / symposia

[1] Bendrea A.-D., Cianga L., Cianga I., *The simplest is the most sophisticated: A Janus type polythiophene copolymer at work for a biointegrable device*, 27th edition of scientific communications entitled "Progress in the field of macromolecular and organic compounds", organized in the frame of Academic Days of Iasi, Romania, 2-4 October **2019**.

[2] Fundueanu G., Constantin M., Bucatariu S., *Advanced polymeric materials in drug delivery*, International Congress of „Apollonia” University of Iași, Edition XXIX, 28 February - 3 March **2019**, Iasi, Romania.

[3] Suflet D.M., *Ionic curdlan hydrogels for medical and pharmaceutical application*, International Congress of „Apollonia” University of Iași, Edition XXIX, 28 February - 3 March **2019**, Iasi, Romania.

[4] Bucatariu S., Constantin M., Fundueanu G., *Design and development of sponge-type hydrogel composed of hyaluronic acid and poly(methylvinylether-alt-maleic acid) for biomedical applications*, Oral Presentation at 21st Romanian International Conference on Chemistry and Chemical Engineering, 4-7 September **2019**, Constanta, Romania.

[5] I. Popescu, M. Constantin, *Alginate-pluronic hydrogels obtained by thiol-ene photo-click reaction*, 21st Romanian International Conference on Chemistry and Chemical Engineering, 4-7 September **2019**, Constanta, Romania.

[6] Pelin I.M., Popescu I., Suflet D.M., *Phosphorylated curdlan based hydrogels for medical applications*, 21st Romanian International Conference on Chemistry and Chemical Engineering, 4-7 September **2019**, Constanta, Romania.

[7] David G., Iachim M., Pricop G., Bargan A., Rosca I., *Hybrid 3D polymer matrices-evaluation for biomedical applications*, Al 13-lea simpozion international de produse cosmetice si aromatizante, Cosmetologia - Esenta de frumos si sănătate, 4-7 iunie, **2019**, Iași, România, în Programul simpozionului, p 29-30.

[8] Ciubotaru B.-I., Zaltariov M.-F., Racles C., Cazacu M., *Functionalized mesoporous silica as carrier for controlled delivery of doxorubicin*, „Zilele Spitalului Clinic C.F. Iași”, „Performanța Științei – Știința Performanței”, Iasi, Romania, 22-27 octombrie **2019**.

[9] Ciubotaru B.-I., Zaltariov M.-F., Racles C., Cazacu M., *Preparation and application of mesoporous silica for pH-controlled delivery of doxorubicin*, Zilele Universității „Alexandru Ioan Cuza” din Iași, Conferința Facultății de Chimie, 31 Octombrie - 01 Noiembrie, **2019**.

[10] Călin M., *Nanoplatforms for Targeted Delivery of Drugs to Activated Endothelium*, “9th Annual World Congress of Nano Science & Technology-2019” (Nano S&T-2019), Suzhou, China, October 20-22, **2019** – Invited Speaker.

[11] Carnuta M., Anghelache M., Patrascu A.A., Maxim C., Popescu D.-L., Călin M., *Synthesis, characterization and in vitro antitumor evaluation of new binuclear oxovanadium(V) compounds*, “Achievements and Perspectives of Modern Chemistry”, Chișinău, Republica Moldova, October 9-11, **2019** – Lucrare Poster.

[12] Carnuta M., Patrascu A.A., Maxim C., Anghelache M., Manduteanu I., Popescu D.-L., Călin M., *A new family of vanadium compounds stimulates insulin receptor phosphorylation in HepG2 cells in a time and dose-dependent manner*, Anniversary Symposium “An incredible 40-year journey to uncover cell’s secrets for the benefit of human health”, workshop “Cardiac valves disease: new targets for therapies and tissue engineering”, București, România, September 19-20, **2019** – Lucrare Poster.

[13] Carnuta M., Patrascu A.A., Maxim C., Anghelache M., Călin M., Popescu D.-L., *Synthesis and characterization of a new vanadium (V) complex based on D/L-valine Schiff base with anti-cancer properties*, “21st Romanian International Conference on Chemistry and Chemical Engineering (RICCCE)”, Mamaia-Constanța, România, September 4-7, **2019** – Lucrare Poster.

[14] Carnuta M., Patrascu A.A., Maxim C., Anghelache M., Manduteanu I., Popescu D.-L., Călin M., *A new family of vanadium compounds stimulates insulin receptor phosphorylation in HepG2 cells in a time and dose-dependent manner*, “The 37th Annual Scientific Session of the Romanian Society for Cell Biology and the 11th National Congress with International Participation”, Constanța, România, June 20-23, **2019** – Lucrare Poster.

3. Training sessions / invited trainers / internships

[1] Dr Anca Dana Bendrea, “Grigore T. Popa” University of Medicine and Pharmacy of Iasi, Faculty of Biomedical Engineering, Centre for Tissue Engineering and Regenerative Medicine, Iasi, Romania, 30 May-20 June **2019**, Short-period training course entitled “*In vitro and in vivo testing methods for regenerative medicine*”.

4. International and internal Work meetings

- Maier S. S., participation to *The 4th Satellite Meeting on Carbonic Anhydrases*, November 14-17th **2019**, Parma, Italy; <https://ca2019parma.wordpress.com/>. Biomedical and pharmacologic perspectives of the carbonic anhydrases and their activators and inhibitors. Molecular modeling and bioinformatic approaches.

- Prof. Aatto Laaksonen, the project director, has held scientific meetings with each partner teams, leading to intermediate and final scientific reports.

IV. Topics and prognoses for Stage 2020

Based on the approaches and results of the current year, the following commitments can be formulated for the next stage of the project.

1. Regarding the molecular entities involved to supramolecular assembling

- Setting up of compounds libraries.
- Investigation of some particular inhibitors of carbonic anhydrases.
- *In silico* investigation of docking and supramolecular assembling of library unimers.

2. Regarding the nanoplatfoms synthesis and physical-chemical evaluation

- Extending the design, synthesis, and characterization of (macro)molecular components of functional nanoplatfoms.
- Preparation of stock and etalon components of functional nanoplatfoms, for accurate and systematic investigation of their functionality in crowded milieus.

3. Regarding the production of simple constituents of future tissue / tumor surrogates

- Diversification of the synthesized substrata.

We certify that all the goals of 2019 stage of **5D-nanoP** project have been achieved.

December 2, 2019

Project Director,
Professor Aatto Laaksonen, PhD.